Measuring optical properties of engineered tissues using optical coherence tomography

David Levitz

Presented to the Department of Biomedical Engineering
and the Oregon Health & Science University
School of Medicine
in partial fulfillment of
the requirements for the degree of
Doctor of Philosophy
in
Biomedical Engineering
May 2010

Department of Biomedical Engineering

School of Medicine

Oregon Health & Science University

CERTIFICATE OF APPROVAL

This is to certify that the Ph.D. dissertation of

David Levitz

has been approved

Steven L. Jacques, Thesis Advisor

Professor, Departments of Dermatology and Biomedical Engineering,

Oregon Health & Science University

Monica T. Hinds

Assistant Professor, Department of Biomedical Engineering, Oregon Health & Science University

Peter E. Andersen

Professor, Department of Photonics Engineering, Technical University of Denmark, Denmark,

and Atomic Physics Division, Department of Physics, Lund University, Sweden

Stephen R. Hanson

Professor, Department of Biomedical Engineering, Oregon Health & Science University

Ruikang K. Wang

Professor, Departments of Biomedical Engineering and Anesthesiology and Peri-Operative

Medicine, Oregon Health & Science University

To Debbie, Cool Water, and Frank

for loving me and helping me keep my sanity through complex and difficult circumstances

Acknowledgements

First and foremost, the author would like to thank his supervisor, Steve Jacques, who developed most of the theory presented in this thesis, and was instrumental in data analysis and in shaping the main conclusions in this thesis. Prof. Jacques' expertise in many topics biomedical optics, as well as in data presentation, helped the author identify the experiments needed to validate his hypotheses, and analyze the results, and present them in a convincing manner. Importantly, Prof. Jacques also provided lab space, equipment, and financial support.

The author would also like to thank Monica Hinds, who was primarily responsible in training the author in cell culture techniques, teaching the author about tissue engineering applications, and guiding him through the biological portions of the thesis. Prof. Hinds helped the author design the critical collagen gel experiments in Ch. 7-9, as well many of the earlier experiments that were not detailed in this thesis. Additionally, Prof. Hinds provided lab space and lab supplies.

The remaining author's thesis committee also helped shape many of the experiments presented in this thesis. Peter Andersen, the author's co-supervisor during his Master's studies, provided the author's initial training in biomedical optics and helped develop the idea of measuring optical properties from OCT images. Steve Hanson proposed the idea of characterizing engineered tissues, specifically collagen gels in this

thesis, and provided a protocol that was the author's starting template. Ricky Wang came on board late on short notice but was had very helpful suggestions, both as a thesis committee member and during the weekly seminars.

The author would also like to thank members of the Jacques' lab at OHSU. Niloy Choudhury built the sample arm of the OCT system, and was available to re-align the system on many occasions. Ravi Samatham assisted in countless experiments, both related and unrelated to this project, which saved the author countless hours. Without the contributions from Ravi and Niloy, this thesis would not have been possible. Yongji Fu participated in many useful discussions and came up with the phantom design that was used throughout this thesis. Dan Gareau, Ardi Ardeshiri, and Jabeer Ahmed helped with confocal mosaic imaging that was critical to Ch. 8-9. Kevin Phillips helped with confocal imaging, Frederic Truffer helped with the modeling, and Laurel Jones participated in thoughtful discussions. Keri Vartanian trained the author in sterile techniques and provided cells for experiments on very short notice. Anusha Elias, Brandon Markway, and Kathy McKenna also provided cells on short notice on multiple occasions. Lars Thrane and Thomas M. Jøgensen from Risø National Laboratory, Denmark, both of whom trained the author during his Master's studies, we helpful in developing many of the modeling and algorithm methods implemented in this thesis. And finally, the author would like to thank the faculty and staff at the Department of Biomedical Engineering for their constructive ideas and support.

Table of Contents

List of Tables

List of Figures

List of abbreviations

OCT – optical coherence tomography

SMC – smooth muscle cell

ROI – region of interest

PDF – probability density function

MMP – matrix metalloproteinase

NA – numerical aperture

EC – endothelial cell

ECM – extracellular matrix

MEM – minimum essential medium

PBS – phosphate buffered saline

SGM – smooth muscle cell growth medium

GOF – goodness-of-fit

HG – Henyey-Greenstein

MC – Monte Carlo

MCML – Monte Carlo Multi-Layer

EHF – extended Huygens-Fresnel

RTE – radiative transport equation

SS – single scattering

NIR – near infrared

CT – collimated transmission

FWHM – full-width at half-maximum

TE – tissue-engineered

FB – fibroblast

TIMP – tissue inhibitor of metalloproteinases

MT-MMP – membrane tethered matrix metalloproteinase

ANOVA – analysis of variance

dox – doxycycline

List of Symbols

μ_s – scattering coefficient

g – scattering anisotropy

μ_a – absorption coefficient

μ – attenuation

ρ – reflectivity

n – number of samples OR refractive index

$p(\theta)$ – scattering phase function

c_v – coefficient of variation

λ – wavelength

Abstract

The ability of optical imaging techniques such as optical coherence tomography (OCT) to non-destructively characterize engineered tissues has generated enormous interest recently. The engineered tissue of interest here is the collagen gel, wherein smooth muscle cells (SMCs) are embedded in a 3D collagen I matrix. This thesis focuses on characterizing collagen gels quantitatively, by measuring the optical properties – the scattering coefficient μ_s and anisotropy factor g – from OCT data by fitting the signal to a theoretical model. μ_s and g are macroscopic physical properties that provide information on the density and size of scattering particles in the sample (cells and collagen fibrils), respectively. To measure μ_s and g, OCT data from nanoliter-sized volume is averaged to produce a depth-dependent curve, which was fit to a model, yielding 2 observable parameters – attenuation μ and reflectivity ρ – which map back to the optical properties μ_s and g.

Collagen gels were imaged by OCT at various time points over a 5 day period, and their optical properties were evaluated. In the first 24 hours, scattering in collagen gels is dominated by the collagen fibrils, which scattered light anisotropically, that is, mostly in the forward direction. However, over a 5 day period, the optical properties of collagen gels showed a 10-fold increase in reflectivity with no change in attenuation. Such changes imply a decrease in anisotropy g, which cause an increase in backscatter

and imply an increase in the number of small scattering particles in the collagen gels. In trying to assess what caused the measured changes in optical properties, the activity of matrix metalloproteinases (MMPs) was identified as responsible for the anisotropy decrease. MMPs degrade the collagen matrix, breaking down collagen fibrils, which scatter light anisotropically, into small fibril fragments, which scatter light more isotropically.

These findings are supported by follow up experiments in which MMP activity was altered in cellular and acellular gels, as well as experiments with the cells concentrated on one side of the collagen gel which enhanced the effect SMCs and MMP activity have on the scattering properties. All in all, these data show that SMCs embedded in a collagen gel express and activate MMPs, that these MMPs act locally to degrade collagen fibrils into smaller fragments, and that OCT can visualize and quantify the entire process.

Chapter 1: Measuring optical properties from engineered tissues: why and how

1.1. Introduction

The idea of extracting quantitative information from optical measurements on biological samples is a growing trend in many biomedical applications [1]. There are many parameters biologists are interested in that can be measured with optical technologies. These include (but are not limited to) assessing the functionality of a tissue, the biochemical composition of the sample, as well as the size, shape, and localization of cells. Optical technologies offer several technological advantages that many biologists find appealing. Optical measurements are often both non-invasive and inexpensive, which enable making repeated measurements on the same specimen without damaging it. Other technical advantages are more specific to different technologies. For example, microscopes have a fine spatial resolution (~μm), which allow for making highly localized measurements, while instruments in spectroscopic applications have a fine spectral resolution (~cm^{-1}), which allow extracting information on the biochemical composition (i.e., proteins, glucose, etc.) of the sample.

One biomedical application with a particularly pressing need for quantitative optical methods is tissue engineering. While the field of tissue engineering has advanced

rapidly in the last 2 decades, the issue of quality control has emerged as a critical challenge that must be overcome [2]. Quality control requires testing the engineered tissue prior to implantation, since engineered tissues are dynamic structures that constantly interact with their surroundings and thus change over time. However, most current techniques for characterizing engineered tissues are limited either by their destructive nature, their requirement of adding expensive labels to the sample, or by their ability to make macroscopic measurements only with no ability to assess local variations in the sample [3-6]. Given these limitations, optical technologies that characterize engineered tissues non-destructively are particularly appealing.

One optical imaging modality that shows exceptional promise in tissue engineering applications is optical coherence tomography (OCT) [7]. OCT systems are modified Michelson interferometers in which scanning optics were integrated into the sample and reference arms. The guiding principle behind OCT is low-coherence interferometry, wherein the axial resolution is determined by the temporal coherence length of the source. Using a broadband source with a short coherence length enables attaining fine axial resolutions of ~10 μm. Changing the delay in the reference arm enables probing different depths in the image, creating an A-scan or depth-scan; scanning the sample arm beam laterally between successive A-scans creates a 2D map of the tissue cross-section.

While OCT images provide qualitative visual information on biological samples such as engineered tissues, quantitative approaches that characterize the sample based on physical principles are often preferred. The methodology proposed in this thesis is to measure the optical properties from OCT signals. Numerous theoretical models [8, 9] of OCT have shown that the OCT signal is determined by the optical properties of the imaged medium and the sample arm optics. Since the sample arm optics are constants that are known *a priori*, it is possible to fit the signal to a theoretical model and thereby extract out the optical properties. This method of measuring optical properties was used throughout the thesis to characterize remodeling in one of the most common types of engineered tissues, collagen gels [10].

1.1.A. The basic idea

As an imaging technology, OCT can provide high resolution visualization of the imaged sample's cross-section, thereby allowing qualitative assessment of the sample as it develops. However, qualitative monitoring of engineered tissue development is at times insufficient. An example of this is shown in Fig. 1.1A, which displays 2 OCT images of collagen gels, one at 6 hours and one at 5 days. The color-scale of the images was calibrated to units of reflectivity to enable a direct comparison. In the 6 hour image, small bright structures that represent cells or clusters of cells are seen in the foreground throughout the gel. The collagen matrix in the background is slowly varying (i.e., low spatial frequencies) and signal-poor. However, at 5 days it is difficult to identify any structures in the image. All that is seen is a superficial signal-rich region that attenuates with depth. The poor visualization seen in the day 5 gel is a consequence of gel development and remodeling, which caused a change in its optical scattering properties. In general, it is of greater interest to characterize mature developed engineered tissues that are ready to be implanted than tissues that still need to be grown for weeks or months. Thus, there is a need for quantitative analysis of the OCT signal in order to extract information from the data that will help characterize the sample in a more objective manner.

In order to extract the optical properties from the image, the signal from multiple adjacent A-scans (outlined by a white dashed line in Fig. 1.1A) is averaged laterally, resulting in an averaged A-scan. An example averaged A-scan is shown in Fig. 1.1B (black line). Next, the sample interface (the peak in Fig. 1.1B) is identified as a point of reference. At this point, the axial range over which the signal will be fit is determined (blue thick line in Fig. 1.1B). This signal is then fit to a theoretical model. In this thesis, the μ-ρ model [8] is used, which is described in Ch. 2. The fit results return the attenuation and reflectivity of the sample, which correspond to the slope and intercept of the natural log of the fitted signal.

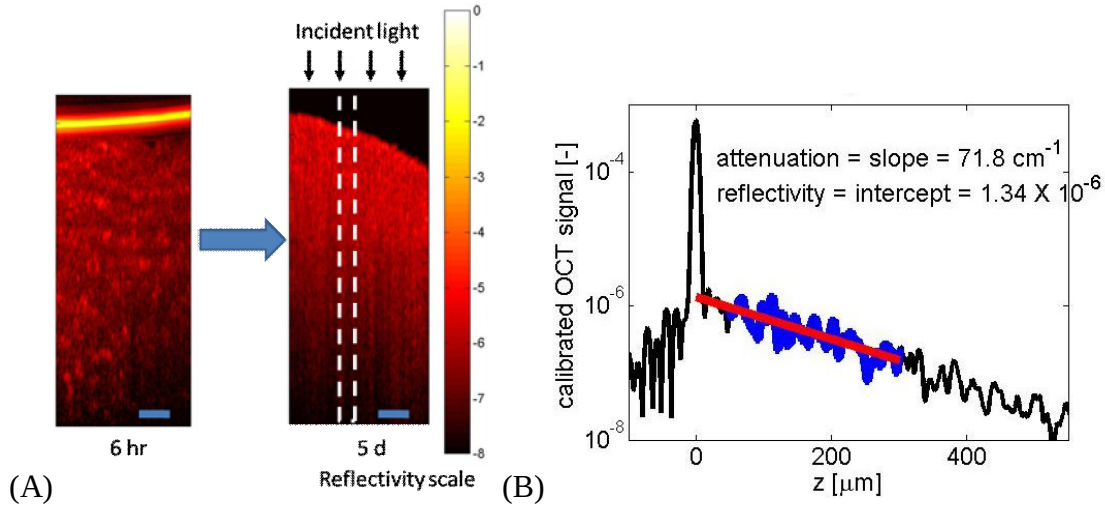

Fig. 1.1: Example calibrated OCT images of collagen gels at 6 hours and 5 days, plotted on a log scale. At 6 hours, one can see small bright structures that represent cells atop a low signal background. At 5 days, it is difficult to see any structures in the OCT image. However, it is clear that the signal attenuated from the top to the bottom of the sample. The method used the in this thesis quantitatively analyzes the attenuation and reflectivity in OCT images. The signal from selected A-scans (outlined in white dashed line) is averaged laterally across the image, resulting in an averaged A-scan. (B) Depth-dependence of a representative averaged A-scan. Selected pixels along the depth (z) direction (blue) are fit to a theoretical model. The fit is shown in red. The slope of the fit represents the attenuation, and the intercept represents the reflectivity, which together map back to the optical scattering properties of the sample.

1.2. Light transport in tissue

Much of this thesis revolves around measuring the optical scattering properties that are measured from OCT data. This section introduces and defines these properties, and details some common methods to measure them. A more thorough review of optical properties is found in [11]; a survey of the measurement techniques is found in [1].

1.2.A. Optical scattering properties

When light enters a turbid medium such as tissue, small local fluctuations in the refractive index of biological structures cause the light to scatter in many different directions. Examples of biological scattering particles are cells and organelles, as well as extracellular matrix components such as collagen fibers. Moreover, the scattered light is not distributed uniformly in all directions; the directionality of the scattered light, which is important in guiding light transport in tissue, is determined by particle size, shape, and refractive index mismatch. In addition to scattering, the light can also be absorbed by specific chromophores in the tissue. However, in most tissues at visible and near infrared wavelengths, scattering dominates absorption.

The most important optical properties that describe light transport in tissues are summarized in Table 1.1. These optical properties are macroscopic physical properties that describe a volume within a material. The scattering and absorption coefficients describe the inverse of the average distance between successive scattering and absorption events, respectively. While μ_s and μ_a are rather simple to conceptualize, understanding $P(\theta)$ and g is not straightforward. A schematic that illustrates both $P(\theta)$ and g within the context of a single scattering event is shown in Fig. 1.2. Here, it can be seen that the scattered light (blue arrows) is more forward-directed than isotropic. The forward component for each of these scatter trajectories is given by $\cos(\theta)$. The anisotropy factor g is the mean value of this forward component (red). Note that $P(\theta)$ characterizes the energy distribution along polar angles in the plane of the paper, but not along azimuthal angles ψ which are perpendicular to the original light trajectory. Frequently, light scattering is assumed to be symmetric in azimuthal directions; however, this assumption is not always true in tissue [12].

In general, calculating $P(\theta)$ for an arbitrarily shaped particle is an ill-posed problem. In fact, the only exact calculation of $P(\theta)$ exists for spherical particles (and infinitely long cylinders) in what is known as a Mie calculation [11]. Mie theory shows that small spheres scatter light isotropically (lower g) while large spheres scatter light

anisotropically (higher g). Moreover, Mie calculations, which are based on spherical harmonics and Bessel functions, result in P(θ)'s that have multiple lobes. However, in real tissues P(θ) is smooth and can be adequately described by the Henyey-Greenstein phase function [13]:

$$p_{HG}(\theta) = \frac{1}{4\pi} \frac{1-g^2}{\left(1+g^2-2g\cos\theta\right)^{3/2}} . \qquad (1.1)$$

Table 1.1: Summary of tissue optical properties.

Name	Symbol	Units	Description
Scattering coefficient	μ_s	cm^{-1}	This parameter is defined as 1 / (the average distance between successive scattering events). μ_s provides an indirect measure of the particle density. High μ_s values imply the scattering events are close together, while low μ_s values imply they are further apart.
Scattering phase function	p(θ)	–	A probability density function that describes the distribution of scattered energy along polar angle θ. p(θ) is defined for 0<θ<180° and is normalized such that $\int p(\theta) 2\pi \sin\theta d\theta = 1$. In general, tissues scatter light mostly in the forward direction and thus p(θ) is higher at smaller angles than large angles.
Anisotropy of scattering	g	–	Describes the forward component of the scattered light. g is defined as the expectation value of the cosine of the polar angle of the scattered light, i.e., g = ⟨cos(θ)⟩. Since tissues scatter light mostly in the forward direction, g is often closer to 1 than 0.
Absorption coefficient	μ_a	cm^{-1}	Defined as 1 / (the average distance between successive absorption events). Similar definition to μ_s, but μ_s and μ_a describe different physical phenomena. Moreover, for most tissues, $\mu_s >> \mu_a$.

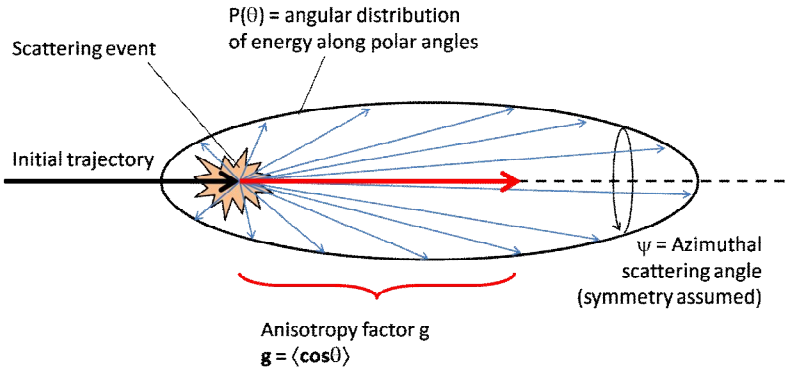

Fig. 1.2: Scattering phase function P(θ) and anisotropy factor g. Blue arrows represent the trajectories of the scattered light, which are mostly in the forward direction. The mean forward component, representing g, is shown in red.

Fig. 1.2 presents a simple description of single light scattering event. However, in reality when a beam of light enters tissue there are so many scattering events that any individual scattering event is greatly overshadowed. In general, light transport in tissue can be adequately approximated by the laws of diffusion as energy particles moving down a concentration gradient. Here, the directionality of the scattering defined by P(θ) get blurred away and the scattering is guided by a only single parameter, the reduced scattering coefficient $\mu_s' = \mu_s(1 - g)$. Thus, in most optical property measurements, μ_s and g are linked and cannot be separated without additional information.

However, while most measurements of scattering involve diffusion and μ_s', the confocal imaging geometry common to confocal microscopy and OCT operates in different scattering regime. A summary of the various scattering regimes in tissue is shown in Fig. 1.3. The most common regime is the diffusion regime that occurs at optical depths $\mu_s z > 10$, in which the directionality of the scattering gets lost and individual scattering steps resembles a random walk. The single scattering regime ($\mu_s z < 1$) assumes that light that entered the tissue underwent a single backscattering event before leaving. Multiple scattered light ($1 < \mu_s z < 10$) is somewhere in between the diffusion and single scattering regimes, where the light maintains some its properties.

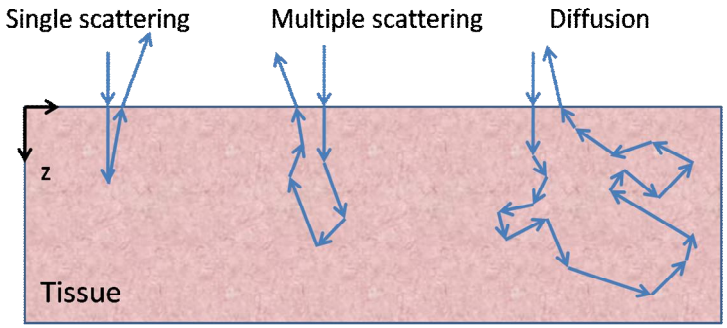

Fig. 1.3: Light propagation in the 3 different scattering regimes, with each blue arrow representing a single scattering event.

Reflectance-mode confocal imaging operates mostly in the single scattering regime; OCT, with its larger penetration depth, operates in both single and multiple scattering regimes. Because these technologies operate in the niche prior to the diffusion regime, it is possible to make measurements that separate μ_s and g. Currently, no other method is able to measure μ_s and g at the same time. Note that it is widely assumed that in the single scattering regime, light transport in confocal and OCT signals is guided by only by μ_s; however, data presented in Ch. 4 challenges the current paradigm.

1.2.B. Current methods that measure optical properties

Several methods exist for measuring optical properties of tissues that were not used in this thesis but are nonetheless reviewed here for completeness. One very common method is the integrating sphere method [14], in which a thin tissue sample is placed on the port of a sphere that is coated with highly reflective material. The highly reflected coating on the sphere ensures that all the light that entered the sphere is collected by the detector, which is found inside the sphere. The integrating sphere can operate in either reflectance or transmission modes, depending on which sphere port is used (entrance port for transmission mode, exit port for reflectance mode). Together, the reflectance and transmission port measurements can be mapped back to 2 unknowns, μ_s' and μ_a, using either inverse adding doubling theory [15] or inverse Monte Carlo [16]. In order to separate μ_s' into μ_s and g, a third measurement is needed, the collimated

transmission. However, given the inherent difficulty of the collimated transmission measurement, many choose to omit it. Despite its widespread use, the integrating sphere has several key limitations. First and foremost, it requires thin (~μm) sections of tissue to measure the optical properties, which is at best difficult to prepare and often simply unavailable. Another limitation is that some scattered light leaks out the side of the port, which results in an overestimation of μ_a.

Another very common method is to measure the diffuse reflectance of light from the tissue. The simplest way to do this is to place 2 fibers closely together on the tissue surface and to measure how the light transport between them changes as the fibers are moved further and further apart, a so-called R(r) measurement. The equations that guide the light transport for a semi-infinite medium are detailed in [17]. Alternative methods to measure diffuse reflectance is to keep the fibers fixed in place and use a fast detector to obtain a time-resolve measurement [16], or to modulate the light at a certain frequency and study the propagation of photon density waves [18]. However, these methods utilize diffuse light, meaning that it is not possible to separate μ_s and g as they are both lumped into μ_s'.

Another common method to characterize biological samples is using goniometry [19], which measures $P(\theta)$. In this method, the angular dependence of light scattered off a thin tissue section is measured by a detector attached to a rotating arm. An alternative setup is to capture all the scattered light on a screen and map it from xy space to angle space [20]. Goniometry has the advantage of measuring both $P(\theta)$ and $P(\psi)$, however, it provides no information on either μ_s or μ_a. And like the integrating sphere method, goniometry has the disadvantage of requiring a preparation of ~μm thin tissue sections.

1.3. Tissue engineering: a field in need of non-destructive methods

The idea behind tissue engineering is to apply principles of engineering and the life sciences to develop biological substitutes in a laboratory in order to repair, replace, or regenerate organs and tissues whose functionality was lost due to damage or disease.

Currently, there is a clinical demand for donors of such tissues and organs, and demand far exceeds available supply. Tissue engineering was proposed as an alternative method to alleviate the demand for organ donors. However, despite very high initial expectations, the results from some of the preliminary *in vivo* trials with tissue engineered implants have been considered disappointing [21]. In analyzing and dissecting the causes of the failures on tissue engineered implants, it was concluded that point failures are a result of non-uniformity within the implant, and that better quality control is needed, specifically, methods for monitoring development that fully characterize the engineered tissue just prior to implantation [2].

A key element here is that engineered tissues are constantly evolving, responding to stimuli, adapting to their local microenvironment, and remodeling their scaffold matrix accordingly [21]. Moreover, there is great inherent phenotypic variability within cells, even cells that were isolated from the same tissue. In other words, preparing the 2 engineered tissues using the same scaffold and cells can still lead to 2 very different samples. Modulating cell phenotype is one of the key challenges in tissue engineering [21], and many of the stimuli that affect the cell phenotype occur in the local cellular microenvironment. Thus, for engineered tissues to become a viable clinical alternative, non-destructive tissue characterization methods are needed to improve quality control and monitor the samples as they develop and remodel their surroundings.

However, there very few techniques that can quantitatively characterize engineered tissues non-destructively. The most common conventional methods such as histology and electron microscopy are destructive in nature, allowing only end-point measurements. Similarly, many common mechanical tests also destroy the sample in the process. Imaging techniques such as magnetic resonance imaging and computed tomography are expensive and repeated measurements may lead to toxicity. Other common methods include labeling a molecule of interest with a fluorescent probe and monitoring it using fluorescence microscopy. However, this requires buying expensive fluorescent dyes and integrating them into the samples, and thus it is not cost effective to survey large volumes of tissue.

It is within this void that optical coherence tomography offers great promise [22]. Like many optical techniques, OCT is non-invasive and non-destructive, which allows users to make repeated measurements and monitor the engineered tissue development. The contrast mechanism in OCT depends on the endogenous mismatches of refractive index in the imaged sample, and thus no expensive labels are needed. The noise floor in OCT is roughly 3 orders of magnitude less that of confocal microscopy, which allows for imaging depths of up to 1 mm in highly scattering tissue samples. OCT is also very inexpensive relative to magnetic resonance and computed tomography imaging. State of the art Fourier domain OCT system designs [23] can image samples at rates much higher than video rate. Moreover, in OCT the axial and lateral resolution are independent, meaning that with a low numerical aperture objective lens is it possible to avoid the tradeoff between penetration depth and spatial resolutions common to many microscopy applications. Since OCT is fiber-based, it is possible to couple the technology to probes that can be integrated into the incubator for continuous monitoring of the developing engineered tissues for days and weeks.

While these features make OCT an ideal imaging technology for surveying engineered tissues, image analysis and interpretation remains a problem. Surveying and analyzing large volumes of engineered tissues is not trivial. Many images of developed engineered tissues are rather featureless, as multiple scattering degrades the spatial resolution. This thesis attempts to address these 2 issues by illustrating the utility of evaluating the optical properties from the OCT data. Using this method, it is possible to describe the tissue with numbers and analyze this numerical data statistically.

1.4. Organization of the thesis

This thesis is organized as follows: after this general introductory chapter which presented a brief overview of concepts common to the thesis, there will be 2 more focused introductory chapters. One of these chapters will present the μ-ρ theory of light scattering [8] in a confocal/OCT imaging geometries and develop the concepts used in

the rest of the thesis. The second specific introduction will describe the state of vascular tissue engineering, presenting both the state of the field and present challenges that remain to be overcome, focusing on the biology of the problem.

Four of the next 6 chapters represent manuscripts that have been submitted or will shortly be submitted to peer reviewed journals, and the fifth and sixth chapters will describe and analyze methods that are common to the thesis. Ch. 4 will address the effect anisotropy factor g has on confocal and OCT signals from the single-scattering regime, showing that anisotropy does indeed affect attenuation in the single-scattering regime. Ch. 5 will cover the algorithm used to measure optical properties, from the preparation of the data for fitting, through the fitting and analysis of the results. Ch. 6 presents a statistical characterization of the method of measuring optical properties from OCT data, specifically, demonstrating its accuracy and reproducibility. Ch. 7 will present an analysis of the optical properties of remodeling collagen gels imaged at various cell seeding densities and imaged at 8 different time points, showing a decrease in anisotropy (increase in reflectivity) over of the gels a 5-day period. Ch. 8 addresses the effect that matrix remodeling has on optical properties, and shows how blocking remodeling impeded the decrease in anisotropy over 5 days, while treating the day 1 acellular gels with collagenase partially reproduced the decrease in anisotropy measured at day 5 in the SMC gels. Ch. 9 assesses the effect SMC localization has on remodeling and the optical properties, by comparing the optical properties of collagen gels in which the SMCs were plated on top of the collagen to gels in which the SMCs were embedded in the collagen. The results showed a depth-dependence to the optical properties on the SMC side of the dual sided gels, which qualitatively correlated with cell migration seen in histology images. Finally, Ch. 10 summarizes the thesis and presents future directions.

1.5. Scope of the thesis

This thesis will discuss in detail how to measure optical properties from OCT data, and applications within tissue engineering. It is assumed that the reader has some familiarity with OCT systems, and system design will not be covered in detail. For more

details on the basic principles of OCT, see [24]. Moreover, rather than discussing hardware in detail, several key image-processing and statistical analyses algorithms are discussed in Ch. 5 since the novel methods in this thesis were computational. Discussions of algorithm design and computational efficiency are for the most part omitted for clarity. Additionally, the theoretical model (Ch. 2) and fitting algorithm (Ch. 5) also require that the sample be imaged under focus-tracking or quasi-focus-tracking conditions. This thesis does not discuss how defocusing affects the OCT signal or the fitted parameters, though this is an area of interest that needs to be explored. It is also assumed that the reader has some familiarity with confocal microscopy, which is used to image collagen gels in Ch. 7; however, it serves as supporting evidence, while the OCT data is at the heart of that chapter.

Chapter 2: A summary of the μ-ρ model in confocal microscopy and optical coherence tomography

2.1. Introduction

Many measurements in the field of biomedical optics involve trying to assess the optical properties of a tissue. This tissue can be thought of as an optically turbid medium that is described by its various properties: scattering coefficient μ_s, anisotropy factor g, absorption coefficient μ_a, and refractive index n. The underlying theme of this thesis is measuring the two optical properties that affect light transport most – μ_s and g – from confocal and OCT images by fitting the data to a theoretical model. In fact, Ch. 4-9 all include methods and analyses that originate with the theory that connects the optical properties μ_s and g to OCT signals through 2 observable parameters: attenuation μ and reflectivity ρ. This chapter develops μ-ρ theory to provide the reader with a sounder understanding of how OCT signals could be decomposed and quantitatively analyzed to provide a meaningful assessment of the state of the tissue, vis-à-vis measuring the tissue's optical properties. Most of the theoretical work presented here was developed by S. L. Jacques and his research group; the author's specific contributions are noted in the text. Nearly everything presented here is described in more details in [8].

Fitting OCT and confocal signals require analytical models that describe how the signal changes as a function of depth. In confocal microscopy, the only theory describing the signal as a function of depth has been single-scattering theory [25]. As the name implies, single-scattering theory assumes that the light has undergone only a single backscattering event at the focus, and that the light traveled ballistically to and from the focus. The single-scattering model is presumed to be valid up to a (one-way) optical depth $\mu_s z$ of 1, in which the light has experienced on average less than 1 scattering event.

In OCT, several analytical models have been developed, based on single-scattering theory [26-28], the extended Huygens-Fresnel (EHF) principle [9], and the small-angle approximation to the radiative transport equation (RTE) [29]. Both the EHF and RTE models are capable of separating focusing and coherent backscattering, as well as the effects that multiple small-angle scattering to and from the coherence gate have on the OCT signal. Including these features analytically add a great deal of complexity to these models. However, the EHF and RTE models are inherently different – the EHF model is in closed-form that can be fitted to using traditional non-linear least squares algorithm [30], while the RTE model is a set of open-ended equations that require computationally intensive genetic algorithms [31]. The EHF model is considered by many to be the most complete analytical OCT model to date. It is worth adding that both the EHF and RTE models are restricted to the small-angle (paraxial) approximation, meaning that it is only valid for tissue where $\theta < 30°$, or $g > 0.866$. Moreover, both the EHF and RTE models assume that in order to measure anisotropy, the fitted signal needs to reach the multiple-scattering regime ($\mu_s z > 1$), in which the signal cannot be approximated by μ_s alone and g begins to influence.

The μ-ρ model described in this chapter was derived from the inverse Monte Carlo method. Analytically, it is much simpler than EHF and RTE models while including some multiple scattering effects that these other models do not account for. There are a couple of distinctive features. First, most work based on fitting data using single-scattering theory is based on fitting 1 parameter, the total attenuation coefficient μ_t, and for most tissues at visible and NIR wavelengths, $\mu_t \approx \mu_s$. The μ-ρ model has 2

parameters, μ and ρ, which together can be mapped to μ_s and g. Importantly, this model illustrates how anisotropy affects single-scattered light, circumventing the need to image very deeply into the sample in order to accurately fit g. However, using the μ-ρ model requires implementing focus-tracking (or quasi-focus-tracking) conditions, which considerably slows down image acquisition and data processing.

This chapter develops the theory that is utilized throughout this thesis. Specifically, this chapter details how confocal and OCT signals can be described by 2 parameters – attenuation μ and reflectivity ρ – and it decomposes these parameters into their relevant terms. Moreover, the chapter briefly describes how anisotropy affects focusing and attenuation in the confocal and OCT geometry, as well as how a fraction of the scattered light is redirected back towards the detector. The chapter also provides details on how μ and ρ can be mapped through theory to the optical properties μ_s and g, and presents a grid that links (μ_s, g) to (μ, ρ) space that is used to display the fitted data.

2.2. Calibration

A biomedical optics measurement M can be decomposed, to a first order approximation, into 4 terms: a source term S, a transport term T, a collection efficiency term η, and a detector term D, such that

$$M = ST\eta D . \tag{2.1}$$

This equation is valid for both a measurement on a biological sample and a measurement on a calibration standard under the same experimental conditions. A calibration measurement could be a measurement on a phantom with predetermined optical properties, or of a simple oil-glass interface. Here we have

$$M_{calib} = ST_{calib}\eta_{calib}D . \tag{2.2}$$

Note that the source and detector terms are the same for both measurements. The term η describes the mathematically describes the spatial arrangement of the experimental setup, which also does not change between the measurement and the calibration. By taking the

ratio of these equations, the source, collection efficiency, and detector terms cancel out and we are left with

$$\frac{M}{M_{calib}} = \frac{T}{T_{calib}} = \frac{R}{R_{calib}}. \qquad (2.3)$$

When measuring optical properties, the term of interest is the transport term T, which describes how the light propagated from the source through the sample and to the detector. It is a function of optical properties μ_s, g, μ_a, and n. Note the ratio of transport terms T/T_{calib} is proportional to the ratio of signal terms R/R_{cailb}. R will be used to denote the OCT signal through the remainder of the chapter.

For confocal microscopy and OCT, which measure light backscattered off a sample, the transport term is the term of interest, since it is a function of the sample's optical properties. Given that the transport term is known *a priori* in the calibration measurement, the biological data can thus be calibrated by multiplying it by (R_{calib}/M_{calib}). This achieves the purpose of converting the data from arbitrary detector units into the dimensionless units of signal R. Below we describe R in terms of μ_s, g, and the system parameters.

2.3. Theoretical development: from Monte Carlo to analytical equations

The μ-ρ model was derived from inverse Monte Carlo (MC) method. MC methods model the stochastic process of light transport in a turbid medium by sampling probability density functions using a random number generator. Here, light is described in terms of small energy packets called "photons" that propagate (scatter) through the turbid medium and get slowly absorbed as they propagate. Thus, the underlying physical principle here is power transport, with the photons representing power. Some photons get completely absorbed while others escape outside the turbid medium. Those photons that do escape represent light that can be measured optically through reflectance- or transmission-based measurements. The source code for the MC simulations (in C) used to develop this model was written by S. L. Jacques [32], expanding on the subroutines originally developed in the famous Monte Carlo Multi-Layer code by Wang and Jacques

[33], and adapting it to the confocal geometry. It was hypothesized and experimentally determined that the μ-ρ model applies to OCT imaging as well.

In order to define equations of the μ-ρ model, the forward problem of light propagation in the confocal geometry was simulated using the MC method. The forward MC simulations behind the μ-ρ model describe a beam focusing into a depth z inside a semi-infinite turbid medium, described by a (user-defined) μ_s, μ_a, g, and n. The objective lens is characterized by numerical aperture NA. Based on their escape position and trajectory, the program determines if the photons will reach a pinhole and thus contribute to the signal. Multiple simulations were run, in which many of the parameters (μ_s, μ_a, g, z, NA) were varied. Each simulation resulted in a single data point that described the signal from that experimental condition. After running a large volume of simulations, certain patterns emerged of how the signal related to each of the varied parameters. These patterns were described analytically, as detailed here.

The confocal or OCT signal can be described as an exponential decay

$$R(z) = \rho \exp(-\mu z) \tag{2.4}$$

with,

$$\rho = \mu_s b(g) \Delta z\,, \tag{2.5}$$

and

$$\mu = 2G(\mu_s a(g) + \mu_a)\,. \tag{2.6}$$

The term Δz represents the axial resolution, and G represents the averaged pathlength relative to the imaging depth. In other words G is a geometrical factor that accounts for the extra pathlength off-axis light must traverse to get to and from the focus. The simplest approximation of G is:

$$G = \frac{1}{\cos\left(\sin^{-1}\left(NA/n\right)\right)}. \tag{2.7}$$

with (NA/n) representing the maximum launch and escape angle from the objective lens. However, a more careful analysis [8] shows that G actually depends on the optical properties and increases slightly with g. The term a(g) quantifies the fraction of forward-

scattered light that reaches the focus, while the term b(g) represents the fraction of light that is scattered in the backwards direction back towards the lens. Both a(g) and b(g) are approximated numerically in the μ-ρ model; however, these terms signify actual concepts more than simple numbers, and these concepts are described below in Sections 2.3.A and 2.3.B, respectively.

2.3.A. Attenuation and a(g)

The first concept discussed here is how anisotropy affects the observed attenuation. Currently, there is a wide consensus across existing analytical OCT models [9, 26-29], that in the single-scattering regime where $\mu_s z < 1$, the attenuation rate is influenced by μ_s (and μ_a), but not anisotropy g. Moreover, anisotropy only begins to affect the signal once it definitively enters the multiple scattering regime. However, the concept of a(g) in the μ-ρ model challenges this preconception by illustrating how forward-scattered light reach the focus and mitigate the observed attenuation. The author contributed in the development of this concept. The a(g) concept occurs independently of coherence gating effects, that is, the a(g) effect is found in confocal microscopy as well as OCT. Since this topic is expanded upon in Ch. 4, the discussion here will be relatively brief.

The principle that links anisotropy to the attenuation is illustrated in Fig. 2.1. Consider a photon energy packet propagating from the objective lens to the focus in a highly scattering and highly anisotropic medium. At some depth, the light will be scattered, but most of the energy will be scattered in the forward direction. From a MC perspective, there is a high probability that the scattered photon will deviate only slightly off its path to the focus and may even reach it. In fact, as $g \rightarrow 1$, photons may be scattered multiple times and still reach the focus as if they were not scattered at all. In such a case, it is not possible to distinguish part of the scattered light from unscattered light. However, in an isotropic scattering medium, only a small fraction of the light would still reach the focus and behave similarly to the unscattered light. Since the attenuation term is primarily affected by scattering to and from the focus, forward-

scattered light that still can still reach the focus (as is found in anisotropic scattering media) has the effect of reducing the observed attenuation. This effect by which the measured attenuation is mitigated in highly-anisotropic media is called a(g).

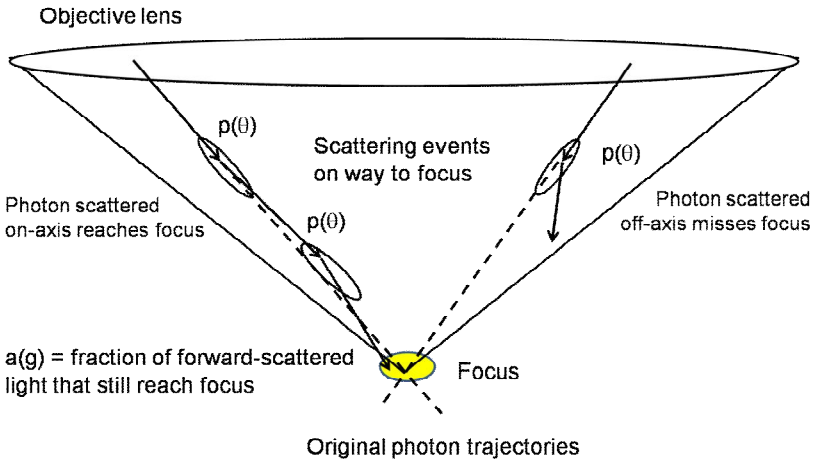

Fig. 2.1: Schematic of a(g), showing how photons scattered nearly on-axis can still reach the focus along with the unscattered light, while photons scattered off-axis will miss the focus, causing attenuation.

More details on exactly how a(g) is related to anisotropy are found in Ch. 4. Briefly, we found that the effect can be approximated numerically by

$$a(g) = 1 - \exp\left(\frac{(1-g)^{0.6651}}{0.1555}\right), \tag{2.8}$$

where a(g) is a multiplicative factor for μ_s in the equation determining attenuation μ. Graphically, plotting a versus g (Fig. 2.2) shows that for g values < 0.7, a(g) has very little influence on the observed attenuation. However, as $g \to 1$, a(g) decreases sharply towards 0, with $a(0.957) \approx 0.5$. Thus, in media where g > 0.9, forward-scattered light that still reaches the focus has the effect of decreasing the observed attenuation.

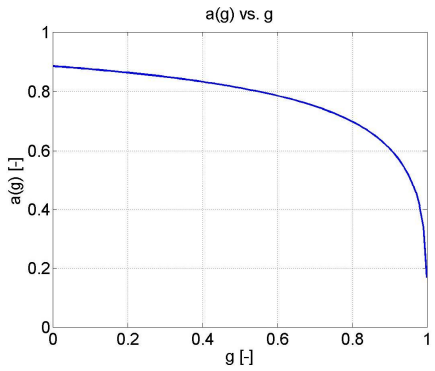

Fig. 2.2: Plot of a(g) versus g. Note that with low g values, a(g)≈1, meaning that the attenuation will be proportional to $2\mu_s$, while as g increases beyond 0.8, the attenuation approaches 0.

2.3.B. Reflectivity and b(g)

The second concept discussed here relates backscattering to reflectivity. From Eq. 2.5, it can be seen that reflectivity ρ is determined by scattering coefficient μ_s, axial resolution Δz, and the term b(g). The product $\mu_s\Delta z$ represents the number of scattering events (on average) that occur within the axial resolution of the imaging system. Note that the (system-specific) product $\mu_s\Delta z$ is typically less than 1. Also, recall that the axial resolution differs between confocal and low-coherence imaging systems. For confocal systems,

$$\Delta z_{confocal} = 1.4\frac{\lambda}{NA^2}, \tag{2.9}$$

where λ represents the laser wavelength. For OCT systems,

$$\Delta z_{OCT} = \frac{2\ln 2}{\pi}\left(\frac{\lambda_c^{\,2}}{\Delta\lambda}\right), \tag{2.10}$$

in which λ_c represents the central wavelength of the source and Δλ the 3 dB bandwidth of the source. Pilot studies in our lab have shown that integrating coherence gating into a confocal setup drops the noise floor by 3 orders of magnitude and greatly enhances the penetration depth, from 200-300 μm to 1-2 mm at 1310 nm.

The b(g) term determines the fraction of light scattered in the backwards direction relative to the total angular distribution of energy as described by the scattering phase function p(θ). This concept is described schematically by Fig. 2.3. Here, a scattering event (small yellow spot) occurs at the focus, and light is distributed spatially according to p(θ). While most of the light is scattered in the forward direction, a fraction is scattered in the backwards direction towards the lens. The blue region represents b(g), in other words, it is the overlap between p(θ) that falls within the collection geometry of the objective lens. Note that b(g) is dependent upon the maximum collection angle, which is the ratio of the numerical aperture NA to refractive index n. Thus, as NA increases, so does b(g).

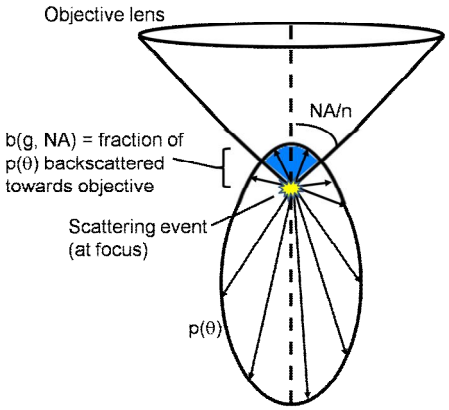

Fig. 2.3: Schematic of b(g), showing a scattering event at the focus and the angular distribution of energy p(θ). Note how only a fraction of p(θ) is backscattered towards the objective lens such that it can contribute to the signal.

Mathematically, b(g) can be defined to a first approximation by the equation:

$$b(g) = \int_{\pi - \sin^{-1}\left(NA/n\right)}^{\pi} p(\theta) \cdot 2\pi \sin(\theta) d\theta \,, \qquad (2.11)$$

which integrates p(θ) from [π-sin^{-1}(NA/n)] to π and accounts for the azimuthal component by including the 2πsin(θ) term in the integrand (Fig. 2.3). Note that this geometry assumes that the initial photon trajectory was on-axis, but that often photons are launched towards the lens off-axis. Truffer [34] has looked into the effects of off-axis launching on the overall b(g), and determined that Eq. 2.11 describes the overall b(g) term with sufficient accuracy.

In our analyses in this thesis, a Henyey-Greenstein (HG) phase function [13] is assumed. For completeness, the HG phase function is given by

$$p_{HG}(\theta) = \frac{1}{4\pi} \frac{1-g^2}{\left(1+g^2-2g\cos\theta\right)^{3/2}}. \qquad (2.12)$$

Using a HG phase function, the parameter b(g) was calculated for various values of NA and plotted in Fig. 2.4 on both a linear scale (A) and a log scale (B). For this thesis, the most important NA is in green (0.18), which represents the under-filled 10× microscope objective in our OCT system.

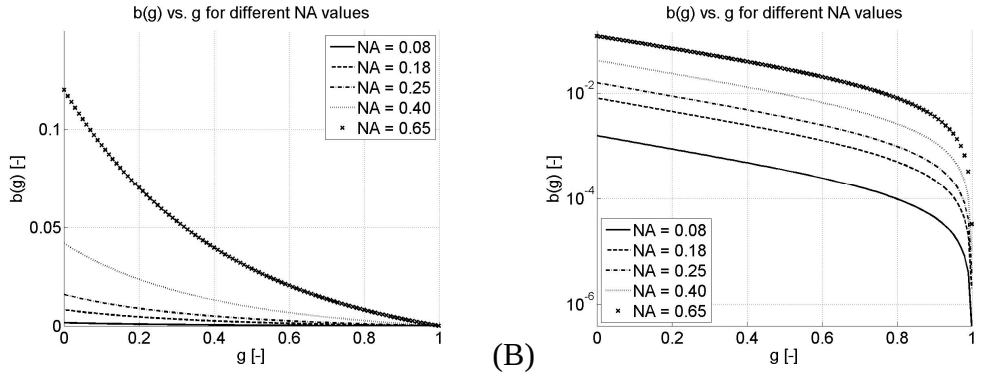

Fig. 2.4: Plots of b(g) versus g using an HG phase function for different NA values on a linear scale (A) and a log scale (B). The values of NA in the figure correspond to a low NA that is common to many OCT systems (0.08), the under filled 10× microscope objective in our OCT system (0.18), and over filled 10×, 20×, and 40× microscope objectives (0.25, 0.4, and 0.65, respectively).

It is worth mentioning that most tissues scatter light anisotropically and that typically b(g) is much smaller than the product $\mu_s\Delta z$. Consider for example, imaging a μ_s = 100 cm^{-1}, g = 0.9 medium with an NA = 0.25 objective lens and an axial resolution of 10 μm. In such a case, b(g) = 4.46×10^{-4} while $\mu_s\Delta z = 0.1$.

2.3.C. Mapping from (μ, ρ) space back to (μ_s, g) space

The parameters a(g) and b(g) make the mapping of (μ_s, g) to (μ, ρ) nonlinear and nontrivial. Yet in addition to the forward conversion from a given (μ_s, g) pair to a corresponding (μ, ρ) pair, the parameters a(g) and b(g) also enable making the reverse conversion from (μ, ρ) space back to (μ_s, g) space, and the author developed this methodology. The mapping assumes absorption is negligible compared to scattering. By dividing ρ by μ, we get

$$\frac{\rho}{\mu} = \frac{\mu_s \Delta z b(g)}{2G(\mu_s a(g) + \mu_a)} \approx \frac{\mu_s \Delta z b(g)}{2G\mu_s a(g)} = \frac{2G}{\Delta z}\left(\frac{b(g)}{a(g)}\right). \qquad (2.13)$$

The $2G/\Delta z$ is a constant for the imaging system. [b(g)/a(g)] is a monotonically decreasing vector that varies with g and follows the form of a double-exponential for $0 \le g \le 0.99$. In fact these double-exponential functions greatly resemble the b(g) curves shown in Fig. 2.4, since a(g) is close to 1 for most g values. Thus, by multiplying (ρ/μ) by ($\Delta z/2G$), one is able to solve for g, and thereafter solve for μ_s using Eq. 2.5.

2.3.D. Limitations of model

As with all theoretical models, the μ-ρ model described here has several limitations. The effects of multiple-scattering – the so-called turning of the corner by the signal on a log-scale [9, 29] – are missing. This is one of the primary disadvantages of the model, as it places a limit on the maximum fitting depth that depends on both the imaging system and the optical properties of the tissue. A second limitation is that for OCT imaging, this model assumes that the coherence and confocal gates are matched. Experimentally, this is not always the case, as fixing the focus can greatly increase imaging speed. Moreover, using an objective lens with a higher NA is advantageous for resolving optical properties, but this does not always improve image quality. A consequence of increasing the NA is that the depth of focus is limited, again reducing the depth range over which the optical properties can be measured. One way to overcome this is by implementing a focus-tracking (or quasi-focus-tracking) scheme, by shifting the

objective lens relative to the sample using a piezo-driven lens mount and imaging each site multiple times and stitching together the regions from each image that were in focus in software. The shifting objective lens approach was used in this thesis, though it did require a stitching algorithm to achieve the stitching task. However, these are all engineering tradeoffs; in this thesis, imaging speed and image quality were sacrificed in order to increase the dynamic range of the fitted parameters and thereby improve the overall accuracy of the algorithm.

2.4. Implications for fitting optical properties

There are several consequences of using the μ-ρ model to measure optical properties from biological samples. One major advantage is that Eq. 2.4 can be linearized by taking the log of both sides, which means that an exact solution exists for each fit. This eliminates the need for iterative algorithms and greatly reduces the computation time for each fit. Moreover, since every fit will have a solution, there will be no fits that do not converge to a solution, a drawback that occurs with both the EHF and RTE models. Also, because the μ-ρ model is not limited by the paraxial approximation, it is valid for isotropic as well as anisotropic turbid media. Another implication is that the model yields 2 fit parameters – μ and ρ – that can be mapped back to 2 unknowns, μ_s and g. Since anisotropy g was shown to have an effect on the attenuation even in the single-scattering regime, the fitting algorithm can now be designed to concentrate on the superficial pixels which have a high signal-to-noise ratio to evaluate g, rather than on the deeper regions in which the signal has "turned the corner". This feature is also useful for fitting g when the optical depth is below 1. Taken together, these features significantly enhance the ability to measure optical properties from confocal and OCT data.

2.5. Mapping experiment to theory: the (μ_s, g) grid in (μ, ρ) space

The physical meaning behind a(g) and b(g) may seem abstract, as do the observable parameters μ and ρ. However, a better understanding of how to interpret a

given (μ, ρ) pair can be obtained by plotting the (μ, ρ) pairs that correspond to a grid of (μ_s, g) pairs (Fig. 2.5). The grid covers a range of optical properties typically encountered in biological samples at visible and NIR wavelengths: $1 \leq \mu_s \leq 1000$ cm^{-1}, and $0 \leq g \leq 0.99$. Collectively, these points form a grid of iso-μ_s and iso-g lines in (μ, ρ) space, and can help provide a context for a given (μ, ρ) pair. Since the resulting values of μ and ρ values span over 3 orders of magnitude in μ and over 5 orders of magnitude in ρ, a log-log scale is used.

The grid plotted in Fig. 2.5 has several interesting features. First, it can be seen that for a given μ_s, as anisotropy g increases, the attenuation decreases; moreover, this decrease becomes sharper for $g > 0.9$, which is representative of most tissues at NIR wavelengths. Secondly, for a given μ_s value, the range of reflectivity spans about 3 orders of magnitude. This implies that the signal is highly dependent on anisotropy, and suggests that anisotropy plays a critical role in contrast in OCT images. And finally, since μ and ρ represent the measured observations, any experimental error in the measurement will be in (μ, ρ) space. Given the nonlinear mapping between theory and experiment, it can be seen that error in one measurement or another will have a nonlinear effect on the corresponding (μ_s, g) pair that corresponded to the fit.

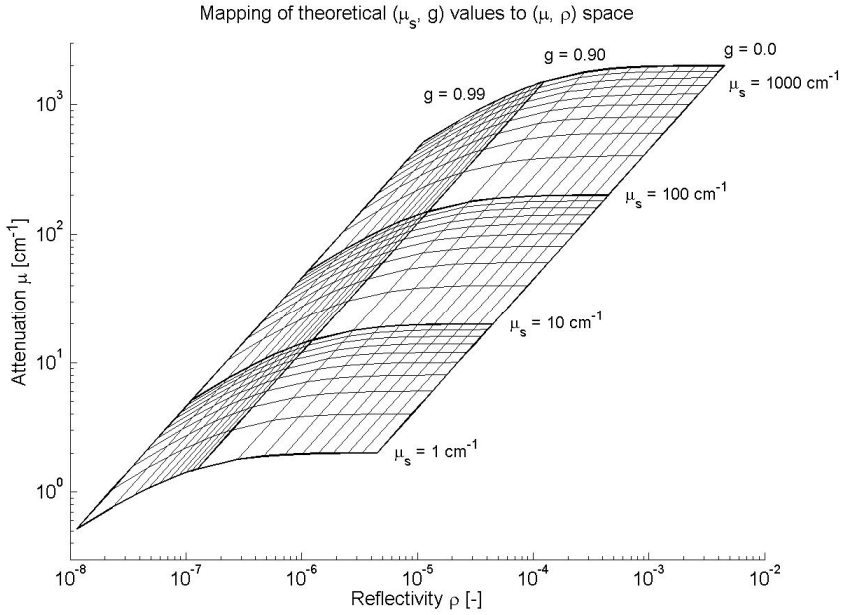

Fig. 2.5: Plot that maps a grid of theoretical (μ_s, g) values to (μ, ρ) space for the OCT system used in the thesis (Δz = 5.5 μm, NA = 0.18).

2.6. Summary

This chapter described some of the principles behind the μ-ρ model that describes confocal and OCT signals from turbid media as exponential decays with attenuation μ and reflectivity ρ. These 2 observations map nonlinearly to 2 unknowns, the scattering coefficient μ_s and anisotropy factor g. The signal can be converted from arbitrary detector units into dimensionless units of reflectivity by calibrating the signal against a sample of known reflectivity. The μ-ρ model also identifies the effect anisotropy has on focusing and attenuation in turbid media, which allows for evaluation of g without the need to image deeply into the tissue. Moreover, it describes how only a fraction of the light scattered at the focus is scattered in the direction that can be collected by the objective lens. Finally, a grid that maps theoretical (μ_s, g) pairs into (μ, ρ) space is shown which will assist in interpreting the fitted (μ, ρ) data. These principles form the underlying backbone of the computational methodology (Ch. 5) and are used throughout the thesis.

Chapter 3: Review of tissue engineering techniques for vascular applications

3.1. Introduction – why do people make engineered tissues?

Throughout the world, there is a growing demand to replace and repair organs and tissues that have lost functionality due to disease or damage [35]. Unfortunately, the supply of organs available for transplants does not meet the high demand for replacement tissues. There are many instances when current medical treatments are too costly, lack proven efficacy, or simply not available. Indeed, there is a demand for most tissue types, including blood vessels, cartilage, bones, kidneys, liver, pancreas, endocrine glands, neural glia, and many others [36].

Tissue engineering represents a paradigm shift in the manner of how patients are treated, in which tissues and organs that were grown in a laboratory are implanted in place of the damaged tissue. The purpose of tissue engineering is to replace, repair, or regenerate failing tissues or organs [21]. The term 'tissue-engineering' was coined in 1987 in a meeting of the National Science Foundation; however, research relevant to tissue engineering applications predates the coining of the term by decades [21]. As a field, tissue engineering applies and integrates concepts from biology, engineering, physics and chemistry, as well as the computational sciences. Given the interdisciplinary

nature of tissue engineering, and the complexities that exist at every step in the manufacturing process, the development of off-the-shelf tissue engineered products has been slower than initially hoped [2].

This chapter provides a brief review of tissue engineering, with an emphasis on vascular applications. It is intended to provide the reader with some background beyond the need to monitor engineered tissues non-destructively, which was discussed in Ch. 1. The scope of the discussion will be on the *in vitro* preparation of engineered tissues, focusing on interactions between the cells, the scaffold material, and the bioreactor. Additionally, some background is also provided on collagen gels and matrix remodeling within collagen gels, as both are relevant topics to this thesis. *In vivo* results of implanting tissue-engineered grafts in animals or patients, as well as the prospects of commercialization of tissue-engineered products, are beyond the scope of this chapter.

3.2. The 3 key facets of manufacturing engineered tissues

Typically, tissue engineering methodologies revolve around integrating 3 key components: the cells, the scaffold, and the bioreactor. The cells are grown or deposited on the scaffold material, which is then conditioned in a bioreactor for some period of time. One must master each of these critical facets both individually and collectively, as all 3 components interact with one another (Fig. 3.1). Integrating them together in order to have successful, reproducible outcomes is in a way a careful balancing act.

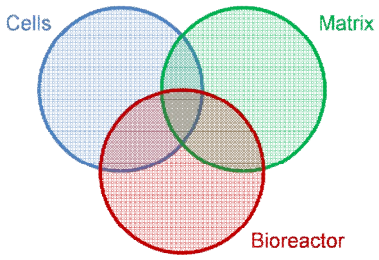

Fig. 3.1: The inter-relationship between the 3 facets of tissue engineering.

However, once one manufactures an engineered tissue, the big question becomes how does one assess whether tissue functionality has been achieved? Often, the

properties of interest in engineered tissues are biological, i.e., cell number or protein expression, or mechanical, i.e., size, linear modulus, toughness, or ultimate tensile stress [37]. To properly restore tissue function, the implanted engineered tissue must (approximately) match those of the native tissue.

Also important in the design of tissue engineered products is the issue of biocompatibility. Biocompatibility means the engineered tissue must be nonthrombogenic, nonimmunogenic, resistant to infection, integrate into the body, as well induce a healing response that does not lead to inflammation [38].

3.2.A. Cells

Differentiated cells that perform specialized functions are a key component of most tissues, and thus restoring tissue function requires attaining the functional properties of the cells in question. However, for the cells to function as intended they must acquire a specified phenotype. For example, in an engineered artery, the smooth muscle cells (SMCs) should have the contractile phenotype typically found in healthy arteries *in vivo*, as opposed to the synthetic phenotype, which synthesizes matrix and proliferates, and leads to pathological conditions such as intimal hyperplasia [39]. Thus, the wrong phenotypic expression by cells in the implanted tissue can lead to failures. Cell phenotype depends on the biochemical and biomechanical microenvironment, including the cells' extracellular matrix, as well as the cell source [39].

While using differentiated cells in engineered tissues is advantageous from a functional perspective, these cells must come from an autologous source in order to avoid an immune rejection of the implant, and such autologous sources are not always accessible. Alternatively, undifferentiated stem cells offer promising features, namely, finer control over the cells' phenotype within the selected differentiation pathway. However, undifferentiated stem cells are not always accessible in the adult host, and the use of allogenic (or xenogenic) cells can result in immunogenicity issues, as cells that do not come from the patient can illicit an immune response that may lead to rejection of the

implanted tissue, which one would like to avoid. It is worth noting that the degree of differentiation of the cell source may impact the overall cell function [21].

Thus, the source of cells used is critical, and the variables to consider are case specific since the optimal clinical strategies for restoring, replacing, and regenerating all differ from one another [21]. The key to remember is that there is a great heterogeneity within cells, even those harvested from the same location on the same organ. Table 3.1 lists possible sources of cells for tissue engineering, and comments on their applicability in terms of a clinical and manufacturing perspective [21].

Table 3.1: Possible source for cells employed in tissue engineering. From [21].

Cell source	*Comments*
Autologous, differentiated cells	No issue of immunogenicity, but this approach only leads to an off-the-shelf product or strategy if recruited directly from the host
Allogeneic, differentiated cells	Can provide for an off-the-shelf product or strategy, but in many cases will need to employ a strategy for engineering immune acceptance
Adult stem cells/progenitor cells	If recruited from the host to an acellular substitute or delivery vehicle, can provide for an immune acceptable, off-the-shelf product or strategy
Embryonic stem cells	When differentiated, as allogeneic cells there will be a need for an immune acceptance strategy; however, there is the potential for an off-the-shelf available product or strategy

3.2.B. Scaffold

In order to create a 3D structure that resembles a tissue, a scaffold material is needed to provide structural support for the cells, filling the role of the extracellular matrix. Scaffold materials can be either natural (i.e., collagen, fibrin, chitosan) or synthetic (i.e., poly(lactic acid), poly(glycolic acid)). Since the scaffold will go into the body, it needs to be biocompatible.

Natural biopolymers are advantageous in the sense that they are biocompatible. They are also abundant, and their interactions with cells *in vitro* are well characterized. The main disadvantages stem from the fact that these biopolymers are natural. All biopolymers have some heterogeneity, and exerting the fine control needed for medical

applications on a mass-production scale is ill-posed. There may also be some immunogenicity problems since many of these proteins come from animal sources. Recombinant technologies, which have shown promise in mitigating some of these issues, greatly increase the cost.

In contrast to natural biopolymers, synthetic polymers are industrially produced, which has advantages in terms of having fine control over material properties and tailoring them to a specific application. One common sought-after property is mechanical strength. On the other hand, non-biodegradable synthetic polymers such as expanded polytetrafluoroethylene (ePTFE or Teflon) and polyethylene terephthalate (PET, or Dacron) have the necessary mechanical strength, but poor interactions between the material surfaces and the body can lead to adverse reactions and ultimately failures [40]. Indeed, despite higher levels of quality control associated with non-biodegradable synthetic materials, their levels of biocompatibility often do not match the body's needs. In short, as with natural biopolymers, the options of synthetic scaffold materials are limited and require making engineering tradeoffs.

3.2.C. Bioreactor and construct conditioning

Creating functional engineered tissue replacements is more complicated than just mixing together cells and scaffold materials. The implanted engineered tissue needs to have the proper mechanical properties since the biomechanical environment of the cells will affect their phenotype [39] and the wrong environment could lead to failure. It is therefore necessary to condition the engineered tissue in a bioreactor in order to prepare it for the mechanical load it will encounter *in vivo*.

As with the cells and the scaffold material, the correct bioreactor design is application and treatment-specific. For example, the *in vivo* hemodynamic load that an engineered blood vessel needs to be conditioned to withstand differs from the typical *in vivo* mechanical load that engineered bone needs to be able to handle. As engineered

tissues develop in the bioreactor, the scaffold and bioreactor interact with the cells and modulate their phenotype, enabling them to properly remodel the scaffold matrix.

3.3. Vascular applications

Given the large number of tissue engineering applications and the limited space of this review, one application will be discussed in more detail – vascular engineering – highlighting both the progress made and the challenges that remain. However, it is important to note that the optical property measuring method discussed throughout the thesis can be applied to many other types of engineered tissues.

Cardiovascular disease is the leading cause of mortality and morbidity in the industrialized world, accounting for nearly 1,000,000 deaths in the US every year [35]. There are several ways to treat arteries that become partially or fully occluded. One way is to open the artery up by dilating a balloon in the distal end of a catheter. Often times, the artery is propped open using a metal mesh tube called a stent. Both balloon angioplasty and stenting are useful when the artery is partially occluded; however, a fully occluded artery requires providing an alternative conduit that bypasses the original artery and delivers blood to the target organ.

The National Center for Health Statistics estimates that last year 448,000 coronary artery bypass procedures were performed on 253,000 patients in 2006 in the US alone [41]. Autologous vessels (i.e., the saphenous vein), remain the standard for small diameter grafts; however, accessing these vessels in many patients has proven to be difficult because of vascular disease, amputation, or previous harvest [38, 42]. Available replacements of these small-diameter arteries (<6 mm) have performed poorly in terms of thrombogenicity, intimal hyperplasia, aneurysm formation, infection, and progression of atherosclerosis [43]. Given the high impact of the disease, there is a pressing need to develop such a therapeutic alternative. For these patients, tissue engineered blood vessels (TEBVs) hold considerable, if unmet, promise [21].

The ideal TEBV must contain a confluent endothelial layer, differentiated quiescent SMCs, and mechanical integrity and elastic moduli that retain sutures and tolerate systemic arterial pressures [42]. Designing and preparing such a TEBV poses several challenges. The first challenge is shape – here, the scaffold material in which the cells are deposited needs to be shaped as a tube, not a slab. As the vessels' (arteries') main function is to push blood along to the target organs, they contract and expand with systole and diastole. Thus, to restore the vessels' contractile abilities, smooth muscle cells (SMCs) need to be part of the tube-shaped TEBV. A second challenge has to do with endothelialization of the conduit, as an inner layer of endothelial cells (ECs) is required to provide a bioactive non-thrombogenic surface in which the blood will flow. Yet another challenge has to do with matching visco-elastic properties of the engineered construct to those of the surrounding tissue. Specifically, for the tissue-engineered blood vessel to expand and contract elastically there needs to be a layer of elastin present in the tube-shaped construct. And there is also the issue of mechanical conditioning in a properly designed bioreactor.

Ultimately, the challenges for creating TEBV are so great that engineering tradeoffs are necessary. There is a wide consensus that tissue engineered arteries must meet at least these 3 criteria [44]:

1. A component with high tensile strength that provides mechanical support (i.e., collagen fibers).
2. An elastic component that allows for recoil and prevents aneurysm (i.e., elastin).
3. A confluent endothelial layer that prevents thrombosis.

There are 4 main approaches to achieve these tasks: decellularized sheets (rolled up), cell sheets (also rolled up), synthetic polymer scaffolds, and biopolymer scaffolds [38, 45]. The remainder of this section will focus on biopolymer scaffolds, as they are most relevant to this thesis.

The concept of a tube-shaped tissue-engineered vessel was introduced when Weinberg and Bell first created a 3 layer, tissue engineered vessel structure that contained an intimal layer covered by ECs, a SMC-laden medial layer, and a fibroblast populated

adventitial layer [46]. The layers were prepared sequentially. Typically, the medial layer was prepared by casting a collagen gel in an annular mold that within 1 week produced a tubular lattice around a central mandrel. Fig. 3.2 shows a schematic representation of how the medial layer was prepared [38]. Once the medial layer was completed (1 week's time), a Dacron sleeve was placed outside the resulting tube to provide mechanical support [38]. The outer (adventitial) layer was prepared similarly to the medial layer, except fibroblasts instead of SMCs as the cell source; the outer layer was cast outside the Dacron sleeve. Finally, the EC layer was deposited on the inner surface of the medial layer by filling the tube with an EC-media suspension and rotating the tube for 1 week.

The next important development involved introducing bioreactors that mimic the flow that developing native vessels experience and condition the engineered vessel [42]. These TEBVs were conditioned in the bioreactor for 8 weeks under pulsatile flow that is similar to the flow conditions of embryonic development (as opposed to flow conditions in adults), during which most of the scaffold degraded and the SMCs produced their own matrix. Thereafter, ECs were deposited to cover the inner surface of the construct. Mechanical tests showed that the SMCs maintained their contractile phenotype *in vitro* [42], which is typically lost when harvesting cells and propagating them *in vitro* [47].

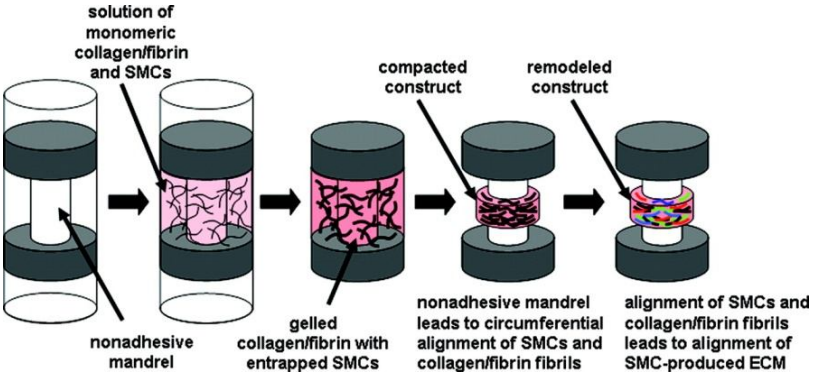

Fig. 3.2: Preparation of vascular construct. From [38].

Other key developments included the creation of a 3-layer, entirely biological tissue engineered artery made only from human cells [48]. Biochemical and mechanical stimuli were used to modulate the phenotype of SMCs [49]. A comparison of mechanically conditioned and unconditioned vascular constructs is found in Fig. 3.3,

which shows differences in the size and shape of the construct. Mechanical conditioning was also shown to change the mechanical properties of the constructs by altering remodeling [49, 50]. Using fibrin instead of collagen as the scaffold material was shown to induce the SMCs to express relatively high levels of both elastin and collagen [51], which ultimately improved the mechanical properties of the gels. Still, increasing elastin levels remains an unmet challenge in vascular engineering, since elastin is critical in determining the vessel's visco-elastic properties and regulating SMC phenotype within the TEBVs [52].

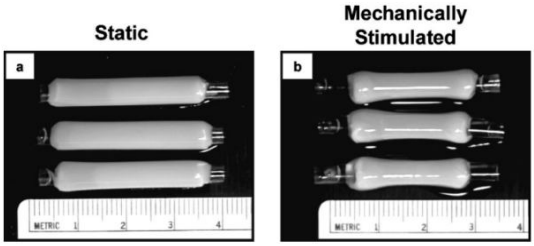

Fig. 3.3: Effect of 6 days of mechanical conditioning (10% circumferential strain, 1 Hz) on tube-shaped vascular constructs made from collagen I. Ruler units are in centimeters. From [49].

3.4. Collagen gels

Collagen gels are among the simplest and most common types of engineered tissues. Here, cells are embedded in a collagen I matrix and treated with the right media in order to achieve the desired structure and function. The most common cell type embedded in collagen gels is the fibroblast [53, 54], although SMCs and other cell types have also been previously embedded in collagen gels [55, 56].

In addition to tissue engineering applications, collagen gels also have cell biology applications [53, 54, 57]. These applications include studies of protein expression and function, cell adhesion and motility, cell-matrix interaction, as well as regulation of such processes. For example, fibroblast-populated collagen gels are used in wound contraction assays, which assess the ability of fibroblasts to contract the collagen matrix under different experimental conditions, i.e., in the presence and absence of a drug.

These contraction assays are used in several applications, such as when studying genetically modified mice that lack certain enzymes and there is a need to assess the remodeling capabilities of the cells [57].

When placed in a 3D collagen gel, fibroblasts assume a myofibroblast morphology, in which they express smooth muscle α-actin and myosin heavy chains. Additionally, they contract and remodel the matrix, both mechanically, by pulling on the collagen fibrils, and biochemically, by expressing and activating proteolytic enzymes that partially digest collagen fibrils. Both fibroblasts and SMCs are known for remodeling collagen gels once they are embedded in the gel. Specifically, the cells form focal adhesion sites where they attach to the collagen fibrils, and then (over days) they pull on the individual fibrils as the cells contract [58]. Cells pulling on the fibrils result in a reduction in both the volume and diameter of the (disc-shaped) gels, as well as an expulsion of fluid from the gel itself. This contraction of the gel is also referred to as gel compaction [37] or mechanical remodeling [59].

Despite their relative simplicity, there is an inherent heterogeneity in collagen gels. One reason for this is that the collagen solution itself is rather thick, and there are non-uniformities on both the micro and macro-levels. In fact, even acellular collagen gels contain some regions that are more scattering than others which can be seen with the naked eye. The second reason for the inherent heterogeneity of collagen gels is that during preparation, the time for mixing and aliquoting samples is limited to ~2-3 min once the collagen solution has been neutralized and before it thermally gels. This inherent short mixing time can cause the spatial distribution of cells to be non-uniform on the millimeter scale, and these initial non-uniformities translate into asymmetric remodeling later on. An example of such asymmetric remodeling is shown in Fig. 3.4, which shows 3 collagen gels at day 5 that were prepared at the same time with the same cells. It can be seen that each of these 3 gels looks differently than the others in terms of diameter and opacity; moreover, intrinsic variation within each gel is also quite obvious. A final source of heterogeneity within collagen gels is due to the (ill-defined) serum in

the media used to feed the cells, in which the biochemical composition varies between lots, adding another level of variability.

Fig. 3.4: Example of triplicate day 5 SMC-collagen gels. Note the differences in shape and size found within a single triplicate created at the same time with the same cells. The different levels of remodeling within these gels exemplify the inherent heterogeneity of biological samples.

3.5. Remodeling and MMP activity

One of the central topics in the thesis is collagen matrix remodeling by SMCs. In general, there are 2 types of remodeling – mechanical remodeling, which involves a reduction in the size of the collagen matrix as fluid is expelled, and biochemical remodeling, which involves proteolytic enzymes that degrade the local matrix [53, 59]. Mechanical remodeling describes the process by which cells pull on the collagen fibrils contracting the gel. Biochemical remodeling involves several groups of proteinases. One key family of enzymes is the matrix metalloproteinase (MMP) family. MMPs are a family of zinc- and calcium dependent endopeptidases with extensive amino acid sequence homology between its various members [60]. This section discusses MMPs, their activity, various functions, as well as inhibitors, and is intended to complement some of the biology-related discussions in Ch. 8-9.

MMPs play a role in many physiological and pathological processes, including development [61], cell motility [62], aging [63], wound healing [64], atherosclerosis [65], tumorigenesis [66], and fibrosis [67]. Not surprisingly, MMPs play a role in many tissue engineering applications as well [59, 68, 69]. In a way, one may consider the challenge in tissue engineering as a remodeling problem, with the matrix properties (i.e.,

biochemical composition, architecture) influencing the way in which the tissue is being remodeled [21]. As their name implies, the primary function of MMPs is to degrade the extracellular matrix. The matrix provides anchorage sites for cell adhesion that control cell viability and the cell cycle [70]. Since MMPs can modify these anchorage sites, MMPs exercise indirect control over cell viability and proliferation. Consequently, MMP activity must be tightly regulated to maintain homeostasis. Moreover, both deficient and overactive proteolysis can lead to disease progression [70]. Matrix proteolysis cascades resemble the multiple feedback system found in the coagulation cascades, with the product of one type of proteolysis activating or inhibiting other degradations [70]. For example, when MT1-MMP binds TIMP-2, they form a complex that is both a receptor and activator for MMP-2. Interestingly, the degradation of the extracellular matrix *in vivo* by MMPs is spatially confined to the pericellular space [70], even when the MMP in question is secreted.

Table 3.2: List of MMPs and their substrates. Modified from [70].

Enzymes	Other Names	Substrates[a]
MMPs		
MMP-1 MMP-8 MMP-13	collagenase-1 collagenase-2 collagenase-3	Col I, II, III, VII, X, GL, EN, LP, AG, TN, L-selectin, IGF-BP, Pro-MMP-2, -9, α2M, α1PI
MMP-2 MMP-9	gelatinase A gelatinase B	GL, Col I, IV, V, VII, X, XI, EL, FN, LN, LP, AG, galectin-3, IGF-BP, VN, FGF receptor-1, Pro-MMP-2, -9, -13
MMP-3 MMP-10 MMP-7	stromelysin-1 stromelysin-2 matrilysin	PG, LN, FN, GL, Col III, IV, V, IX, X, XI, LP, FB, EN, TN, VN, Pro-MMP-1, -8, -9, -13, α1PI, α2M, L-selectin
MMP-12	metalloelastase	EL, FB, FN, LN, PG, MBP, PL, α1PI
MMP-14 MMP-15	MT1-MMP MT2-MMP	Col I, II, III, GL, FN, LN, VN, PG, Pro-MMP-2, -13, α1PI, α2M
MMP-11	stromelysin-3	LN, FN, AG, α1PI, α2M

Abbreviations: aggrecan, AG; α1-proteinase inhibitor, α1PI; α2-macroglobulin, α2M; binding protein, BP; collagen type, Col; complement, C; elastin, EL; entactin, EN; fibrin/fibrinogen, FB; fibronectin, FN; gelatins, GL; hepatocyte growth factor, HGF; laminin, LN; link protein, LP; myelin basic protein, MBP; plasminogen, PL; proteoglycans, PG; tenascin, TN; vitronectin, VN; gelatinase A, 72 kDa gelatinase; gelatinase B, 92 kDa gelatinase.
[a] Substrates are grouped for similar enzymes, but not all of the proteins in each group are cleaved by all the enzymes in the group.

MMPs can be divided into collagenases (MMP-1, 8, 13), gelatinases (MMP-2, 9), membrane-tethered MMPs (MMP-14, 15, 16), stromolysins (MMP-3, 7), as well as other,

less common MMPs. Each of these MMPs has different substrates (Table 3.2) and thus different functions. Moreover, certain MMPs are associated with specific cell types. For example, MMP-8 is expressed by neutrophils while MMP-9 is expressed by macrophages, though we now know these MMPs are not exclusively expressed by these cell types [70, 71]. MMPs are expressed and synthesized in their pro-form, and are activated by cleavage of their pro-domain. The generic MMP has a pro-domain that is covalently bonded to the catalytic domain (Fig. 3.5). Two sequential cleavages of the pro-domain break the zinc-Cysteine bond; this frees up the (zinc-dependent) catalytic domain to begin its activity. Note however, that the catalytic domain differs between different members of the MMP family. For example, gelatinases have 3 additional fibronectin II repeats in the middle of their catalytic domain, while the MT-MMPs have a domain that anchors them to the plasma membrane [71].

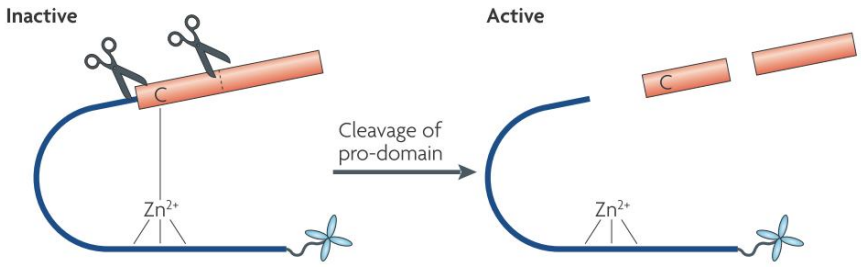

Fig. 3.5: Activation of a generic MMP. A conserved Cysteine in the pro-domain is bonded to the zinc ion, that is otherwise used for catalysis. Two cleavages in the pro-domain separate it from the catalytic domain and free up the zinc ion for proteolytic activity (adapted from [71]).

There are multiple inhibitors of MMPs, including a family called tissue inhibitors of metalloproteinases (TIMPs). Another natural MMP inhibitor is α_2-macroglobulin, which is a non-specific proteolysis inhibitor *in vivo* [72]. Since MMPs are activated by plasminogen conversion into plasmin, inhibiting this pathway also reduces MMP activity [70]. Additionally, there are also MMP-inhibiting drugs. For example, chemically-modified tetracyclines such as minocycline and doxycycline [73, 74] act non-specifically to block MMP activity through a mechanism that is independent of the site of antibiotic activity and is not well understood. Additionally, BB-94 is a potent synthetic inhibitor

that virtually nullifies all MMP activity [57]. These inhibitors help regulate MMP activity remains at physiological levels that are needed for homeostasis of the cell/tissue.

3.6. Concluding remarks

This chapter presented an overview of tissue engineering, focusing on the in vitro development of engineered tissues. The inter-dependence of cells, scaffold, and bioreactor in the manufacturing of engineered tissues was discussed. Special emphasis was paid to developing multi-layer TEBVs using biopolymers. Additionally, there was also a section on collagen gels, which are the template of many of these engineered vessels and are the engineered tissues imaged in Ch. 7-9. Finally, there was a brief discussion of remodeling and MMP activity, since remodeling and MMPs are discussed in Ch. 8-9. This summary should serve as a reference for the reader and fill in some of the missing information not detailed in later chapters.

Chapter 4: Effects of anisotropy of focusing and attenuation in confocal and low-coherence imaging in weakly-scattering media

This chapter was co-authored by Niloy Choudhury and Steven L. Jacques. A version of this chapter will soon be submitted to the journal Optics Letters.

Single-scattering theory has been one of the long-standing pillars of modeling the depth-dependence of confocal microscopy and optical coherence tomography (OCT) signals in turbid media. At its core is the assumption that at optical depths below unity, the signal is primarily composed of ballistic light that has undergone one (back)scattering event at the focus/coherence gate. Under such conditions, Beer's Law is presumed to be valid, and thus the signal follows an exponential decay:

$$I = \exp\left(-\left(\mu_s + \mu_a\right)L\right) = \exp\left(-2z\left(\mu_s + \mu_a\right)\right). \qquad (4.1)$$

Here, L is the pathlength (equaling twice the probing depth z), and μ_s and μ_a are the scattering and absorption coefficients, respectively. Beyond an optical depth of 1, the signal enters the multiple-scattering regime, in which both the signal decay rate and the lateral resolution are reduced. Note that absent from Eq. 4.1 is anisotropy factor g. However, previously both we and others [75] made unpublished observations that the initial decay in the OCT signal had some dependence on anisotropy. This effect was most evident when the anisotropy of the imaged sample was high, and the initial

exponential decay was less than expected. In this letter, we show that for OCT and confocal imaging systems, the initial exponential decay that the signal experiences in the single-scattering regime actually depend on anisotropy as well.

To illustrate this concept, multiple tissue phantoms made of polystyrene microspheres (Duke Scientific) embedded in agarose gels (Amresco) that had the same μ_s value but different g values were prepared and imaged. Using Mie theory, the sphere concentrations required for μ_s values of 20 cm^{-1} were calculated. The gels were sandwiched between 2 microscope cover slips separated by a washer. The phantoms were imaged using an OCT system that operated at 1300 nm with a 3 dB bandwidth of 100 nm (Δz = 5.5 μm) with an objective lens that had a numerical aperture (NA) of 0.18. More details on our OCT system can be found in [76]. To minimize defocusing effects on the OCT signal, a quasi-focus-tracking scheme was implemented. Here, the sample was imaged 11 times at the same site, with the objective lens successively shifted towards the sample by 40 μm each time. The regions of each image that were in focus were stitched together, forming quasi-focus-tracked 3D datasets that measure 350×300×1000 μm (xyz). Thereafter, the 3D data was subdivided into 10×10 regions of interest (ROIs), and A-scans from each ROI were averaged. The log of the averaged signal spanning $200<z<400$ μm was fit to a linear regression, in which the slope corresponds to the decay constant. The probability density functions (PDFs) of attenuations were calculated by binning the fit results into Gaussian shaped kernels. Fig. 4.1A show the distributions of slopes fitted from the 20 cm^{-1} phantoms with varying g values. There were 8 samples in total, 3 of g=0.73 and g=0.89, and 2 of g=0.62. It can be seen that despite the data falling within the single-scattering regime, as the anisotropy of the phantoms increased, the fitted slope decreased by roughly 15 %.

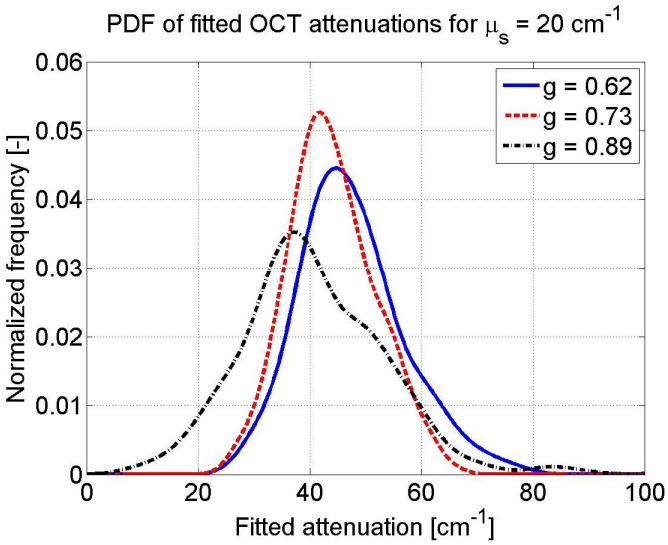

Fig. 4.1: Attenuation of agarose gel-polystyrene sphere phantoms of varying g values imaged by OCT. PDFs of fitted decay constant for phantoms with various g values with μ_s = 20 cm^{-1}.

Next, we sought to determine whether the anisotropy-dependent decay was caused by a coherence-related effect or by a focusing-related effect. To do this, we turned our OCT system into a confocal microscope by blocking the reference arm and setting the detector bandpass filter to DC. Imaging under these conditions, we obtained confocal axial depth profiles (consisting of 11 points) for the various phantoms. We hypothesized that if the effect was related to focusing it would be observed in the confocal signal (in which the signal decay is also supposed to be proportional to exp(-$2\mu_s z$)), but if the effect was coherence-related it would not. Fig. 4.2A shows representative depth-profiles from the given phantoms, and Fig. 4.2 shows the distribution of fitted slopes from the eight 20 cm^{-1} phantoms. Note that here we divided the 3D data into 5x5 ROIs. It can be seen that again the signal decay decreases as g increases, which supports the above observation that the anisotropy affected the ability of light to focus in a turbid media.

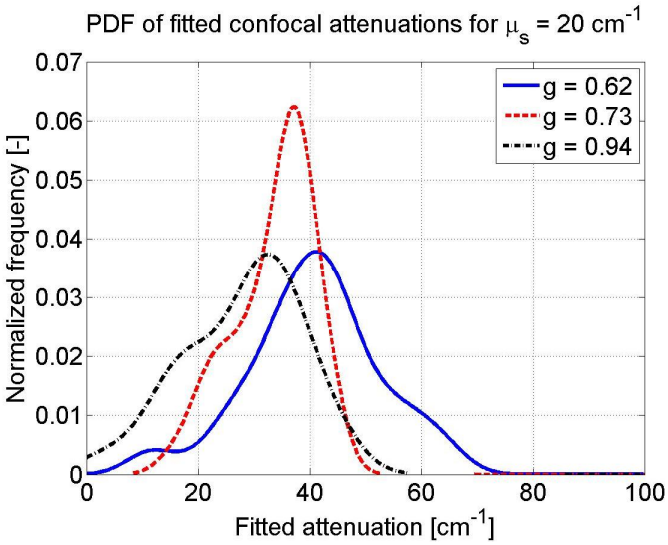

Fig. 4.2: Attenuation of agarose gel-polystyrene sphere phantoms of varying g values imaged by confocal microscopy. PDFs of fitted decay constant for phantoms with various g values with μ_s = 20 cm^{-1}.

The results shown in Figs. 4.1-2 run counter to existing analytical models. However, in trying to understand how anisotropy affects focusing and attenuation in confocal geometries, some insight can be gained from computational modeling using Monte Carlo (MC) simulations that mimic light transport in turbid media. Specifically, we adapted the famous Monte Carlo Multi-Layer (MCML) program to mimic a transmission-mode confocal microscope, in which photons simulating a converging beam are launched into an infinitely-wide slab of tissue. We chose a transmission mode setup since we are only concerned with photon travel to and from the focus, and not the backscattering events that are statistically/computationally inefficient. In these simulations, the turbid medium was shaped as a 400 μm thick slab with the focus 200 μm into the sample; the converging beam had a numerical aperture of 0.25. The intensity that would be collected by a pinhole on the transmission side of the slab was calculated by projecting the escaping photons (using their escape trajectories) back to the focal plane [77]. In these simulations, μ_s was varied from 0 to 52 cm^{-1}, and g was varied from 0 to 0.999. Fig. 4.3A shows the signal as a function of μ_s for selected g values, plotted on a log scale. Again, it can be seen that the decay rate decreases as anisotropy increases; moreover, the attenuation appears to be nearly 0 at g = 0.99. We then divided the fitted

slope for each g value by the fitted slope of the g = 0 case. This ratio, which we call a(g), is defined as the anisotropy-dependent factor that mitigates attenuation in the confocal imaging geometry; a plot of a(g) is shown in Fig. 4.3B. It can be seen that a(g) remains close to 1 for 0<g<0.8, but then begins to decrease towards 0, with a(0.964) = 0.5.

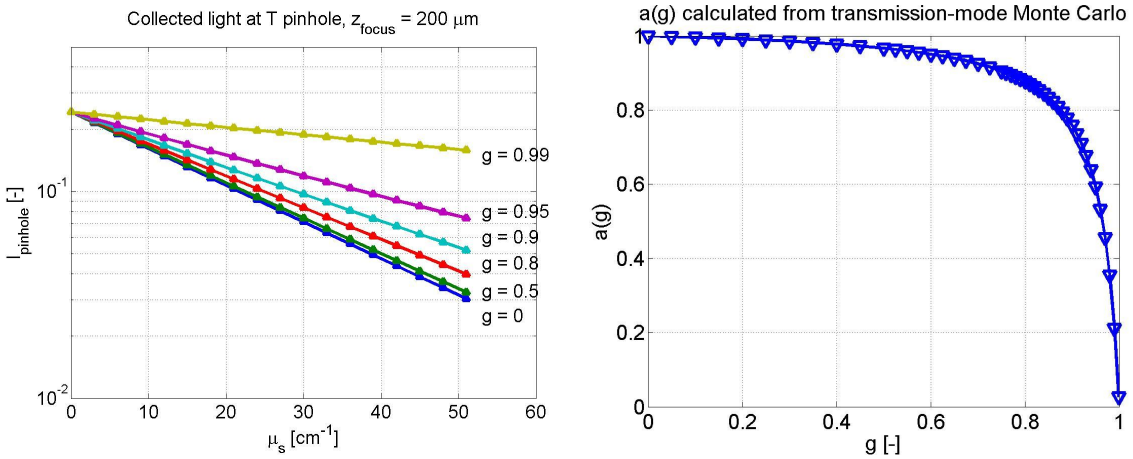

(A) (B)

Fig. 4.3: Monte Carlo simulations of the effect of anisotropy on transmission-mode confocal signal. (A) Plot of signal collected at transmission pinhole for a 400 μm infinitely wide slab with focal plane halfway at 200 μm. (B) Plot of decay rate for various g's normalized by decay rate when g=0.

In trying to conceptualize how anisotropy affects the ability of light to focus inside a turbid medium and what a(g) means physically, consider the scattering phase function p(θ). Typically, p(θ) is thought of as being on average forward-scattering, with the forward scattering component defined by g and the isotropic scattering component defined by 1-g. Similarly, one can think of p(θ) in terms of an on-axis component, which could still reach the focus despite the scattering, and an off-axis component that will not reach the focus (Fig. 4.4). The part of the light that is scattered at these very small angles will continue to propagate nearly in phase with the unscattered light to the focus where it will constructively interfere with the unscattered light. In other words, light scattered on-axis cannot be distinguished from the unscattered light. Thus, the more light is scattered on-axis (higher g), the more scattered light reaches the focus along with unscattered light, and the smaller the observed attenuation (Figs. 4.1-2).

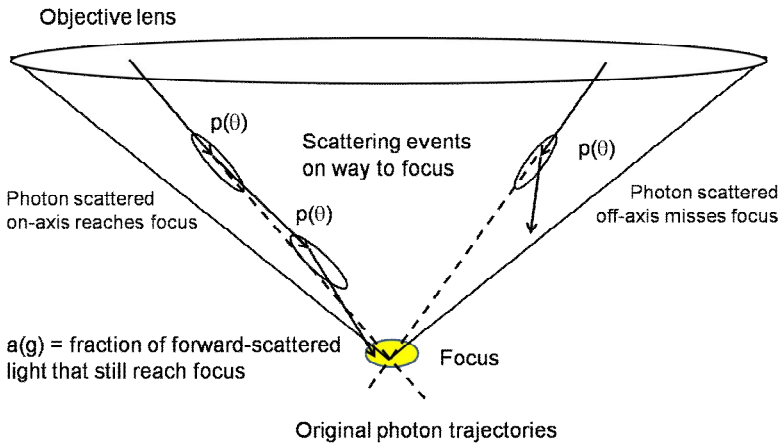

Fig. 4.4: Proposed mechanism of how anisotropy affects focusing in confocal imaging geometries. Light propagating towards the focus can undergo multiple small-angle scattering events and still reach the focus and hence does not contribute to the observed attenuation, while light scattered off axis misses the focus and does contribute to the attenuation.

Taken together, these experimental and computational results suggest that in confocal imaging of turbid media, the anisotropy of the sample influences the ability of light to reach the focus. Specifically, in highly anisotropic media, light scattered at very small polar angles can still reach the focus where it may not be distinguished from the unscattered light. Effectively, this leads to a reduction in the observed attenuation, and that in the single-scattering regime, the signal decay is better represented by

$$I = \exp\left(-2z\left(\mu_s a(g) + \mu_a\right)\right). \qquad (4.2)$$

In other words, we propose that in confocal imaging of turbid media, anisotropy and scattering are linked through the factor a(g), and that the product $\mu_s a(g)$ can be thought of as analogous to $\mu_s(1 - g) = \mu_s'$ that is found in the diffusion regime. Moreover, the effect anisotropy has on the confocal decay rate also applies to OCT systems, since the sample arm of OCT systems is essentially a confocal microscope. This effect, which is not trivial to model analytically, has eluded many researchers trying to understand the depth-dependence of confocal and OCT signals. These results suggest that special attention needs to be paid to the anisotropy of tissues when extracting optical properties from confocal and OCT data even when $\mu_s z < 1$, as many tissues have high g values wherein

a(g) could have a noticeable effect [25, 78-80]. Currently, further work in our lab is geared at elucidating how a(g) affects the optical properties extracted from confocal and OCT data.

In conclusion, we have shown that the even in the single-scattering regime, the anisotropy of the sample affects the signal attenuation in both OCT and confocal microscopy. Specifically, light scattered on-axis can more easily reach the focus where it cannot be distinguished from unscattered light, which effectively decreases the observed signal attenuation. Thus, both the scattering coefficient and anisotropy factor of the medium in question, in addition to the focusing properties of the lens, need to be considered when making quantitative measurements of light attenuation in confocal and OCT images.

Chapter 5: Selected computational methodologies used to fit optical properties from optical coherence tomography data

5.1. Introduction

The handling and processing of optical coherence tomography (OCT) and confocal microscopy data are critical steps that affect the evaluated parameters that were fit to the data. Here, the parameters of interest – attenuation μ, reflectivity ρ, as well as scattering coefficient μ_s and anisotropy factor g – come from the μ-ρ model described in Ch. 2. In general, most groups [25, 31, 78, 79] have been rather vague on what exact steps they take from acquiring the raw data to the figures and tables they publish. The purpose of this chapter is to provide the reader with some insight as to how to develop such an algorithm, using an engineering approach. The algorithm is written in Matlab (Mathworks), and it is assumed that the reader has a general knowledge of this language.

The OCT system used in this thesis was a time domain system, with very little elaborate hardware. The reference arm consisted of a rapid scanning optical delay line [81]. The sample arm contained an xy scanner and a piezo-driven objective lens mount to enable image acquisition at quasi-focus-tracking conditions. The electronic signal coming out of the detector is high-pass filtered at the detector; thereafter, the signal is digitized on a data acquisition card and stored on a computer. Given that most of the

methodological novelties in this thesis were computational and the (relatively) minimal hardware in the OCT system, this chapter will focus on these computational methods and present the relevant Matlab code.

One should keep in mind the objectives here: First, to convert raw data to a number of depth-dependent curves (averaged A-scans) that represent the calibrated OCT signal in a given volume of a sample; second, to fit the curves to the μ-ρ model; and third, to interpret and analyze the results. There are many ways in which one could achieve these 3 tasks. One need not use Matlab, but given's Matlab's robustness and widespread use, Matlab was chosen as the programming language used in this thesis. The author designed and wrote a unique algorithm for each OCT and confocal imaging system in our laboratory. This chapter presents a summary of the author's methodology to meet these objectives. In the discussion below, only the lines of code that are critical to computation are given; plotting and other display options are omitted.

In addition to highlighting the important computational methodology used to fit optical properties from OCT data, this chapter is intended to serve as a guide to someone trying to write an algorithm for measuring optical properties from OCT (or confocal) data. This chapter will cover data processing from the raw interferogram and proceed, step by step, through the segmentation of the data into regions of interest (ROIs), to the final (μ, ρ) display and analysis. Some of the presented subroutines are not original work by the author (as noted in the text), but are tabulated here given this chapter's aim for completeness.

The basic principles guiding the algorithm design are described in Section 5.2. Section 5.3 explains some of the pre-processing steps needed: forming a quasi-focus-tracked image, calibrating the data, aligning the sample in the image, and segmenting ROIs. Fitting the OCT signal from each ROI to the μ-ρ models is presented in Section 5.4, and some common analysis methods are discussed in Section 5.5. Sections 5.3-5 are all dedicated to data processing in 2 dimensions, since this algorithm addresses all the fundamental tasks while being simpler to conceptualize. Section 5.6 details the changes

need to be implemented in order to process 3D OCT data, and Section 5.7 discusses challenges that remain unresolved, routines that have yet to be implemented, and provide an outlook.

5.2. Basic principles

When trying to approach handling lots of data from an engineering perspective, there are a couple of governing principles that were used for guidance.

1) Standardization of names. The same algorithm was used to process all the data imaged by a particular OCT system, such that all the data underwent the same preprocessing steps, maintaining variable nomenclature across different subroutines. Moreover, all the intermediate result files followed a standardized naming system.
2) Modular design. The algorithm was divided into clear steps that were independent of one another. Each step had its own *.m file, which may have called other subroutines with their own *.m files. A simple master program called each step.
3) Detailed documentation. A copy of the data was saved before and after the manipulation that occurred in each step, which facilitated debugging and comparing different types of manipulations. Moreover, the plot from each fit against the data was saved as a *.jpg, as well as figures that compared the fit results and the goodness-of-fit (GOF) statistics.
4) Optimizing hardware usage. There is inherent computational burden in the data processing (especially with 3D data), and the design should consider how to minimize this by utilizing multi-threading in the computer, processing data on multiple computers and/or a mainframe, and minimizing the number of large variables in the workspace.
5) Write own routines when possible. Matlab contains several robust built-in functions that can perform a plethora of calculations and computations based on some input options. Simplifying these robust functions into functions that

perform a single task (using a subset of the original Matlab source code) improved computational efficiency.

While each of the above basic principles were necessary for more accurate and efficient data handling, an emphasis was also given to automation and user-friendliness. During programming of the algorithm, it was believed that the more user-friendly an algorithm is, the less input the user needs to provide, and thus the full automation of the algorithm has been the ultimate goal. The present confocal algorithm is fully automated; the OCT algorithm, with its extra data reading sub-steps, is nearly fully automated.

5.2.A. Data processing tasks, steps, and design

OCT data processing steps from the raw data files to the analyzed results can be subdivided into 3 sequential tasks: pre-processing, fitting, and analysis (Sections 5.3-5, Fig. 5.1). Each of these tasks can be further subdivided into individual steps and sub-steps. In some cases, the order of the individual steps is important, while in others it is not. For example, there are 4 pre-processing steps needed: stitching, calibration, alignment, and ROI segmentation. Theoretically, the stitching, calibration, and alignment steps can be carried out in any order. However, the stitch-calibrate-align order was found to be advantageous since it reduced the size of variables in the workspace, which freed up memory and sped up computation.

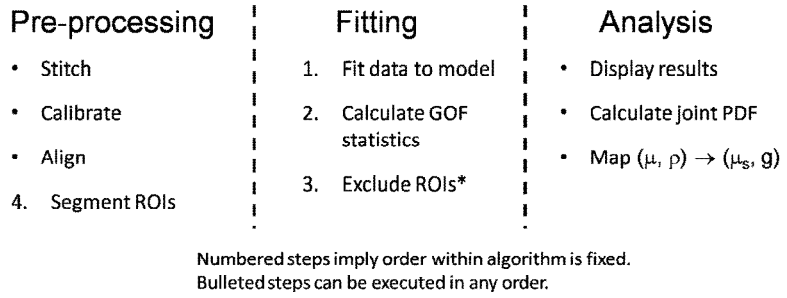

Fig. 5.1: Organization of data processing tasks, with individual steps categorized as pre-processing, fitting, or analysis. The numbered steps indicate their required order within a given task, while bulleted steps indicate no need for order within the given task. *- ROI exclusion is done both before and after fitting in the 3D algorithm.

After the pre-processing steps, the data is subdivided into ROIs, the data from each ROI is fit to the μ-ρ model. For each fit, goodness-of-fit (GOF) statistics are calculated, and the output is saved into a results file. After the fit results are determined and stored in a file, one important step in the analysis task is to read the results file from several data sets, and plot them together on a μ-ρ grid for comparison. Another key analytical step maps the fitted (μ, ρ) pair back to the optical properties (μ_s, g). Finally, to analyze the variance in the distributions of fitted μ and ρ values, a joint probability density function (PDF) is calculated for each group of samples.

5.3. Pre-processing steps in 2D: From the raw data to the averaged A-scans

In this section, the preparatory subroutines needed to process 2D OCT data are detailed. Each of these subroutines is part of a pre-processing algorithm that was organized in modular steps, so that one could keep track of the data as it propagated through the algorithm. In a single imaging session, multiple samples (either agarose gels with spheres or collagen gels) are imaged. Each sample is imaged at 5 randomly selected sites. At each imaging site, 10-12 images are acquired, with the sample manually shifted by 50 μm towards the objective between each acquired image. The 10-12 images are called an image set or a data set, all referring to images from a single site.

A graphical representation of the pre-processing algorithm is shown in Fig. 5.2. Typically, the first step is to read the raw data and form a 2D quasi-focus-tracked OCT image. In contrast to confocal microscopy, in OCT two additional sub-steps are needed: performing the Hilbert transform on each A-scan, and stitching together data acquired with the focal plane at different depths. When the 10-12 images at a single site are stitched together, they form 5 xz quasi-focus-tracked images per sample (Section 5.3.A). Another necessary step is to convert the signal from arbitrary units to units of reflectivity, which is done by calibrating the data against the signal from a known reflectivity, such as that from an oil-glass interface ($\rho = 4.05\times10^{-4}$) or the reflectivity from a phantom with known optical properties. Tissue samples and constructs generally have an irregularly

shaped surface, and thus the optical depth the light has traversed at a given z pixel varies along the lateral direction. To correct for this irregular shape, an alignment step which axially shifts individual A-scans so that the sample interface is at the same z pixel is also needed. These 5 stitched, calibrated, and aligned, images are then subdivided into ROIs, resulting in 5 curves per image set, or 25 curves per sample.

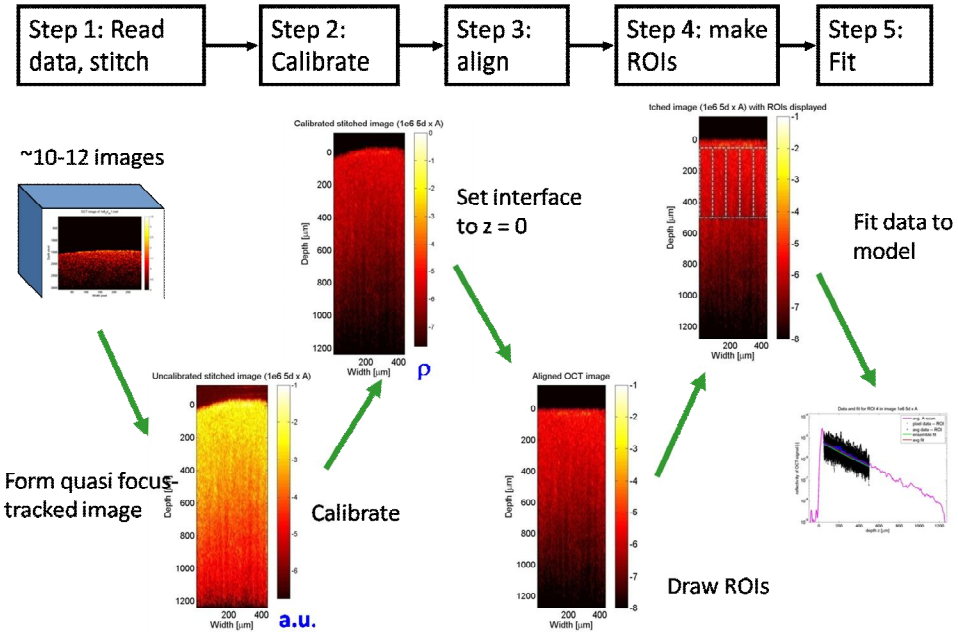

Fig. 5.2: The pre-processing algorithm for 2D OCT data, with a bird's eye view (top) and a pictorial representation (bottom). The key steps include stitching, calibration, alignment, and ROI segmentation, described in Sections 5.3.A-D, respectively. Thereafter, the data is fit and analyzed (Sections 5.4-5, respectively).

5.3.A Reading data, stitching, and shifting

The first step in creating a quasi-focus-tracked image is to read each of the 10-12 raw data files (all taken at the same site) into Matlab. The data is then digitally bandpass filtered using a narrower bandpass around the OCT carrier (fringe) frequency, with the central frequency (`cent`) and bandwidth (`ww`) determined from the averaged Fourier Transform of multiple A-scans in an oil-glass image acquired during the same imaging session. The OCT signal is then filtered in the frequency domain, and inverse Fourier Transformed back to the time domain. The envelope of the interferometric signal is

calculated digitally using the Hilbert transform. Since the envelope is proportional to the electric field, squaring the envelope results in the intensity.

```
filter1D = [exp(-2 * (((1 : samples / 2)' - cent) / ww) .^ 2); ...
    exp(-2 * (((samples / 2 : -1 : 1)' - cent) / ww) .^ 2)];
filter2D = filter1D * ones(1, lines);

% Filter data, convert to intensity
FV = fft(data);
FVte = FV .* filter2D;
Vtest = real(ifft(FVte));
E0 = abs(hilbert(Vtest));
dat4im = E0 .* E0;
```

After the intensity image is computed from each of the 10-12 raw data files in a single image set, the next step is to stitch the segments from each image that are in focus together, to achieve quasi-focus-tracking conditions. Here, `ps` is the pixel separation representing 50 μm, `nim` is the number of images in the data set, `imset` is a 3D matrix with each of the image files in that image set (the 3rd dimension is the objective lens position), and `combo_im` is the stitched image. Each of the images in the set is axially shifted by `ps` pixels. The xz pixel in focus will have the maximum signal along the 3rd (objective lens position) dimension.

```
ims2 = zeros(size(imset, 1) + round(ps*(nim - 1)) - 10, size(imset, 2),
nim);

for i = 1 : nim
    ims2(1 + round(ps * (i - 1)) : size(imset, 1) + ...
        round(ps * (i - 1)) - 10, :, i) = imset(1 : end - 10, :, i);
end
combo_im = max(ims2, [], 3);
```

5.3.B. Calibrating to oil-glass interface

The next step is to convert the signal from arbitrary detector units to dimensionless units of reflectivity. There are 2 ways to calibrate an image – either against a surface of known reflectivity such as a mineral oil-glass interface, or against the reflectivity fit to OCT data from a phantom with well-defined optical properties. It is worth noting that in theory, the oil-glass calibration should be simple and reproducible: acquire an image in which the oil-glass interface is in focus, identify the interface, and calculate the calibrating factor based on the Fresnel reflection formula. However, this "simple" measurement turned out to yield results that were not reproducible, particularly during 3D imaging. Thus while in the 2D algorithm, the oil-glass approach was sufficient, for 3D data processing, the phantom calibration approach was needed (Section 5.6.B). This section will focus on oil-glass calibration.

On the surface, this step is rather simple. A calibration image is displayed, the user identifies the interface, the signal is averaged laterally across the image and from this mean value the calibration factor is calculated using the Fresnel formula:

$$\rho_{oil-glass} = \left(\frac{n_{glass} - n_{oil}}{n_{glass} + n_{oil}} \right)^2 . \qquad (5.1)$$

Since the refractive indices of oil and glass at 1310 nm are 1.46 and 1.52 respectively, $\rho_{oil\text{-}glass} = 4.05 \times 10^{-4}$. Implementing the oil-glass calibration subroutine is quite straightforward – the oil-glass image is loaded and displayed, the user zooms in on the region that contains the interface, and the maximum signal is calculated. After faulty A-scans that are blank where the interface should be are removed, the signal is averaged resulting in a mean oil-glass signal $R_{oil\text{-}glass}$. Since the signal is proportional to the reflectivity in both the sample and the oil-glass interface, the reflectivity of the sample ρ_{sample} is determined by $R_{sample}*(\rho_{oil\text{-}glass}/R_{oil\text{-}glass})$.

It is worth noting that the calibration factor ($\rho_{oil\text{-}glass}/R_{oil\text{-}glass}$) is identical for all the images acquired in that imaging session. Since the user input required for the calibration is redundant, repeating this step for every image in that imaging session becomes

unnecessary. One way to avoid repeating this step is to save the factor ($\rho_{oil\text{-}glass}/R_{oil\text{-}glass}$) in a small file called `'auto_calib.mat'` in the relevant directory, so that if this file exists, it can be read without user input. If the file `'auto_calib.mat'` does not exist, the calibration subroutine is called.

5.3.C. xz frame alignment

The μ-ρ model, the underlying theory behind the method of measuring optical properties from OCT and confocal images, assumes that the sample is perpendicular to the optical axis. However, biological samples often have irregularly shaped surfaces that vary laterally across the image. Hence, it is necessary to flatten the image so that the light would experience the same attenuation at the same depth (z) pixel at different lateral positions in the image.

The basic algorithm for alignment of an xz frame assumes that there are 2 types of interface to a sample – a flat surface and an irregular surface. When the objective lens has a sufficiently high NA (0.18 in our case), a flat surface actually maps to a parabolic interface in the OCT image as a result of large scan angles. If the pixels that represent the start of the sample at each A-scan are also the ones with the maximum signal in that A-scan (this is common when there is a specular reflection), the image could be aligned automatically. However, when there are irregularly shaped surfaces, the user must provide some input for alignment. Thus, for a single xz frame, one can devise a simple algorithm using an `if/else` statement, in which the user would see the image and the maximum signal at each A-scan and choose the appropriate alignment method. Here, the variable `fr` represents the data from a single OCT frame, and `mi_` represents the z pixel at which the sample starts.

```
[mx, mix] = max(fr, [], 1);
mix = medfilt1(mix, 5);

%%    Plot image
```

```
%%    Prompt user about aligning image automatically or manually

if strcmp(button, 'Auto')
    align_coeff = polyfit(1 : length(mix), mix, 2);
    mi_ = round(polyval(align_coeff, 1 : length(mix)));
else
%%    Call snake alignment program
    mi_ = snake_align;
end
```

For the moment, let us assume the user chose an irregularly shaped sample that needs to be aligned manually. This can be done by clicking with the mouse on landmarks on the sample surface, or drawing a "snake" across the top of the sample. The algorithm devised for this task was modeled on a program originally written by Thomas M. Jørgensen of Risø National Laboratory, Denmark. After displaying the image, the command ginput is called, allowing the user to click as many times as needed.

```
[x_cl, z_cl, snake_button] = ginput; % clicked x, z, and button (1 ->
left, 3 -> right)
```

The user clicks on the surface landmarks, from left to right, using the main (left) mouse button. If the user makes a mistake, a right click will remove the incorrect click, by 'tagging' all the right clicks and the clicks that preceded them on the `snake_button` vector output from the ginput command. Thereafter, these clicks are removed in the `x_cl` and `z_cl` vectors.

```
% Tag right clicks and previous clicks
for j = 1 : length(x_cl)
    if snake_button(j) ~= 1
        snake_button(j - 1 : j) = snake_button(j - 1 : j) + 1;
    end
end

% Remove tagged clicks
```

```
for j = length(x_cl) : -1 : 1
    if snake_button(j)~= 1
        x_cl(j) = [];
        z_cl(j) = [];
    end
end
```

It is worth pointing out that the basic `ginput` → tagging right clicks and preceding clicks → removing tagged clicks subroutine described above was used in other applications throughout the thesis, such as when delineating a gel in a histology or confocal mosaic image. In terms of aligning OCT images, once the tagged clicks are removed, the "snake" is sorted (along x) and linearly interpolated across the image for all x pixels. The critical variable is `mi_`, which represents the z pixel at which the sample starts along every x position in the image.

```
% Adjust snake
m_cl = [x_cl, z_cl];
m_cl = sortrows(m_cl);
m_ext = [0, m_cl(1, 2); m_cl; x_max, m_cl(end, 2)]; % extend snake
across img
mi_ = round(interp1(m_ext(:, 1), m_ext(:, 2), 1 : x_max));
```

It is worth noting that during automated alignment, the variable `mi_` is determined as the pixel with maximum signal at each A-scan, thereby skipping the snake algorithm. Using the `mi_` variable, the new size of the aligned frame (along z) is calculated. Of note, the aligned image is padded with 1×10^{-11} instead of zeros to avoid log(0). Finally, all the A-scans in `fr` are shifted axially in the aligned frame variable `fr_align`, which is then ready to be subdivided into ROIs.

```
av = mi_ - min(mi_) + 1;
aw = max(av) - min(av) + 1;
fr_align = zeros(size(fr) + [aw, 0]) + 1e-11;
for i = 1 : size(fr, 2)
```

```
    fr_align((aw - av(i) + 1 : aw - av(i) + size(fr, 1))', i) = fr(:,
i) ;
end
```

5.3.D. ROI segmentation

As with alignment, there are 2 methods to delineate ROIs in an xz frame – automatically or manually. Automatic ROI delineation involves prompting the user for a start and end depths (μm), then calculating the appropriate z pixels. To determine the x pixels, the sample is divided into 5 equal lateral regions. Often, the first 50 μm of pixels are ignored, as this part of the signal is often corrupted by cross-talk from the specular reflection. The final depth is usually 500 μm, though the user could modify that when prompted to choose between manual and automatic ROI delineation. If the user chooses to delineate the sample manually, the image is displayed and the user is asked to zoom in on the ROI, and the corresponding pixels are determined accordingly. Putting this together, we have:

```
%% Prompt user about delineating ROIs automatically or manually

if strcmp(button, 'Manu')              % Manually drawn ROIs

    %% Display image
    i = 1;

    while i <= n_rois

        % zoom into ROI
        zoom on
        msg = msgbox('zoom into correct data range');
        waitfor(msg)
        zpix(i, 1 : 2) = round(get(gca, 'YLim'));
        xpix(i, 1 : 2) = round(get(gca, 'XLim'));
        zoom out
```

```
        %% Highlight ROI, prompt for user approval
    end
else                            % AUTO-ROIs
    %% Determine ROI boundaries automatically
end
```

The output of this subroutine were two 5x2 matrices `zpix` and `xpix`, which gave the axial and lateral start and end pixels for each ROI. Using these pixels, the ROIs were averaged laterally, resulting in 5 depth-dependent curves that would be fit to the theoretical model. The fitting routine and its outputs are described in the following section. Of note, when analyzing biological samples, it was determined that 5 ROIs is the optimal number, and that a larger number of ROIs signifcantly increases the inter-ROI variability for μ and ρ.

5.4. Fitting

In many respects, the fitting is the most important step in the data processing. This section details how the data from each ROI is fit to the μ-ρ model in a computationally efficient manner, and presents some preliminary analyses of the fit results.

5.4.A. The fitting equation

The general form of the μ-ρ model is

$$I = \rho \exp(-\mu z) + B \qquad (5.2)$$

Here, the B term represents the diffuse light component in the system. However, the B term matters in confocal signals, but not OCT signals, since the coherence gating in OCT drops the noise floor by a factor of 1000. The noise floor of the OCT system, defined in units of reflectivity, is ~10^{-10}. By comparison, at 500 μm (the deepest focal position), a sample with μ_s = 100 cm^{-1} and g ≈ 0 only decays to 2.27×10^{-8}, roughly 200× the noise

floor. Thus, the background term can be approximated to 0. Taking the natural log of the remaining terms linearize the μ-ρ model to

$$\ln(I) = -\mu z + \ln(\rho). \tag{5.3}$$

Now, the model is of the form y = mx + b, with μ = -m and ρ = exp(b). This form of the model is advantageous in that it can be solved directly, i.e., the fitting is not an iterative process that only approximates a solution and can be both computationally burdensome with no guarantee of convergence. Moreover, linear fits are easier to conceptualize and test when adding features such as weights and robustness.

5.4.B. Implementing the fitting into an algorithm

The subroutine works by sweeping through each ROI as part of a `for` loop. In each ROI, the appropriate pixels are segmented out into different variables. Most groups [25, 30, 31, 78, 79] average the data laterally and fits the averaged A-scan to their respective theoretical model. Our group also fits the data as an entire ensemble to the model. In general, the ensemble fit provides a better estimate of how the entire data agrees with the results, it has poorer GOF statistics than the averaged fit. However, the average data fit and the ensemble data fit are done primarily to check on one another. Both tend to yield approximately the same results, though the fitted ρ values from the ensemble fits are slightly less than those from the corresponding averaged fits. Any substantial difference indicates there is something wrong with the data, such as a geometrical problem or a structural heterogeneity.

Implementation-wise, after the appropriate vectors are created, a weighted linear least squared approach is used to fit the calibrated, depth-dependent OCT data to the μ-ρ model. The weights of the each depth are inversely proportional to the (lateral) variance of ROI pixels at that depth.

```
for j = 1 : n_rois
z_roi = zpix(j, :);
```

```
x_roi = xpix(j, :);

% average data fit
zi = z(z_roi(1) : z_roi(2))' * 1e-4;      % convert micron to cm
aas4fit = mean(fr_align(z_roi(1) : z_roi(2), x_roi(1) : x_roi(2)), 2);
aas_w = 1 ./(var(log(fr_align(z_roi(1):z_roi(2), x_roi(1):x_roi(2))),
0, 2));
[p, ci, civ, gof] = weighted_polyfit(zdata, log(aas4fit), aas_w, 1);

%% repeat fit for ensemble of data

%% store fit results in appropriate variables

%% plot results, save data

end
```

5.4.C. Weighted polynomial fitting

The function used to fit the data, `weighted_polyfit`, was compiled by the author for use in this algorithm. This function was modeled after the Matlab functions `polyfit`, which is an unweighted polynomial fitting function that comes with the basic Matlab package. To add weights to the pixels, certain subroutines were borrowed from the `fit` function from the Curve Fitting Toolbox, which is a robust but rather complicated fitting function for iteratively fitting many types of functions using multiple algorithms. One reason the `weighted_polyfit` function was written was to be able to perform weighted least squares fitting without the Curve Fitting Toolbox, since the toolbox is not always accessible and all the needed functions already come with the Matlab basic package. Moreover, the implementation was rather straightforward.

In the `weighted_polyfit` function, 4 inputs are needed: an `x` vector, a `y` vector, a weight vector `w`, and the polynomial degree `n`. The main output is vector `p`, which contains the (n+1) polynomial coefficients; additional (optional) outputs are the 95% confidence intervals, prediction bounds, and a vector containing GOF statistics. Note

that the `x`, `y`, and `w` vectors all need to be column vectors of the same length. A polynomial fit function that weights the individual (x, y) pairs contains 5 basic steps. First, the Vandermonde matrix `A` is computed [82]. Next, the Vandermonde matrix `A` is used to calculate the weighted Jacobian matrix `J`. Additionally, a weighted vector of `y` values (`Dy`) is determined. The Vandermode matrix is decomposed by QR factorization (orthogonal-triangular decomposition) [83], and the coefficients of polynomial `p` are solved for using `R`, `Q`, and `Dy`.

```
function [p] = weighted_polyfit(x, y, w, n)

A(:, n+1) = ones(length(x), 1);
for j = n : -1 : 1
    A(:, j) = x .* A(:, j + 1);
end

J = repmat(sqrt(w), 1, size(A, 2)) .* A;     % weighted jacobian for
lin reg
Dy = sqrt(w) .* y;

% solve equation by QR factorization
[Q,R] = qr(J,0);
p = full(R \ (Q' * Dy));    % Same as p = D*A\(D*y);
```

5.4.D. Plots and GOF statistics

The outputs from the `weighted_polyfit` function at each iteration of the `for` loop are all stored for further analysis in a '`SAMPLEname--RESULTS.mat`' file. Specifically, these are the fitted parameters μ and ρ, their 95% confidence intervals, the 95% prediction bounds over depth z, the arithmetic and geometric mean pixel errors, and the adjusted R^2. Fits in which the difference between the upper and lower 95% confidence interval were larger than the fitted value were considered poor fits and excluded. However, only a small fraction of the total fits actually failed to meet these criteria. Additionally, for both ensemble and averaged fits, there was a unique image

saved comparing the fitted data to the signal. There was also a plot that plotted the 2 against one another (Fig. 5.3A), a histogram of the 5 μ and ρ values the each ROI in the image set (Fig. 5.3B), and a histogram of the GOF statistics from each ROI in the image set (Fig. 5.3C).

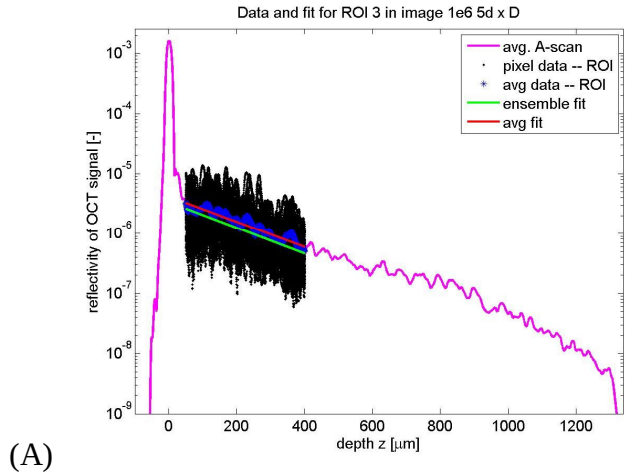

(A)

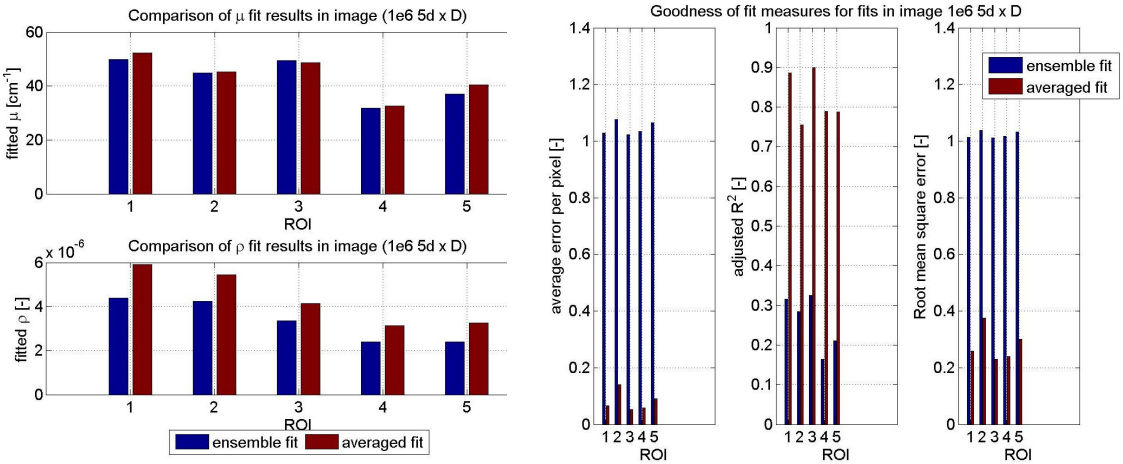

(B) (C)

Fig. 5.3: Sample output from a collagen gel. (A) Example of comparison of ensemble and averaged fits in a single ROI. Note that there were 5 ROIs per image set. (B) Example comparison of μ and ρ fit results for ensemble and averaged fits in 5 ROIs of image set. Though the ensemble and averaged fits produce very similar results, the ρ values from the ensemble fits are ~20% less than those from the averaged fits. (C) Example comparison of 3 GOF statistics: mean pixel error, adjusted R^2, and root mean square error, for 5 ROIs of an image set. Note that the GOF statistics of the averaged fits are better than those of the ensemble fits.

5.5. Visualizing and analyzing the fitting output

Finally, there are the critical steps of analyzing the fitted (μ, ρ) data. There are many types of analyses used over the course of this thesis; but 3 were chosen here as the most important. The first of these analyses involves displaying the data from different groups of the same experiment. Another important analysis involved characterizing the variance in the fitted (μ, ρ) data, which is done by calculating the joint PDF. Finally, there is mapping the fitted (μ, ρ) values back to (μ_s, g) space. Each of these analyses is analogous to a "step" described elsewhere in the chapter; however, there is no order or explicit interdependence between these analyses that the word "step" implies.

5.5.A. Reading and displaying the fit results

The most important analysis is to graphically compare the (μ, ρ) data from different groups – that is, to read the relevant results files and plot the data as a scatter plot on a grid that shows how theoretical (μ_s, g) values map to (μ, ρ) under the experimental conditions. Although this sounds trivial, consider a collagen gel experiment similar to the ones shown in Ch. 6-8, that compares cellular versus acellular gels at days 1 and 5. If there are 3 gels in each group and 5 sites per imaged gel, there would be a total of 60 results files to read. Thus, manually reading and plotting the data is not a viable option, and some automation is needed, which in turn brings about new challenges in terms of how to handle all the data.

Reading the fitting outputs efficiently requires standardizing the output and variable names. In general, it would be ideal if variables describing a group of samples would be named after them (i.e., `mu_acell_gels_1d`) as opposed to some general arbitrary name (i.e., `mu_sample1`), to allow for further analysis in the workspace that is often needed. But since in each experiment the names of the samples differ, naming variables requires manipulating the commands in such a way that produces variable names that differ between different experiments. This can be achieved by prompting the

user to name the various groups, storing the group names as strings inside a cell array, and then using the `eval` and `sprintf` commands in combination to create the appropriate commands (as shown below).

To simplify the algorithm, all the results files are to be placed in the same directory. Then, creating a cell array with the filenames of all the results files is trivial.

```
% Find result files in target directory
d = dir('*--RESULTS.mat');
reslist = cell(length(d), 1);
for i = 1 : length(d);          reslist{i, 1} = d(i).name;          end
```

Once all the results file in the directory are placed in a cell vector, the user can then choose the appropriate files in each group using the `listdlg` command integrated into a `for` loop. Note that the output of the `listdlg` command is a vector containing the indices of the highlighted choices (i.e., `[1, 3, 5]`). Each of these vectors is stored in the cell array `gind`.

```
for i = 1 : ngroups
    gind{i, 1} = listdlg('ListString', reslist, 'SelectionMode',
'multiple',        'PromptString', sprintf('Click on files in %s
group', ls{i}));
end
```

With the appropriate files chosen and stored into the cell vector `gind`, the results are read into the appropriate μ and ρ vectors, labeled to represent each group. The labels for each group are defined earlier in the program (not shown) in the parameter `group_base`.

```
for igr = 1 : ngroups

    eval(sprintf('mu_%s = [];', group_base{igr}));
    eval(sprintf('rho_%s = [];', group_base{igr}));
```

```
    for i = 1 : length(gind_)
        res_file = load(reslist{gind_(i)});
        eval(sprintf('mu_%s(end + 1 : end + length(res_file.muA), 1) =
res_file.muA;', group_base{igr}));
        eval(sprintf('rho_%s(end + 1 : end + length(res_file.rhoA), 1)
= res_file.rhoA;', group_base{igr}));
    end
end
```

Once the μ and ρ values from every sample of every group are read, they can be plotted on a log-log plot, along with a grid that maps theoretical (μ_s, g) values to the corresponding (μ, ρ) values for the respective imaging system (Ch. 2).

Recapping this algorithm, the files from each group of samples are identified, their results are read into vectors that contain all the μ and ρ values for that particular group, and these vectors are plotted on a log-log scale along with a grid.

5.5.B. Calculating the joint-PDF

Given the large volume of (μ, ρ) data that result from the fitting algorithm, some statistical methods are needed to simplify interpretation of the results. One simple way to do this is to calculate the joint PDF of μ and ρ values. The Matlab command `ksdensity` conveniently calculates the PDF from a distribution of values by binning the distribution into Gaussian shaped kernels. We assume that μ and ρ are statistically independent and calculate the joint PDF from the individual PDFs using the equation f(μ, ρ) = f(μ)f(ρ). Thus, a simple function can be used to calculate the joint PDF from a distribution of μ and ρ values on a log-log scale over predefined $\log_{10}(\mu)$ and $\log_{10}(\rho)$ vectors (`lmv` and `lrv`, respectively), and find the peak μ and ρ values from the 2 distributions.

```
% calculate pdfs
mu_pdf = ksdensity(log10(mu_dist), log10(lmv));
```

```
rho_pdf = ksdensity(log10(rho_dist), log10(lrv));

[RR uu] = meshgrid(rho_pdf, lmv);
[uu MM] = meshgrid(lrv, mu_pdf);

M_dist = RR.*MM;
mx = max(max(M_dist));
[I, J] = find(M_dist == mx);
mxrho = lrv(J);
mxmu = lmv(I);
rhomu = [mxrho, mxmu];
```

5.5.C. Mapping fitted (μ, ρ) data to (μ_s, g)

The final analysis is to map observations μ and ρ back to the optical properties μ_s and g. Since some of the (μ, ρ) data fall off the (μ_s, g) grid, such a mapping is typically done either on the mean (μ, ρ) values, or the peak (μ, ρ) from the joint PDF, in order to characterize a sample or a group of samples. The following subroutine presents a simple way to do such mappings.

As discussed in Ch. 2, for a given NA, the quotient b(g)/a(g), denoted b/a in short, is monotonically decreasing from $0 \leq g \leq 0.99$, resembling a double-exponential function (assuming absorption is negligible relative to scattering). Given this feature, one can use an interpolative approach to make the mapping. Specifically, for a (μ, ρ) pair, b/a can be calculated by:

```
boa_data = 2 * (G / Lf) * rho ./ mu;    % = b(g)/a(g), calculated from
model
```

Next, a theoretical b/a curve is determined for a vector of g values (gv). Knowing the theoretical and experimental (b/a) values, all that is needed is to interpolate for g, and use that g to solve for μ_s:

```
% Interpolate g, calculate corresponding a(g), and from that deduce mus
g = interp1(boa_theory, gv, boa_data);
afit = 1 - exp(-((1-g) .^ 0.6651) / 0.1555);  % a(g) for specific
interpolated g's
mus = mu ./ (2 * G * afit);
```

5.6. Translating algorithm from 2D to 3D

All measurements of optical properties assume the sample is homogeneously turbid over a certain volume, and thus some averaging is inevitable. When fitting optical properties from 2D OCT images, the volume that is averaged is shaped as a thin sheet; in our 2D system a typical ROI measures 90×10×450 μm (xyz). While such a cross-section of the sample may provide for an interesting image, it may not fully reflect the true local optical properties since it does not survey scatterers 20 μm away in the y direction. Intuitively, ROIs that included data from all 3 spatial dimensions would provide a better measure of the true local optical properties. However, while the second lateral dimension (along y) provides valuable information, it also adds some complications to the data pre-processing steps: stitching, calibrating, aligning, and segmenting ROIs. This section proposes solutions to address these challenges.

Unlike the 2D image processing algorithm (Fig. 5.3), which proceeds step-by-step, the 3D algorithm operates non-linearly (Fig. 5.4). Recall that the stitching, calibration, and alignment steps did not have to be carried out in a specific order. Once these 3 steps are completed, the data is subdivided into ROIs and the data is fit. Note that the fitting, GOF statistical calculation, and further data analyses all use the same methodologies as with the 2D OCT data. In 3D data processing, the calibration data – the reflectivity from a phantom made of polystyrene spheres embedded in agarose gels – is stitched and aligned separately from the remaining samples, and the data is fit to the model. The calibration factor is then calculated based on the theoretical reflectivity of the phantom, and is then used as an input for processing the remaining samples.

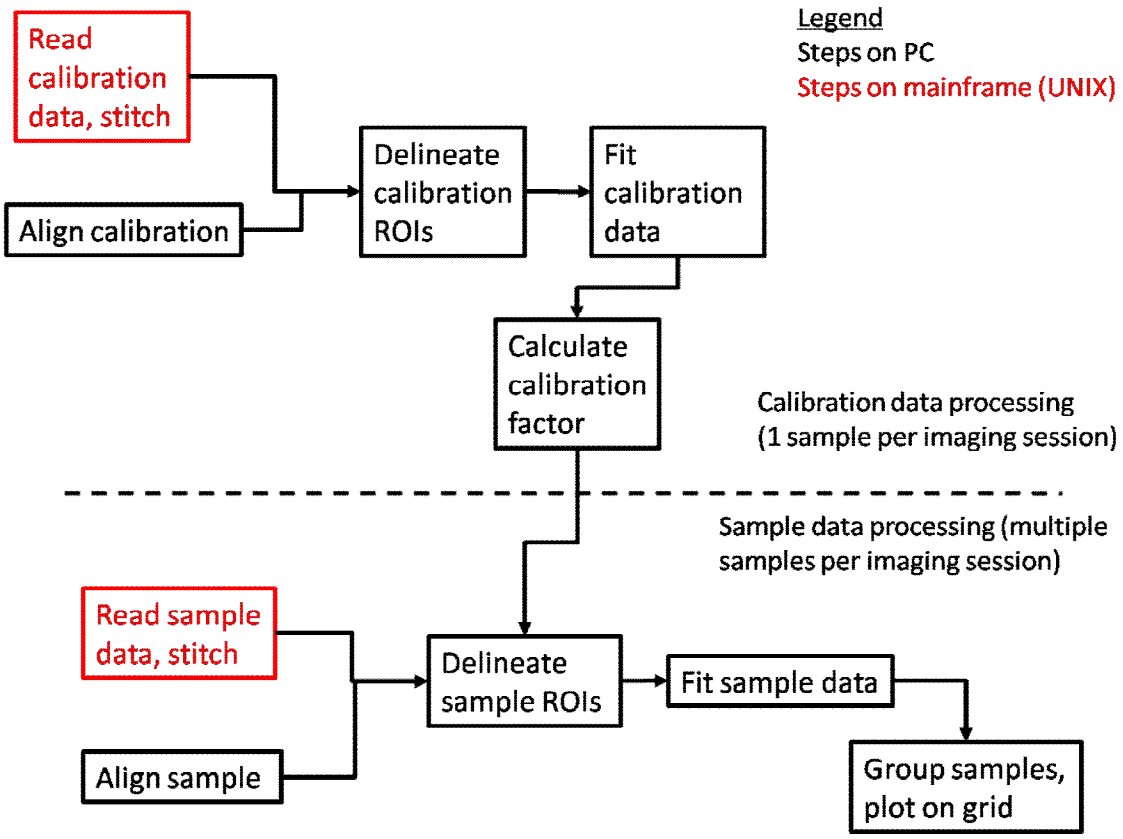

Fig. 5.4: Schematic of 3D algorithm. Steps in black are done on a PC, while steps in red are done on the mainframe computer using a UNIX version of Matlab.

5.6.A. Stitching and aligning in 3D

The first challenge arises from the large volume of accumulated data that results from 3D imaging (150 xz frames at 11 objective lens positions per imaged site = 3.07 GB, in contrast to ~20 MB for 2D imaging). This memory issue poses a challenge on multiple levels. First, there is the issue of storing the data on a server. Our lab solved this problem using a NAS (network attached storage device) with a RAID5 volume, which are better suited for computation and have fewer timeout errors than traditional Tera stations. Loading such large data files into Matlab also requires additional RAM (>4 GB), and both Matlab and Windows utilize RAM poorly. A fast, efficient processor is also required. Thus, the necessary computing power is beyond the specs available on state of the art computers running 64-bit Windows XP.

The optimal way to overcome this data problem is to separate the stitching program that forms a 3D dataset from the alignment step, which can be achieved by aligning only selected xz frames and interpolating. The stitching step is executed without any of the visualization on virtual machines (VMs) running in VMware Infrastructure Environment that use Linux OS. Connecting to these VMs from a PC requires using SSH protocol such as Putty or Cygwin. The VMs run the UNIX version of Matlab, and read and write to a NAS on which the OCT data is stored. Even with these efficient computing specifications, occasional timeouts occurred when processing four-dimensional 3 GB data sets (xyz at 11 objective lens positions), so the alignment was done on a frame-by frame basis. The resulting 3D matrix is ~200 MB.

It is worth noting that when running the data on a UNIX platform, in some versions the user-interface commands, path shortcuts, and even the Matlab Editor are sacrificed for speed. One way to circumvent such problems is to create a small script that adds the appropriate paths in the Matlab home directory. Moreover, the Matlab scripts can be edited (but not executed) through the Windows platform. Also noteworthy is that in the 3D imaging setup, in which the objective lens is moved instead than the sample, is advantageous since the pixels from different objective lens positions are aligned with respect to one another and no axial frame shifting was necessary.

Another challenge concerns aligning irregularly-shaped samples in 3D. This problem is more complicated than simply finding the sample-air interface, since maintaining proper hydration of biological sample often requires covering the sample in a medium like DMEM or PBS. Thus, the additional spatial complexity of many data sets in 3D made automated alignment nearly impossible. Since graphical input is required, running Matlab on the UNIX platform is not an option. Moreover, from a memory management perspective, Matlab runs slowly with a 200 MB, 3D matrix in the workspace. Thus, the fastest solution turned out to be repeating the 2D alignment step in 17 of 150 frames, and interpolating the missing points. Here the 17 individual frames, equally spaced along y, are read from the first objective lens position folder. Similar to the 2D algorithm, the user can choose between automated and manual alignment. The

interpolation is a 2D cubic interpolation, which is only ~2 sec slower than a linear interpolation. However, the output is not the aligned image, but rather a matrix `mi_`, which like in the 2D alignment case, contains the start z pixel at each (x, y) position. This matrix is used to align data only later on in order to minimize computational burden.

5.6.B. Calibration using polystyrene sphere phantoms

However, the major challenge in extending the algorithm to 3D turned out to be the calibration. Processing the sphere data separately introduced a complication: the large scan angles (relative to the NA of the objective lens) resulted in an intensity modulation, as there was more power in the central region (along the xy plane) than at the corners. It is worth pointing out that while this falloff existed in 2D, the reduction in signal was at most ~25 %; in the 3D imaging setup, the reduction was up to ~90 %. Given this unequal distribution of light, the calibration had to be ROI-specific. Moreover, any outlier fit in the sphere data meant that the corresponding ROIs from all the samples would also be faulty. Thus, an outlier rejection mechanism needed to be implemented as well.

As a result of these issues, the calibration data processing had its own arm in the schematic in Fig. 5.4, making the algorithm non-sequential. The stitching 3D calibration data, and 3D alignment matrix containing the pixels representing the start of the tissue, were combined when subdividing the data into ROIs and creating a z vector (similar to how normal sample data are processed, detailed below). The fit results from the uncalibrated data resulted in (μ, $\rho_{uncalib}$) data pairs. The user then ran a program that plots the uncalibrated data and allows for outlier exclusion by zooming in on the data range to use. The user inputs the size of the spheres in the phantom and the pre-calculated μ_s value, and the size of the sphere is used to do a Mie calculation [11] using the Mätzler program that performs this calculation in Matlab [84]. The Mie calculation output can be converted to a theoretical (μ_s, g) pair, which is then converted into (μ, ρ) space using the `getmurho_OCT_3D` subroutine. The calibration factor for each ROI is determined from the uncalibrated ρ matrix (`rhoM`).

```
theory = getmurho_OCT_3D(0.01, mus_theory, g_theory);
mu_ = theory(1);
rho_ = theory(2);
calib = rho_ ./ rhoM;
```

When laterally subdividing the data into ROIs, the uncalibrated signal from each individual ROI is multiplied by the corresponding element from the calibration matrix `calib`. Of note, in addition to processing all the sample data from the imaging session, the sphere data was calibrated and reprocessed using the results from the initial calibration fitting.

5.6.C. 3D ROI segmentation and ROI exclusion

The final step before fitting the data is segmenting out the ROIs. In contrast to the 2D ROI segmentation approach, in which the user could either automatically delineate (5) ROIs or manually select them, in 3D datasets, the stitched data is laterally subdivided into 10×10 regions (100 ROIs total). Initially, the 4 corners of the (10×10) matrix are excluded, since that is where the signal is weakest. For the remaining 96 ROIs, multiple exclusion rules are applied, removing ROIs that have a poor geometry or a poor fit. Typically, OCT data of agarose gel-polystyrene spheres phantoms maintain >90 ROIs/sample, while OCT data of collagen gels results in 30-80 ROIs/sample, depending (mostly) on the sample geometry. In comparison, the 2D data resulted in 35 ROIs/sample.

The 3D ROI preparation subroutine begins with the user inputing the start and end depth in μm, thereby defining the axial boundaries of the ROIs. Typical fits range from 150-400 μm, since in some collagen gels dehydration of the PBS affects the signal from the initial 100 μm of the sample. Before truncating in the axial direction, the signal from each ROI is then aligned using input from the `mi_` matrix, following the same subroutine used in the 2D case. The aligned 3D matrix of size `[X, Y, Z]` is then reshaped to be a

2D matrix of size `[X*Y, Z]`. The 2D matrix is averaged along the lateral dimension and transposed into a column vector.

At this stage, some exclusion rules are implemented. If the z=0 pixel of the ROI (found in the `mi_` matrix) falls within the first 70 pixels in more than 1/3 of the total A-scans in the ROI, the ROI is excluded. We chose 70 because there is a delay when the rotating reference arm galvo mirror changes scan direction (it rotates within ±5°), and this delay causes the axial pixel spacing to be nonlinear in the first (and last) 70 pixels of every other A-scan. Similarly, if the z = 400 μm pixel falls within the last 70 pixels in more than 1/3 of the total A-scans in the ROI, the ROI is also removed. There are also geometrical considerations. The μ-ρ model assumes that the sample surface is perpendicular to the optical axis but this condition does not always hold for ROIs from biological samples like collagen gels. Moreover, our experience with 2D fits suggests that the signals from samples that are tilted at a large angle relative to the normal, or contain a deep (>100 μm) crevice do not behave according to our model. To assess sample geometry, the distance between the highest and lowest z=0 pixel (in the ROI's `mi_` matrix) is calculated. If this distance is > 100 μm, the fit is excluded.

Following these exclusion rules, the fitting range is truncated axially based on the user inputs. Note that when fitting 3D OCT data, there are roughly 8.5× as many A-scans/ROI as when fitting 2D data. Consequently, fitting the data as an ensemble yields nearly identical fit results as fitting the averaged pixel value at each depth (or the median pixel value), and so only averaged fits are used. The averaged A-scan is then calibrated using input from the `calib` matrix, and fit to the μ-ρ model using the `weighted_polyfit` algorithm used for 2D fitting and (Section 5.4). At this stage, additional exclusion criteria are also applied. One post-fit exclusion rule has to do with the 95 % confidence intervals of the fit. Similar to the 2D case, fits in which the ration of the upper minus the lower confidence interval (in either μ or ρ) are excluded. Finally, fits resulting in "negative" attenuation values are also excluded (though most of these ROIs have already been excluded by the geometry criteria). Each of these reasons for ROI exclusion are also numbered and documented in an `ex_` matrix.

5.7. Conclusion and future steps

This chapter described the computational methods common to the remaining chapters in this thesis. The image-processing algorithms described here followed a standardized approach in which specific Matlab codes were developed for pre-processing, fitting, and analysis tasks followed the consistent nomenclature for files and variables. Each part of the algorithm was divided into modular steps and sub-steps, with documentation kept at each step such that the data could be monitored as it progressed through the algorithm. Separate algorithms were written for each OCT and confocal imaging system used in this thesis. This chapter covered many of the steps that were common to the different algorithms that processed data from the various imaging systems. Based on these experiences, the author concludes that the key to accurate, efficient, and consistent data processing is organization. Moreover, clearly identifying the steps that need to be done and where they reside within the context of the larger data processing objectives is vital to implementing them correctly.

Critical to data pre-processing were steps that stitched together a quasi-focus-tracked image from multiple images, calibrated the data against a sample of known reflectivity, aligned the sample so that the z=0 pixel was consistent laterally across the image, and segmented ROIs from the data. Implementation of these steps differed between 2D and 3D data processing. Fitting the data involved using a weighted polynomial fit and keeping track of GOF statistics to evaluate the fit. Analysis steps included displaying the (μ, ρ) data on a log-log plot that contained a grid of where theoretical (μ_s, g) pairs mapped to the experimental conditions, calculating the joint PDF of μ and ρ, mapping the data from (μ, ρ) space back to (μ_s, g) space.

Future steps will aim at fully automating the algorithm, such that the user only has to execute a single command and the data would process itself. A second priority is making the algorithm run faster. Currently, processing one sample in 3D takes ~20 minutes, and ideally this time could be cut down to 1 minute or less. Obviously, meeting

both the automation and speed objectives depends on improvements computing capabilities so that the stitching could be done on a PC rather than VMs. Additionally, improved algorithms for 3D alignment are also needed. These 2 areas are believed to be the bottlenecks overall. In this thesis, multi-tasking on multiple computers proved invaluable. Other improvements would be in terms of fitting routines such as bootstrapping. Overall, the author believes that this thesis made significant improvements in systematic data processing that would be needed in continuous monitoring of engineered tissues or when translating this technology into the clinic where it could assist in a variety of applications.

Chapter 6: Statistical characterization of the method of measuring optical properties from optical coherence tomography data

6.1. Introduction

The validation of any method to detect differences between groups of measured samples requires demonstrating that the method can reliably and accurately measure such differences, and that the measurements are reproducible. As this entire thesis revolves around the method of measuring optical properties from optical coherence tomography (OCT) data, it is necessary to establish the validity of the method through rigorous statistical analyses. This chapter presents a summary of various such statistical characterizations of the OCT algorithm.

The algorithm measuring optical properties from the OCT data represents a subset of steps that are part of data acquisition and analysis. Initially, the user images the sample at a specified site, acquiring multiple images of the sample with the objective lens successively shifted to enable forming a quasi-focus-tracked image. As outlined in Ch. 5, the specific tasks of the algorithm are to stitch the segments of the data that are in focus to form a 3D dataset, calibrate the data, align the data geometrically, subdivide the data into regions of interest (ROIs), average the signal in the lateral dimensions, and fit the

data to a theoretical model [8]. The algorithm fitted output – attenuation μ and reflectivity ρ – are observations that map back to the optical properties of the sample, namely, the scattering coefficient μ_s and anisotropy factor g [11]. Since μ and ρ are intermediate parameters that link experimental conditions to theory, they were chosen for analysis in this chapter.

The most important analysis of the algorithm is its accuracy – that is, how close are the measurements of μ and ρ to the theoretical predictions? This analysis was done on phantoms with well-defined optical properties. Additionally, there are 4 types of statistical analyses presented in this chapter that describe the reproducibility of the method: the intra-ROI, inter-ROI, inter-site, and inter-sample variabilities. These statistical analyses were done on both light polystyrene sphere scattering phantoms with uniform optical properties, and biological tissues, namely smooth muscle cells (SMCs) suspended in collagen I gels at 1 and 5 days. Both types of light scattering media were used in throughout this thesis. Testing the algorithm on phantoms was used to assess the accuracy and reliability of the method. In contrast, testing the algorithm on day 1 collagen gels (before matrix remodeling takes place) was used to assess the inherent variations of the sample preparation methodology, while testing the algorithm on day 5 gels was used to assess the variations that accompany gel development and remodeling.

The parameter reported in many of these analyses is the coefficient of variation c_v, which is defined as the ratio of the standard deviation to the mean. Since the analyzed algorithm makes 2 measurements (attenuation μ and reflectivity ρ), that are both assumed to be independently distributed random variables, the averaged c_v is reported for both parameters in percent, along with the standard deviation of the c_v values from n measurements. Note that the definition of a measurement changes for each type of statistical analysis, as detailed in Sections 6.3.A-E.

In this chapter, Section 6.2 provides details on preparation of both the phantoms and the collagen gels. Thereafter, Section 6.3 details each of the statistical analytical

methods. The results are shown in Section 6.4, and are summarized and discussed in Section 6.5.

6.2. Sample preparation

6.2.A. Sphere phantoms

To determine the accuracy and reproducibility of OCT-based optical property measurements, the measurement technique – both image acquisition and the image-processing algorithm – need to be validated on light scattering phantoms with well-defined optical properties. The objective here is to validate that measurements of both μ_s and g reliably match values predicted by theory. Varying g in phantoms is most easily achieved by changing the particle size in the phantom, and thus the optimal design of phantom for these validations is to suspend polystyrene spheres in agarose gels [85].

All the phantoms discussed in this chapter consist of differently sized polystyrene microspheres (Duke Scientific) suspended in agarose gel (Amresco). Specifically, 2 ml aliquots of 1-2 % agarose gel were prepared. Mie theory [11] was used to calculate the anisotropy and scattering cross-section of the spheres, from which the (sphere) stock solution volumes needed to arrive at the desired optical were determined. For each of the 2 ml aliquots, the agarose gel was melted prior to mixing in the predetermined sphere suspension, which created a "stock phantom". Prior to OCT imaging, a stock phantom was melted, and 100 μl of the sphere suspension were sandwiched between 2 glass cover slips inside of a washer. This 100 μl removed from the stock phantom and housed in the cover slip-washer unit represents 1 "sample" of a phantom.

The optical properties of the sphere phantoms statistically characterized in this chapter are summarized in Table 6.1. The optical properties of the phantoms ($20 < \mu_s < 60$ cm^{-1} and $0.45 < g < 0.92$) span ranges that are typical for tissues at NIR wavelengths. Note that phantoms A-E were imaged under 3D conditions with imaging taking place

over a 3 month period, while phantoms F-H and P-R were imaged under 2D conditions with imaging spanning 2 months.

Table 6.1: Optical properties of imaged phantoms. Accuracy measurements were made on phantoms C, D, E, F, and I. Intra-ROI measurements were made on phantoms A, B, C, and D. Inter-ROI and inter-site measurements were made on phantoms F, G, H, P, Q, and R. Inter-sample measurements were made on phantoms A, C, D, and E.

Phantom ID	Diam. [μm]	μ_s [cm^{-1}]	g [-]	f_{vol} [%]	N_{sph}/vol [ml^{-1}]
A	0.6	60	0.621	1.41	1.24×10^{11}
B	0.6	30	0.621	0.703	6.22×10^{10}
C	0.77	20	0.730	0.310	1.30×10^{10}
D	1.5	20	0.888	0.149	8.43×10^{8}
E	0.6	40	0.621	0.937	8.29×10^{10}
F	0.5	20	0.457	0.61	9.39×10^{10}
G	0.5	40	0.457	1.23	1.88×10^{11}
H	0.5	60	0.457	1.84	2.82×10^{11}
I	0.6	20	0.621	0.469	4.14×10^{10}
J	0.77	30	0.730	0.465	1.94×10^{10}
P	2	20	0.919	0.124	2.95×10^{8}
Q	2	40	0.919	0.247	5.90×10^{8}
R	2	60	0.919	0.371	8.85×10^{8}

6.2.B. Collimated transmission measurements

To assess the accuracy of the OCT algorithm, the results fitted from phantoms were compared to results obtained using a standard technique for measuring optical properties: spectrally resolved collimated transmission (CT) measurements. Both measurements we made on sphere phantoms only. The CT measurements were done as follows: First, a slab of phantom was prepared by sandwiching premade sphere/gel mixes (from the same stock solution as the phantoms measured by OCT) between two 60 x 25

mm cover slips, using additional cover slips as spacers. Light coming out of a fiber-coupled white light source (Ocean Optics) was collimated with a lens onto the phantom slab. Light that transmitted through the slab was collected by an additional fiber that was coupled to a spectrometer (Ocean Optics). Shutters before and after the phantom ensured only ballistic light was collected by the detection fiber.

The region of the spectra that had the highest signal-to-noise ratio (550-850 nm) was used in the analyses. Relative to the input irradiance I_{in}, the output irradiance I_{out} through a scattering medium of thickness L follows an exponential decay:

$$I_{out}(\lambda) = I_{in}(\lambda)\exp(-\mu_s(\lambda)L) \ , \qquad (6.1)$$

where μ_s, I_{in}, and I_{out} are all dependent on wavelength λ. Eq. 6.1 assumes that on average, less than one scattering event took place in the scattering medium, i.e., $\mu_s L \leq 1$, which requires preparing a thin sample. The CT was measured in 3 different phantom samples (slabs) with 5 measurement sites per sample. Note that fitting OCT data from thin samples would result in artifacts caused by the glass-gel interface, and thus the phantom slab was made from the same stock solution as the OCT-imaged phantoms, but they were not the exact same sample.

Since the wavelength-dependent refractive index mismatch was known *a priori*, Mie theory can be used to determine the wavelength-dependent scattering as a function of sphere size. Moreover, forward-based Mie calculations showed that over the examined wavelength range (550-1350 nm), the scattering spectra can be well approximated using a power law ($y = a \cdot x^b$). In order to solve the inverse problem, the resulting spectra were thus fit to a power regression, and the resulting coefficients were used to determine the sphere size and concentration, from which g and μ_s of the phantom slab at 1310 nm were determined.

6.2.C. Collagen gel measurements

In addition to statistically characterizing homogeneous scattering media with well-defined optical properties, a similar characterization was also applied to the main

biological tissue analyzed in this thesis, collagen gels. The objective here was to characterize how the spatial variations in the gels, together with the inherent statistical fluctuations in the OCT signal, affect the (μ, ρ) pair fitted from the signal. Moreover, the spatial variations in the gels could result either from variations during gel preparation and/or variations during gel development. Thus, to assess the statistical fluctuations that result from both gel preparation and development, optical property measurements were done at 2 timepoints: days 1 (preparation) and day 5 (development).

The protocol of collagen gel preparation has been described previously [76]. Briefly, 8 parts collagen solution (pH=2.5) were mixed with 1 part 0.2 M NaOH and 2 parts 5× culture medium. Immediately thereafter, 5 parts culture medium with the predetermined number of cells were added and aliquoted as 1 ml samples in 12-well plates. In all experiments, primary SMCs were used. The 1 ml aliquots thermally gelled at 37° C for 1 hr and then 1 ml of culture medium was added (for feeding). All gels were detached with a spatula after 24 hr. Gels that were imaged at day 5 were fed every 2 days. Note there were slight variations in the initial collagen and cell densities of the gels, specifically, the initial collagen density ($[\text{collagen}]_{t=0}$) of the gels was either 2 or 2.43 mg/ml, and the initial cell density ($[\text{cell}]_{t=0}$) was either 1×10^6, 3.8×10^5, or 2.1×10^6 cells/ml. The properties of the gels used in each analysis is detailed in Sections 6.3.A-E.

6.3. Statistical methods

This chapter consisted of 5 types of statistical analyses on accuracy and reproducibility. For clarity, these analyses are defined:

- Accuracy: represents the difference between the fitted (μ, ρ) coefficients and values predicted from theory, normalized by the theoretical predictions.
- Intra-ROI variability: represents the variability of the optical properties in a single ROI from a single site that was repeatedly imaged 10 times.
- Inter-ROI/intra-site variability: represents the variability of the optical properties from 5 ROIs from a single site.

- Inter-site/intra-sample variability: represents the variability of the mean optical properties from 5 sites on the same sample.
- Inter-sample variability: represents the variability of the mean optical properties from 3 different samples.

6.3.A. Accuracy of the algorithm

Calculating the accuracy of the optical property measurements is not trivial: in contrast to the other statistical analyses in this chapter, as the OCT measurements (i.e., the fitted μ-ρ data), cannot be directly compared to the spectrally-resolved CT measurements, which are the mean sphere size and density. Thus, both measurements need to be converted to optical properties μ_s and g, but while it is trivial to determine μ_s and g from a sphere size and density, the method required to do this for the OCT data is not straightforward.

First, there is the issue of calibration. While μ can be estimated using the measurement alone, ρ differs from μ, in that estimating ρ requires calibrating the OCT signal with an additional measurement on a phantom. Moreover, since data from sphere phantoms is used to calibrate the OCT signal for each individual ROI, an alternative calibration method is needed. The alternative method chosen was to define a single calibration factor per dataset. This calibration factor was determined from the entire dataset, while only a subset of the total ROIs (~2/3) was statistically analyzed. Specifically, the calibration factor was determined from the entire 100 ROIs, while only inner 64 ROIs (8×8 along x and y) were tested. Note that here n represents the total number of ROIs.

These OCT data from each phantom results in a distribution of (μ, ρ) values. From this distribution, the joint probability density function (PDF) for μ and ρ was calculated by binning the distribution into Gaussian-shaped bins. From the PDF, the (μ, ρ) pair that corresponds to the peak of the PDF are found. The corresponding (μ_s, g) of

the phantom are found by mapping the (μ, ρ) value of the peak back to (μ_s, g) space. Additionally, the contour in μ-ρ space where the PDF is half of its peak value was also determined and used to estimate the measurement error in (μ_s, g) space. These values described the full-width at half-maximum (FWHM) of the distributions of μ_s and g.

6.3.B. Intra-ROI variability

To calculate the intra-ROI variability, a site (xz frame) was repeatedly imaged 10 times. Fitting for attenuation μ and reflectivity ρ in each of these ROIs yields 10 data points per ROI, from which a coefficient of variation c_v can be calculated. Thus, the reported n value represents the total number of ROIs analyzed. Outlier ROIs in the distributions were removed if their (μ, ρ) values were >3 standard deviations from the mean. In these outlier ROIs, both μ and ρ measurements were faulty (as opposed to only 1 parameter).

The phantoms statistically analyzed here were A, B, C, and D. Additionally, day 1 and day 5 collagen gels ($[cell]_{t=0} = 1\times10^6$ cells/ml, $[collagen]_{t=0}$ = 2 mg/ml) were also imaged and analyzed. Note that the 10 xz frames acquired were part of a 3D dataset that had 10 y positions (instead of 150 frames used in typical 3D sets). Thus, the 2D OCT frames were spaced 30 μm apart.

6.3.C. Inter-ROI (intra-site) variability

To calculate the inter-ROI variability, c_v was calculated for both the μ and ρ values from all the ROIs in the image. Here, the reported n value represents the number of images analyzed. Both sphere phantoms (F, G, H, P, Q, and R) and collagen gels ($[cell]_{t=0} = 3.8\times10^5$, 1×10^6 , or 2.1×10^6 cells/ml, $[collagen]_{t=0}$ = 2.43 mg/ml) were imaged in this analysis.

6.3.D. Inter-site (intra-sample) variability

Calculating the inter-site/intra-sample variability was done in 2 steps. First, the mean μ and ρ values were calculated for a single site, and then c_v was calculated for either μ or ρ across different sites on the same sample. Note that implicit in these measurements is averaging over the imaged site. Here, the reported n value represents the number of samples analyzed. This analysis used the same sphere phantoms and collagen gels that were used to determine the inter-ROI variability.

6.3.E. Inter-sample variability

Similarly, calculating the inter-sample variability was done in 2 steps. First, the mean μ and ρ values were calculated across multiple sites in the same sample, and then the mean μ and ρ values were calculated across different samples (either phantoms or collagen gels) imaged. The various phantoms had identical optical properties, while the various collagen gels were of the same experimental condition (i.e., day 5). Note that implicit in these measurements is averaging, both within a single site, and over the multiple sites imaged in the same phantom/collagen gel. Here, the reported n value represents the number of groups of samples analyzed. The sphere phantoms used for this analysis were A, C, D, and E; the collagen gels were the same ones used for the inter-ROI and inter-site variability calculations ($[cell]_{t=0} = 3.8\times10^5$, 1×10^6 , or 2.1×10^6 cells/ml, $[collagen]_{t=0}$ = 2.43 mg/ml).

6.4. Results

6.4.A. Accuracy of the algorithm

To assess the accuracy of the method of measuring optical properties from OCT data, the optical properties μ_s and g of phantom stock solutions were determined using both OCT and spectrally-resolved CT measurements. The CT measurements were used to estimate a sphere size and density, from which μ_s and g were calculated. These (μ_s, g)

pairs were compared to (μ_s, g) pairs that corresponded to the (μ, ρ) values fit from OCT data, wherein the CT measurements were considered as "truth". Data from the 5 different phantom samples is plotted in Fig. 6.1, along with y = x line that signifies where OCT measurements are accurate.

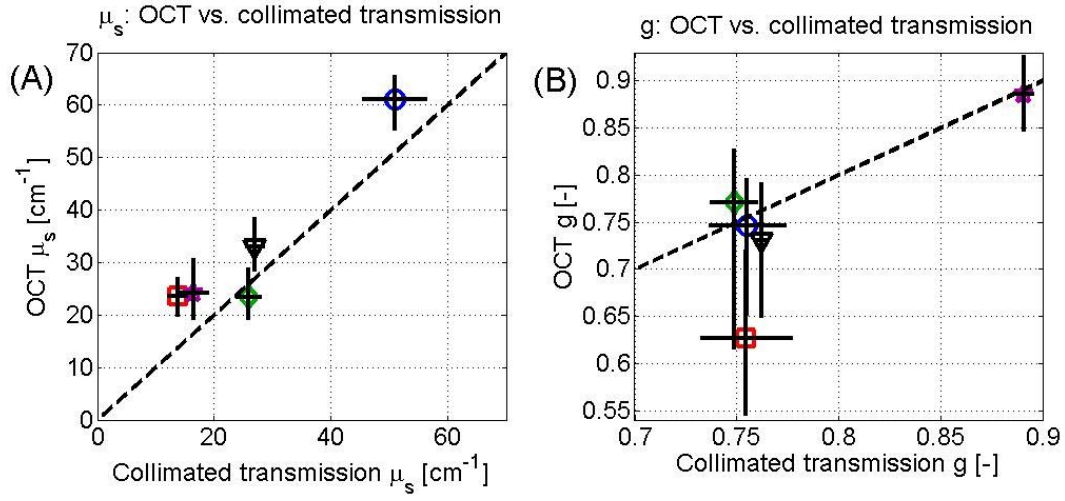

Fig. 6.1: Comparison of optical properties of sphere phantoms determined by both OCT and CT for μ_s (A) and g (B). The dashed line represents the y = x line, where the CT is considered "truth". Each marker represents a different sphere phantom. Error bars along the horizontal axis represent the standard deviations, while error bars in the vertical axis were calculated using the method specified in Section 6.3.A.

Fig. 6.1A shows that the OCT algorithm overestimated scattering coefficient μ_s by 20 % in 4 of 5 phantoms. Moreover, the variations in estimating μ_s using OCT were approximately 22 % in all phantoms, nearly double the variations obtained using CT measurements (12 %). However, the vertical and horizontal error bars represent different number, with the CT measurement error being the standard deviation, while the error in the OCT measurements representing the FWHM of the distribution of μ_s and g values. With regards to anisotropy g, the OCT measurements underestimated the CT-predicted values by 4 %. Here, approximately 10 % variation is seen in the OCT measurements, while the CT variation was <4 %. It is worth noting that in phantom F there was sphere aggregation, as evident by the higher μ_s and g values, which was identified by both techniques. Additionally, the largest discrepancy in g was observed in phantom I, where

the CT measurement disagreed with theory while the (self-calibrated) OCT measurement did not. The increased variation and error in phantom I may also be attributed to the fact that fitting algorithms frequently compensate for error in one parameter by varying another, which results in estimating both parameters erroneously.

The data shown in Fig. 6.1 demonstrates that the OCT method used in this thesis can measure μ_s and g via (μ and ρ) with sufficient accuracy. In comparing the 2 techniques, it is important to note that the OCT measurement analyzes nanoliter volumes, where fluctuations in sphere density are much more pronounced, while the CT measurement averages over microliter volumes which are much less susceptible to such variations. Moreover, the OCT measurements do not require preparation of a thin slab, making the technique much more applicable when imaging biological samples.

6.4.B. Intra-ROI measurements

The intra-ROI measurements for sphere phantoms, day 1 collagen gels, and day 5 collagen gels, are shown in Fig. 6.2A-C, respectively. Fig. 6.2A shows that for sphere phantoms, the intra-ROI variability for ρ was higher than μ in 2 of 4 phantoms, while in the other 2 phantoms the intra-ROI variability was comparable. Importantly, the average intra-ROI c_v was <10 % for both μ and ρ, suggesting that the measurements are indeed reproducible.

Unlike in the sphere phantoms, there was larger intra-ROI variation in the (μ, ρ) values fit from collagen gel data, as nearly all the c_v values for either μ or ρ were >10 %. The day 5 collagen gel data showed that the c_v values for both μ and ρ fluctuated around 10-30 %. Interestingly, the c_v values for ρ, at day 1 were consistently around 20 %, while the c_v values for μ in the day 1 gels varied from 18-55 %. However, images of the highly variable gel (day 1 gel A) reveal that this specific gel was not homogeneous, but instead had a stratified appearance (data not shown). Such a non-uniform sample geometry may account for the large fluctuations in μ observed in the data and suggest non-uniform sample preparation.

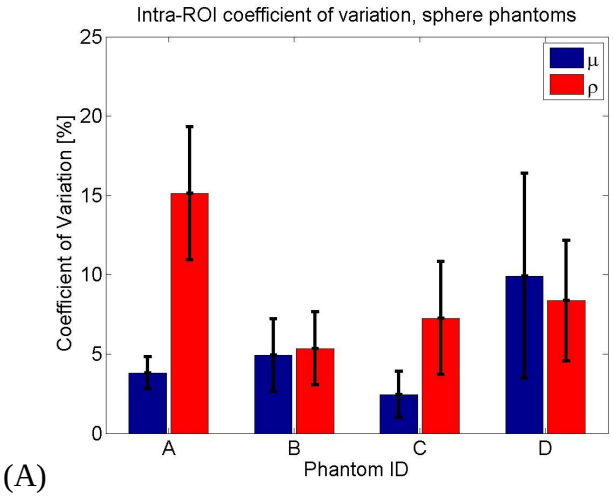

(A)

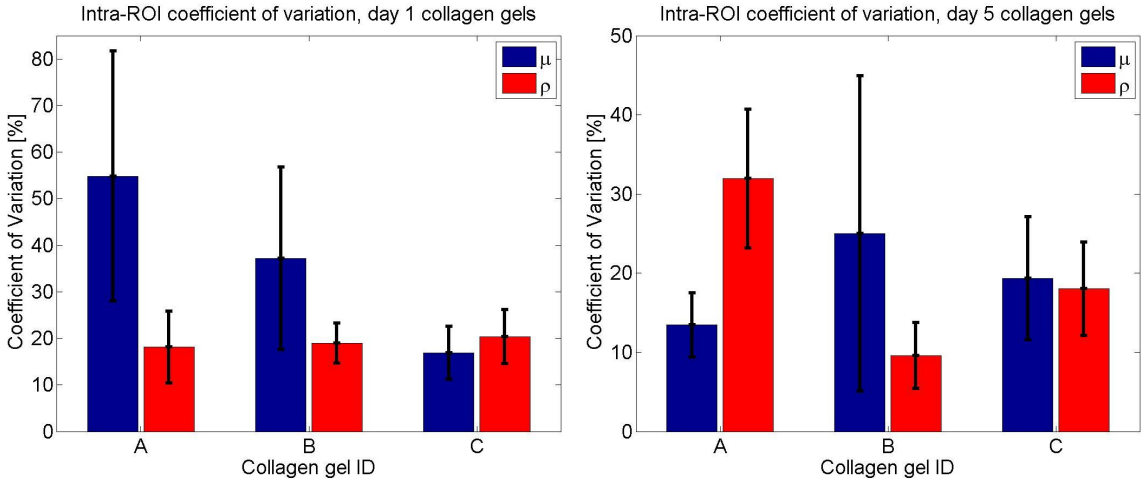

(B) (C)

Fig. 6.2: Intra-ROI coefficient of variation for both μ and ρ for sphere phantoms (A) and collagen gels at day 1 (B) and day 5 (C). Details on the optical properties are found in Table 6.1. The collagen gels in (B-C) had an initial cell density of 1×10^6 cells/ml and an initial collagen density of 2 mg/ml.

6.4.C. Inter-ROI measurements

Fig. 6.3A-C shows bar graphs of the statistical fluctuations in μ and ρ values between ROIs from a single imaging site for sphere phantoms, day 1 collagen gels, and day 5 collagen gels, respectively. In Fig. 6.3A, inter-ROI variations from 6 phantoms are shown; each phantom was imaged at 5 sites. In all 6 phantoms, it can be seen that there were larger variations in ρ than in μ. In comparing the phantom data to Fig. 6.2.A, the

slightly higher c_v values for both μ and ρ suggest that the optical properties did not vary much more within a single site (450×10×450 μm along xyz) than they did within a single ROI (90×10×450 μm).

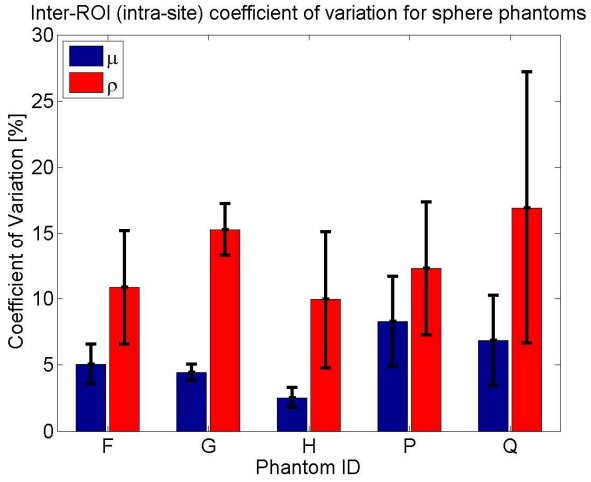

(A)

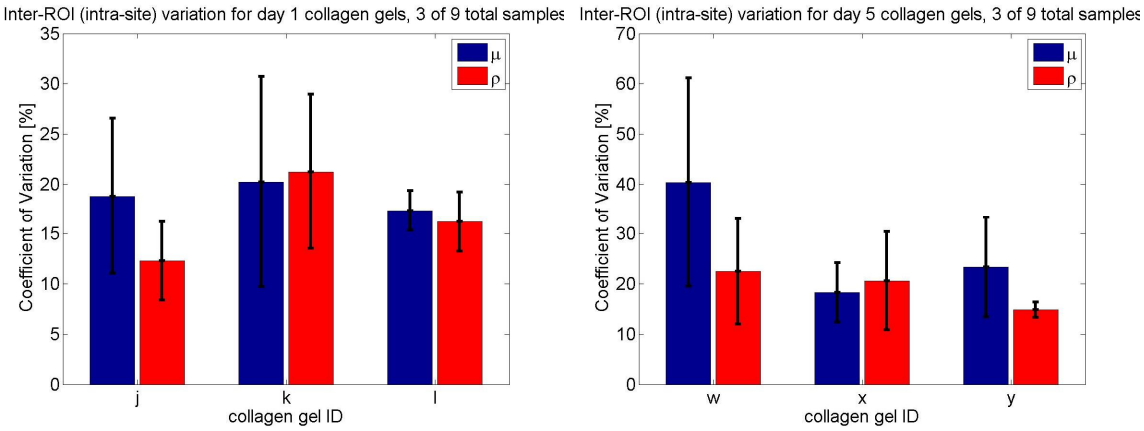

(B) (C)

Fig. 6.3: Plots of inter-ROI (intra-site) variability of attenuation μ and reflectivity ρ, expressed as the coefficient of variation in percent. c_v values for phantoms, day 1 collagen gels, and day 5 collagen gels are shown in (A-C), respectively. Details on the optical properties are found in Table 6.1. The collagen gels in (B-C) had an initial cell density of 1×10^6 cells/ml and an initial collagen density of 2.43 mg/ml; note that only 3 of 9 collagen gels are shown in for clarity.

Bar graphs in Fig. 6.3B-C show the μ and ρ coefficients of variation for 3 collagen gel samples selected from a total of 9 samples analyzed. The collagen gels

shown in Fig. 6.3B-C had an initial cell density of 1×10^6 cells/ml and an initial collagen density of 2.43 mg/ml. Numerical data that summarizes the c_v values from all 9 samples for both day 1 and day collagen gels is provided in Table 6.3 at the end of the chapter. Similar to the sphere phantoms in Fig. 6.3A, the number of sites in each sample was 5, and again, there was less variability in the sphere phantoms than in the collagen gels. Comparing the inter-ROI variability (Fig. 6.3B-C) to the intra-ROI variability in collagen gel data (Fig. 6.2B-C) reveals that there was a modest net increase in c_v for both μ and ρ. Overall, these data suggest that like in sphere phantoms, the optical properties of collagen gels did not vary much more within a single site ($450\times10\times450$ μm) than within a single ROI ($90\times10\times450$ μm).

6.4.D. Inter-site and inter-sample measurements

The inter-site and inter-sample coefficient of variation measurements of μ and ρ for sphere phantoms and collagen gels are shown in Fig. 6.4A-B, respectively. Because the number of "samples" (either individual phantoms/collagen gels, or groups of identical phantoms/collagen gels) analyzed decreased, the data was grouped into phantoms, day 1 gels, and day 5 gels. In terms of inter-site (intra-sample) variability, the c_v values for sphere phantoms was 4 % and 12 % for μ and ρ, respectively. Note that the c_v values here were lower than those in Figs. 6.2A and 6.3A. This is because there was averaging over an entire site in the inter-site calculation, which had the effect of lowering c_v. As for collagen gels, the coefficient of variation for both μ and ρ at day 1 and day 5 was about 30 %. For μ, this was a modest decrease from the inter-ROI measurements, while for ρ this was a modest increase from the inter-ROI data. Since in general these numbers were comparable to the inter-ROI measurements, the data suggest that the variation within a single (sub-milliliter) sample is comparable to (if perhaps slightly larger than) the variability within a single site ($450\times10\times450$ μm).

With regards to the inter-sample variations, the data (Fig. 6.4B) behaves largely as predicted. There was more variability in the optical properties in collagen gels than sphere phantoms, as one would expect more intrinsic variation in biological samples than

in nonliving materials. Comparing the inter-sample collagen gel data (Fig. 6.4B) with inter-site (intra-sample) data (Fig. 6.4A) shows that the variation between samples was larger than the variations within a single sample. Moreover, there was more inter-sample variability in day 5 gels than in day 1 gels, suggesting that in addition to the variations in preparation, the different gel samples also developed (remodeled) differently.

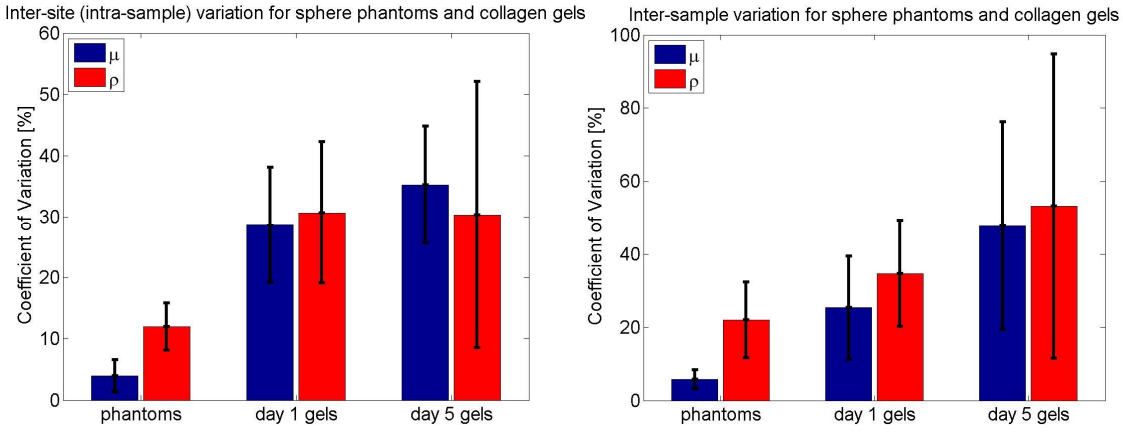

(A) (B)

Fig. 6.4: Plots of inter-site/intra-sample variability (A) and inter-sample variability (B), comparing sphere phantoms, day 1 collagen gels, and day 5 collagen gels. The phantoms used in the inter-site (intra-sample) analysis were F-H and P-R, while the phantoms used in the inter-sample analysis were A, C, D, and E (details provided in Table 6.1). The collagen gels in (B-C) had an initial cell density of 1×10^6 cells/ml and an initial collagen density of 2.43 mg/ml.

6.5. Summary and conclusion

This chapter involved the validation experiments to demonstrate the ability of the OCT algorithm to accurately and reliably measure the optical properties of scattering media. Specifically, the accuracy of the algorithm, as well as the intra-ROI, inter-ROI, inter-site, and inter-sample variabilities were statistically characterized. A concise summary of the all the chapter's results, for both sphere phantoms and collagen gels, is found in Tables 6.2 and 6.3, respectively.

Table 6.2: Reproducibility of the method in sphere phantoms, expressed as coefficients of variation. All data is expressed in percent as mean ± standard deviation. * - outliers that were over 3 standard deviations away from the mean (<4 % of data) were excluded.

Sample type	n	μ	ρ
Intra-ROI*	84	5.06 ± 4.24	9.05 ± 5.12
Inter-ROI	30	5.33 ± 2.71	13.32 ± 5.74
Inter-site	6	3.98 ± 2.61	11.99 ± 3.86
Inter-sample	4	5.81 ± 2.55	22.06 ± 10.33

Table 6.3: Reproducibility of the method in collagen gels. The intra-ROI, inter-ROI, inter-site, and inter-sample data show coefficients of variation, expressed in percent as mean ± standard deviation. * - outliers that were over 3 standard deviations away from the mean (<4 % of data) were excluded.

Sample type	Collagen gels, 1 d			Collagen gels, 5 d		
	n	μ	ρ	n	μ	ρ
Intra-ROI*	63	35.41 ± 24.26	19.13 ± 6.07	63	18.99 ± 12.78	19.85 ± 11.31
Inter-ROI	45	39.94 ± 24.82	30.61 ± 13.91	46	38.81 ± 25.40	23.39 ± 13.80
Inter-site	9	28.64 ± 9.48	30.69 ± 11.61	9	35.22 ± 9.58	30.33 ± 21.76
Inter-sample	3	25.40 ± 14.14	34.74 ± 14.50	3	47.87 ± 28.39	53.12 ± 41.60

The results shown in Figs. 6.1-4 and Tables 6.2 and 6.3 demonstrated that algorithm developed and used in this thesis was both accurate and reproducible. In general, Tables 6.2 and 6.3 illustrate that in all the variability measurements, the measured c_v values for both μ and ρ were always higher in collagen gels than in sphere phantoms.

In terms of accuracy, the algorithm slightly overestimated the fitted μ_s values by 22 %, while g was underestimated by 4 %. The error in fitting μ corresponds to half the error in estimating μ_s (11 %); the error in g results in an overestimation of ρ that ranges from 12 % for g = 0.3 to 46 % for g = 0.9. While these biases that overestimate the fitted

parameters appear systematic, it is important to note that the variations in both μ and ρ (and hence μ_s and g) that are encountered in tissues and collagen gels (Ch. 7-9) are on a logarithmic scale, which thereby diminishes the effects of the resulting errors.

In terms of reproducibility, the intra-ROI coefficient of variation was <10 % for both μ and ρ in sphere phantoms, demonstrating a high degree of reproducibility in a uniform scattering medium. Moreover, this data suggests that spatial averaging can adequately reduce speckle noise which varies between repeated measurements. In collagen gels, the measured intra-ROI c_v values were substantially higher, near 20 % for both μ and ρ in 5 of 6 gels. However, because of slightly different mountings, the collagen gel and sphere phantom measurements are different. The sphere phantom is compactly housed within a washer and cover slips, while the collagen gel is floating in a saline bath in a Petri dish. Evaporation of the saline over the hour moves the air-saline interface closer to the gel surface. This high signal from the air-saline interface corrupts the signal from the gels and adversely affects the fits; movement of this interface caused by evaporation will therefore introduce variability that is unrelated to the method. Of note, in normal data acquisition in which 150 xz frames are acquired, the deeper regions are acquired last, and thus the sample is mounted such that evaporation effects on the signal are minimal.

In terms of inter-ROI variability (Fig. 6.3), the measured c_v values for in both sphere phantoms and collagen gels were slightly higher than the corresponding intra-ROI variability c_v values (Fig. 6.2). Similarly, the inter-site variability was modestly lower than the inter-sample variability (Fig. 6.4) for sphere phantoms and collagen gels. Note that the inter-site c_v values (Fig. 6.4A) were slightly lower than the inter-ROI values (Fig. 6.3). However, in both the inter-site (and inter-sample measurements), there was spatial averaging of the fitted coefficients over the site (and sample). Considering the additional averaging in the inter-site and inter-sample measurements, it appears as if the variation in the measurements sequentially increased from intra-ROI to inter-ROI to inter-site to inter-sample.

When characterizing a measurement technique like the method of measuring optical properties from OCT data, some attention should be paid to a couple of other matters. First, with respect to both the phantoms and collagen gels, it is important to note that as much as these statistical analyses characterized the sample preparation protocol as much they characterized the algorithm output. Preparing a phantom with uniform particle spacing on the micro-scale is challenging; preparing a collagen gel that is uniform on the micro-scale is impossible. And while there were many notable differences between collagen gels of the same experimental condition, all collagen gels of the same condition were created at the same time with the same collagen and cell source. Thus, non-uniformities in sample preparation are dictated by the thermal gelling time of the collagen (~2-3 min) during which the gel suspensions need to be mixed and aliquoted.

Secondly, it is also important to note that in order to obtain accurate and statistically reliable results, image acquisition is as important a step as the data processing described in this chapter. In other words, a well characterized and statistically valid algorithm is useless without developing a reliable systematic imaging protocol. Thus, in order to repeat the experiments in this chapter, it is necessary to develop protocols for handling, mounting, and aligning the samples.

In conclusion, the method of measuring optical properties from OCT data was demonstrated to make reliable measurements, both in terms of accuracy and reproducibility. In a series of sphere phantoms that span a wide range of optical properties, the algorithm output was shown to overestimate theoretical predictions by 18 % in μ and 7.4 % in ρ (Fig. 6.1). The intra-ROI variability (Fig. 6.2) in sphere phantoms was less than 10 % for both μ and ρ, illustrating the method yields reproducible results. Measurements on collagen gels were had higher variability than measurements on sphere phantoms. Finally, the variability increased as the volume analyzed increased; however, averaging over a site or sample offset this increase in variability.

Chapter 7: Quantitative characterization of developing collagen gels using optical coherence tomography

This chapter was co-authored by: Monica T. Hinds, Niloy Choudhury, Noi T. Tran, Stephen R. Hanson, and Steven L. Jacques. A version of this chapter has been accepted for publication in the Journal of Biomedical Optics. Note the version here contains additional data on the relationship between cell density and optical properties in the appendix.

7.1. Introduction

The non-destructive characterization of engineered tissues has generated enormous interest recently. Frequently, tissue engineers are interested in monitoring the local microenvironment in an engineered tissue and assessing parameters such as cell number, cell function, protein expression, and mechanical properties. Most current techniques that characterize these parameters are either destructive, require adding (often expensive) labels to the sample, or making macroscopic measurements with no possibility of assessing local variations [3-6]. On the microscopic level, engineered tissue constructs often have local heterogeneities, and the patency of implanted constructs can depend on assessing these local variations.

In general, optical methods have shown great promise for non-destructively characterizing engineered tissues. One particularly promising method is optical coherence tomography (OCT). OCT offers several unique technological advantages for characterizing engineered tissues [22]. Commercial OCT systems can achieve an axial spatial resolution <10 μm and penetrate up to 1 mm in highly-scattering media, imaging at video rate speeds. As a fiber-based technology, OCT can be coupled into flexible handheld probes, allowing them to be easily incorporated into incubators.

Several recent studies have used OCT to characterize engineered tissues. Initially, Tan et al used OCT to visualize how fibroblasts change the architecture of a 3D chitosan scaffold [86], and then to monitor cell migration, proliferation, and detachment off a calcium phosphate scaffold by trypsinization [87]. Rey et al visualized chemotaxis-induced cell migration in 3D agarose substrates [88]. OCT has also been used to visualize how cells change the porosity in poly(l-lactic acid) scaffolds [89] and chitosan scaffolds [90].

These papers clearly demonstrate the ability of OCT to characterize features such as cells (or a cluster of cells) on a weakly scattering background of an imaged tissue construct. However, as the tissue construct develops, gel compaction, cell proliferation, and matrix remodeling change the size and density of scatterers in the sample. At this stage, the construct becomes a highly scattering medium, in which the cells can no longer be resolved. Properly characterizing mature tissue constructs just prior to implantation will be important for ensuring successful outcomes, but given the highly-scattering nature of mature constructs, making such assessments is quite challenging.

Moreover, the bulk of the work in characterizing engineered tissue constructs using OCT has been qualitative image analysis, based primarily on identifying features of interest (i.e., a cell) by a subjective operator. Given the qualitative nature of these methods, systematically surveying large volumes of data (~cm^3) imaged at micron resolution is both cumbersome and impractical. However, OCT data contain quantitative information on the optical scattering properties of the imaged sample. The optical

properties of interest here are the scattering coefficient μ_s [cm^{-1}] and anisotropy factor g [dimensionless], which provide a measure of the density and size of scattering particles in the medium, respectively [11]. With proper theoretical modeling it is possible to describe the depth-dependent OCT signal as a function of μ_s and g, as well as the system parameters [8]. By fitting a depth-dependent OCT signal that is representative of local nanoliter volumes in the sample to a theoretical model, it is possible to determine the local scattering properties of the sample. This approach was used to evaluate the optical properties of one of the most common types of engineered tissues, collagen gels, and characterize their development when seeded with cells.

Collagen gels are one of the simplest types of engineered tissues, in which cells are suspended in a 3D collagen I matrix. Over time, the cells pull on the collagen fibrils causing gel compaction, where in the gel becomes smaller, with decreased water content and visibly more opaque. Some mesenchymal cells such as fibroblasts and smooth muscle cells (SMCs) also contract and remodel the collagen matrix [91]. An example of SMC-seeded collagen gels at 24 hr and 5 d is shown in Fig. 7.1. Note that the 24 hr gels are large and nearly transparent, while the 5 d gels have contracted and have a cloudy appearance.

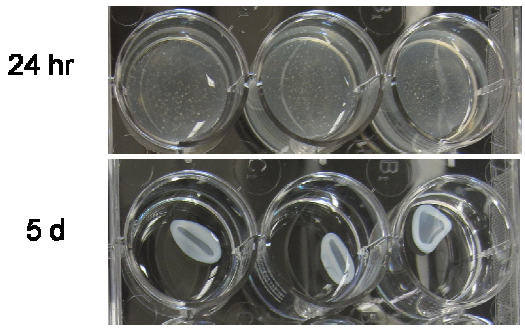

Fig. 7.1: Photographs of triplicate SMC collagen gels at 24 hr and 5 d. Well diameter = 2.26 cm.

In this paper, collagen gels are imaged with different cell-seeding densities over a 5-day period and the data used to measure their optical properties. Over time, the reflectivity of the gels increased while the attenuation did not change, which degraded the ability to visualize structures such as cells. This reflectivity increase was due to a

decrease in anisotropy g, which caused increased backscatter of light. No such changes were observed in acellular gels. In each set of gels imaged at 5 d, reflectivity values followed a bimodal distribution, with the major population of gel sites showing a doubling of reflectivity and a sizeable subpopulation showing a roughly 10-fold increase in reflectivity relative to the first 24 hr. Time dynamics of the gels showed that these changes in optical properties were gradual. A careful analysis of the optical properties measured during the earliest time point showed that a correlation existed between cell density and μ_s, but that cell density and g were uncorrelated; additional experimental data is provided in the appendix. Finally, mechanisms that could be responsible for the observed changes in optical properties are discussed.

7.2. Theory

The theory of light propagation in low-coherence imaging systems used to process the data in this paper was derived from the inverse Monte Carlo method [8]. For a homogeneous turbid medium characterized by a scattering coefficient μ_s, an anisotropy factor g, an absorption coefficient μ_a, and a refractive index n, the depth-dependent OCT reflectance signal R(z) can be described as an exponential decay:

$$R(z) = \rho e^{-\mu z} \tag{7.1}$$

where the reflectivity ρ [dimensionless] is the fraction of light delivered to the focus that is backscattered by the focal volume of tissue within the solid angle of collection of the microscope's objective lens, and the attenuation μ [cm^{-1}] describes the signal attenuation as light propagates to and from the focal volume. Specifically,

$$\rho = \mu_s b(g) \Delta z\,, \tag{7.2}$$

and

$$\mu = 2G(\mu_s a(g) + \mu_a), \tag{7.3}$$

in which Δz is the axial resolution of the imaging system and G is a geometry factor accounting for the extra pathlength caused by off-axis propagation during delivery and collection by the objective lens. Analysis has shown that for an objective lens with numerical aperture NA, the parameter G can be approximated by $1/\cos(\sin^{-1}(NA))$. For

low NA imaging systems frequently used in OCT, G is close to 1.0 (the exact value of G for high NA systems has been discussed [8]). The product $\mu_s \Delta z$ is the number of scattering events that occur within the focal volume, and the parameter b(g) represents the fraction of light scattered within the focal volume that is backscattered into solid angle of collection of the objective lens. For a medium with scattering phase function $p(\theta)$, b(g) is given by:

$$b(g) = \int_{\pi - \sin^{-1}(NA)}^{\pi} p(\theta) \cdot 2\pi \sin(\theta) d\theta \qquad (7.4)$$

In our analysis, a Henyey-Greenstein phase function [13] is assumed. One of the terms in Eq. 7.3 is a(g), $0 < a < 1$, that decreases the effectiveness of scattering when the scattering is forward directed such that photons, despite multiple scattering, still manage to reach the focus and cannot be distinguished from the unscattered light. For highly anisotropic media, a(g) has the effect of reducing the observed attenuation in the OCT signal. The function a(g) can be approximated by a numerical expression determined from Monte Carlo simulations:

$$a(g) = 1 - \exp\left(\frac{(1-g)^{0.6651}}{0.1555} \right). \qquad (7.5)$$

Experiments and numerical simulations have shown that this model is valid for confocal reflectance microscopes, which include both reflectance confocal microscopy (RCM) and OCT operated in focus-tracking mode [8]. The coherence gating in OCT improves on RCM by rejecting photons whose pathlength in the tissue does not match the round-trip pathlength to/from the focus, which yields about a 1000-fold noise reduction that enables deeper imaging [8]. Preliminary data show that this model is valid approximately up to a (one-way) optical depth of $\mu_s z = 3$, before multiple scattering begins to considerably interfere with the signal.

For this model to be valid, it is necessary to convert the interferometric OCT envelope (in arbitrary units) into dimensionless units of reflectance R(z), the fraction of delivered light that is collected and detected by the microscope. To do this, the signal is calibrated against the peak signal from a known interface, such as an oil-glass interface,

or against the reflectivity of an optical scattering phantom with known optical properties. This calibration is crucial in order to map the observations μ and ρ into the optical properties μ_s and g.

7.3. Materials and Methods

7.3.A. Cell culture

All cell culture materials were purchased from GIBCO unless otherwise noted. The experiments used primary SMCs isolated from a single baboon carotid artery that was chemically digested. Passage 9 SMCs were used in preparing collagen gels. The cells were fed with SMC growth medium (SGM), consisting of minimum essential medium (MEM) supplemented with 10 % fetal bovine serum, 1 % L-glutamine, and 1 % penicillin-streptomycin.

7.3.B. Collagen gel preparation

All collagen gels were prepared using the same basic protocol. Soluble calf skin collagen (MP Biomedicals, part # 150026) was dissolved in 0.02 N acetic acid at a concentration of 4.85 mg/ml. In preparing the collagen gels, 8 parts collagen (pH = 2.5) were mixed with 2 parts 5× MEM and 1 part 0.2 M NaOH (Sigma), with NaOH titrated until the pH was neutral as indicated by a color change in phenol red in the solution. Immediately thereafter, 5 parts SGM containing the predetermined number of cells were added to the mixture and aliquoted as 1 ml samples into a 12 well plate (Corning). The weakly scattering suspension thermally gelled for 1 hr at 37°. Thereafter, 1 ml SGM was added to feed each gel. Overall, 24 gels were prepared at each cell concentration (3.8×10^5, 1×10^6, and 2.1×10^6 cells/ml), which is denoted below as a "set" of collagen gels. Additionally, a set of acellular gels was also prepared and imaged. Acellular collagen gels were prepared in an identical manner to the SMC collagen gels, except that cells were absent from the mixed solutions.

Gels that were cultured for longer than 24 hr were detached from the well at 24 hr with a spatula and allowed to further compact. These gels were fed 1 ml SGM every 2 days. At each imaging time point, 3 gels were removed from their wells, and imaged by OCT. After OCT imaging, each sample was fixed for subsequent histological examination.

In addition to the 4 sets of collagen gels described above, optical property data acquired with a different OCT system are also presented. The two other sets of gels (one seeded with SMCs and one acellular) were imaged with a different OCT system at the 24 hr and 5 d time points. There were minor differences between these 2 sets and the 4 above, namely, the NA was 0.08 and the initial collagen density was 2 mg/ml. The OCT images, gel compaction data, and histology images for these two sets were nearly identical to the data presented here and are thus not shown. Altogether, imaging of the 6 sets of collagen gels was done over a span of 15 months.

7.3.C. OCT imaging

A time-domain OCT imaging system was setup as previously described [92]. Briefly, a 9 mW broadband light source operating at 1310 nm (B&W Tech) with a 94-nm full-width at half maximum (FWHM) bandwidth was coupled into a fiber-based Michelson interferometer. A rapid scanning optical delay line [81] varied the delay in the reference arm. A 10× microscope objective (Newport) focused the light on the sample. Both scanning mirrors in the reference and sample arms (x scanning) were from GSI Lumonics. The interference signal between the backreflected light from the sample and reference arms was measured using an InGaAs photodiode (New Focus). The OCT system was controlled through a data acquisition card (National Instruments) using software written in Matlab (Math Works). As the system scanned axially, the interference of the sample and reference arms yielded an oscillating signal. The Hilbert transform was performed in software post-acquisition using Matlab to specify the envelope of this oscillating signal, which was proportional to the reflected electric field. Squaring this envelope yielded the signal proportional to reflected intensity.

During OCT imaging, the sample was mounted on a glass slide and was immersed in MEM to maintain hydration throughout imaging. Each gel was imaged at 5 sites, with the sample repeatedly imaged 10-12 times at each imaging site. The sample orientation was randomized between imaging sites. In the 10-12 images acquired at each site, the translation stage on which the sample was mounted was manually moved towards the objective lens by 50 μm to a position (z'). An axial OCT scan versus depth z was obtained at each lens position, yielding a signal R(z, z'). In separate experiments using an oil-glass interface that could be positioned at different depths, a focus function was specified, F(z, z'), which accounted for the variation in response as the position of a structure of interest (z) deviated from the central focus position (z'). F(z, z') showed that the portions of each image in the range $z = z' \pm 25$ μm experienced only minor defocusing to roughly 81 % of the maximum value. Moreover, 50 μm was chosen as the focus shift distance since 25 μm is approximately 1/8 of the depth of focus in our OCT system (196 μm). The portions of each image in the range $z = z' \pm 25$ μm provided the strongest signals, and were stitched together to yield a final image. Defocusing effects were negligible in comparison to the speckle fluctuations in the signal, which spanned an order of magnitude. In this manner, a quasi-focus tracking image was prepared, appropriate for the theoretical OCT model.

7.3.D. OCT image processing algorithm

The OCT data from all samples were processed in a similar manner. A single, Matlab-based algorithm for evaluation of optical properties from the data was organized in the following separate modular steps:

1. The OCT data at each imaging site was read into Matlab and stitched together to form a quasi-focus tracked image. Using user-defined landmarks as points of reference (typically the air-sample interface or the corners of the sample), images taken at a single site were stitched together.
2. The data from a stitched image was then calibrated against the signal from a known reference. Initially, the data was calibrated against a mineral oil-glass

interface ($\rho = 1.826\times10^{-4}$). However, polystyrene sphere-agarose gel phantom data acquired during the same period of collagen gel imaging revealed that sphere phantoms are a more stable calibration method, and thus all the relevant collagen gel images were cross-calibrated against sphere data from 210 ROIs from 30 imaging sites in 6 phantoms.

3. To align OCT images, the most superficial pixel of the gel was found at each lateral x position, and the image was aligned by shifting each A-scan axially. For samples with the top surface located at the air-MEM interface, this edge was found by fitting a parabola to the interface pixels. For samples submerged in MEM with an irregular surface, the user manually drew a line along the gel surface using the computer mouse. Once the sample surface was identified, the A-scans were shifted accordingly.
4. The user subdivided each calibrated, stitched, aligned image into 5 regions of interest (ROI) along the x direction for fitting. The xz dimensions of each ROI were approximately 90×450 μm. The average signal over x at each z position yielded $R_{avg}(z)$.
5. For each ROI, $\ln(R_{avg})$ versus z was fit to Eq. 7.1 using a linear fit. A weighted-least-squares fitting routine was used, with the weight at each z pixel being inversely proportional to the variance of the signal through all the x pixels at that depth. In addition to the fitted parameters μ and ρ, and their respective confidence intervals, goodness-of-fit statistics – the mean pixel error and the adjusted regression coefficient R^2 – were documented for each ROI.

7.3.E. Gel compaction

Collagen gel compaction was monitored in the gels at 8 time points and expressed as a percent of the initial gel volume (1 ml). The volume of the gels was indirectly measured via the volume of the media in the well that could be aspirated after compaction, i.e., gel volume = 2 ml – aspirated volume, with the 2 ml coming from a 1 ml gel fed with 1 ml SGM. The gel compaction was measured on SMC-gels with 3 cell

seeding densities and an initial collagen density of 2.43 mg/ml. Calibration experiments showed that this method overestimated the collagen gel volume by <50 μl.

7.3.F. Histology

After imaging, samples were fixed overnight in 10% neutral buffered formalin and stored in 70% ethanol at 4° C. The samples were embedded in paraffin, and 5 μm sections were cut and stained with hematoxylin and eosin (H&E) on glass slides. Sections of the selected samples were cut from positions starting at 1/2 the radius of the sample towards the center, in 50 μm increments. The histological sections were cut so they would expose a cross section of the gels, but they did not exactly match the imaging planes in the OCT data since the gel orientation was randomized between the imaging sites. The histological sections were imaged by phase contrast microscopy (Optiphot) at 20×.

7.3.G. Data analysis and statistics

Each linear fit of $R_{avg}(z)$ data at each ROI resulted in a (μ, ρ) pair. The (μ, ρ) data were plotted as a scatter plot against a grid of iso-μ_s and iso-g contours generated by the model of Eqs. 7.1-3. The contours map experiment to theory. Alternatively, the data were assessed by looking at the distributions of fitted (μ, ρ) values. For both μ and ρ, the probability density functions (PDFs), $f(\mu)$ and $f(\rho)$, were computed by binning $\log_{10}(\mu)$ and $\log_{10}(\rho)$ values from an individual group into histograms made of Gaussian shaped kernels. Treating μ and ρ as statistically independent random variables, a joint PDF was computed using $f(\mu, \rho) = f(\mu)f(\rho)$. Finally, the peaks of the (μ, ρ) joint PDFs were mapped back to (μ_s, g) with the *a priori* knowledge of the basic system parameters Δz and NA using Eq. 7.2-3.

To determine the accuracy and precision of the algorithm used in this paper, preliminary experiments were conducted to statistically characterize the fitting results.

Specifically, intra-ROI, inter-ROI, inter-site, and inter-sample coefficients of variation were calculated for sphere phantoms, 24 hr collagen gels, and 5 d collagen gels (Table 7.1). Data in Table 7.1 are expressed as means ± standard deviation over n samples, and are in units of percent. The intra-ROI variability describes the reproducibility of 10 measurements of μ and ρ on the same ROI. The inter-ROI variability describes the variation of the mean μ and ρ of each ROI between 5 ROIs on the same site on a gel. The inter-site variability describes the variation of the mean data of 5 ROIs on a site between 5 sites on the same phantom/collagen gel. The inter-sample variability describes the variation of the mean data of 5 sites on one phantom between 3 different phantoms (or collagen gels). Because of this averaging, the inter-site and inter-sample variability in Table 7.1 are lower than the inter-ROI measurements.

Table 7.1: Statistics describing the reproducibility of the algorithm. Listed are the coefficients of variation for intra-ROI, inter-ROI, inter-site, and inter-sample measurement in both μ and ρ. The μ and ρ values presented are expressed in percent as means ± standard deviations over n samples. Data is given for sphere phantoms, as well as the key timepoints of 1 and 5 d during collagen gel development. * – outliers that are beyond 3 standard deviations from the mean (<4 % of data) were excluded.

Sample type	Sphere phantoms		
	n	μ	ρ
Intra-ROI*	84	5.1±4.2	9.1±5.1
Inter-ROI	30	5.3±2.7	13.3±5.7
Inter-site	6	4.0±2.6	12.0±3.9
Inter-sample	3	4.8±1.9	17.5±5.9

Table 7.1, continued:

Sample type	Collagen gels, 1 d			Collagen gels, 5 d		
	n	μ	ρ	n	μ	ρ
Intra-ROI*	63	35.4±24.3	19.1±6.1	63	19.0±12.8	19.9±11.3
Inter-ROI	45	39.9±24.8	30.6±13.9	46	38.8±25.4	23.4±13.8
Inter-site	9	28.6±9.5	30.7±11.6	9	35.2±9.6	30.3±21.8
Inter-sample	3	25.4±14.1	34.7±14.5	3	47.9±28.4	53.1±41.6

The sphere data in Table 7.1 illustrate the accuracy and reproducibility of the measurements, the 24 hr collagen gel data illustrate the inherent variations in the gel preparation, and the 5 d collagen gel data illustrate the inherent variations in gel development. The resolution of the algorithm for determining optical properties was specified as the FWHM of the PDF for either μ or ρ values. The FWHM resolution in μ was finite at 20 cm^{-1}. For ρ, the resolution scaled with the fitted results, with the FWHM being ~20 % of the mean. In terms of accuracy, the algorithm output was shown to overestimate the theoretically predicted (μ, ρ) values by ~10 %.

7.4. Results

7.4.A. Ability to visualize cells in OCT images of collagen gels decreases with time

Representative images of collagen gels with different cell seeding densities (acellular, 3.8×10^5, 1×10^6, and 2.1×10^6 cells/ml) at 6 hr, 24 hr, and 5 d are shown in Fig. 7.2A-L, with corresponding histology for the SMC gels in Fig. 7.2M-U. The bright line on the top of some of the OCT images represents the air-MEM interface. Overall, the OCT images appeared rather spatially uniform at any given time-point, with the only visualized structures being bright spots that presumably represent individual cells or clusters of cells. Such bright spots on a weakly scattering background can be seen in the 6 hr images of SMC gels (Fig. 7.2B-D). The density of these small "bright" spots increases with increasing cell seeding density. The bright spots were ~20 μm in size, comparable to SMCs. At 24 hr (Fig. 7.2E-H), a few more of these bright spots can be seen in the 2.1×10^6 gels (Fig. 7.2H), and to a lesser extent in the 1×10^6 and 3.8×10^5 gels (Fig. 7.2F-G). At 5 d (Fig. 7.2I-L), the images look different. In the 3.8×10^5 gels (Fig. 7.2J), there are a few bright spots that are difficult to resolve. The 1×10^6 and 2.1×10^6 gels (Fig. 7.2K-L) show a superficial high signal region that decays. For both gel conditions, it is not possible to resolve any cells in the foreground, as the bright spots have blended into the signal rich background. Note that because of the high superficial signal and the attenuation, the images appeared featureless and uniform. These gels have

entered a scattering regime in which qualitative image visualization does not yield much useful information, and in which a quantitative image processing technique is needed. In all the acellular samples (Figs. 7.2A, 7.2E, and 7.2I), there were larger, modestly brighter and darker regions in the background of all the images caused by heterogeneity in scattering from the collagen, which did not appear to change much over time. Histologically, the H&E sections in Fig. 7.2M-U show an increase in cell density over time for each of the 3 different seeding densities.

7.4.B. Collagen gels exhibit an increase in reflectivity/decrease in anisotropy over time

The optical properties of the developing collagen gels from a single representative set are shown on a scatter plot in Fig. 7.3. Also plotted on the scatter plot is a grid that maps theoretical (μ_s, g) values to the observed (μ, ρ) pairs. Here, the initial collagen density was 2.43 mg/ml and the initial cell density was 1×10^6 cells/ml. Fig. 7.3 compares SMC and acellular gels at two key time points of 1 and 5 d, with each datum point representing a (μ, ρ) pair from a single ROI. In assessing the SMC and acellular gels at 24 hr, the relative proximity of these two groups suggests that the scattering is dominated by the collagen fibrils, not the cells, which make sense given the small volume fraction the cells occupy. Also, note that the reflectivity in the SMC gels more than doubled from 1-5 d, while the corresponding acellular gels had only a modest increase in reflectivity. There was a large variance in attenuation values in all the samples. This feature has been observed consistently over multiple sets of collagen gels, and results in poorer ability to resolve μ in collagen gels, in contrast to sphere phantoms (Table 7.1). Moreover, neither the SMC nor acellular gels experienced a major shift in attenuation over 5 d.

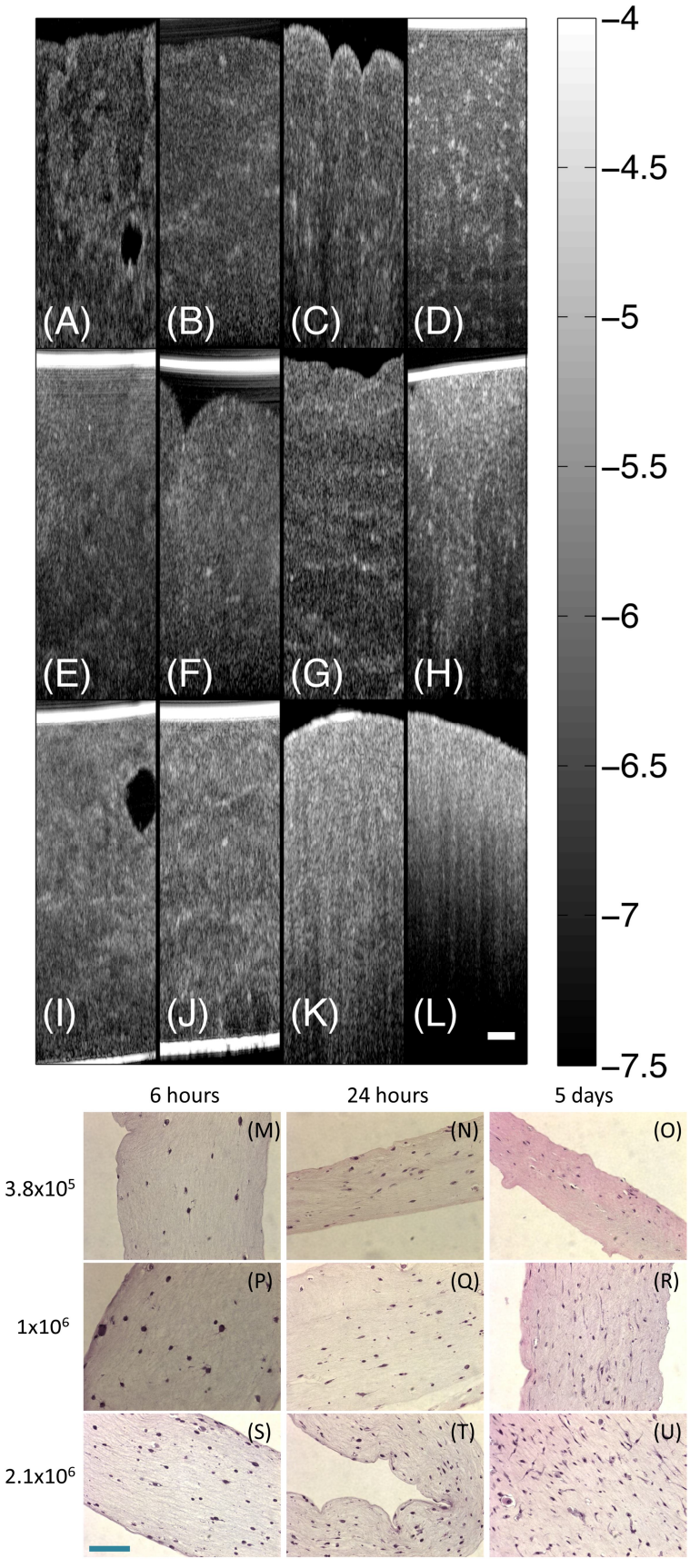
(A)
(B)
(C)
(D)
(E)
(F)
(G)
(H)
(I)
(J)
(K)
(L)
−4
−4.5
−5
−5.5
−6
−6.5
−7
−7.5
6 hours
24 hours
5 days
3.8x10^5
1x10^6
2.1x10^6
(M)
(N)
(O)
(P)
(Q)
(R)
(S)
(T)
(U)

Fig. 7.2 *(on previous page)*: (A-L) – Representative OCT images at 6 hr (A-D), 24 hr (E-H) and 5 d (I-L) for acellular gels and 3 different cell seeding densities. Acellular gels are shown in (A, E, I); gels seeded with 3.8×10^5 cells/ml are shown in (B, F, J); 1×10^6 cell/ml gels are shown in (C, G, K); and 2.1×10^6 cell/ml gels are shown in (D, H, L). Note that other than a few bright spots, the images (particularly at 5 d) are rather featureless, making visual characterization difficult. The bright spots are presumed to be cells or clusters of cells. Gray scale represents $\log_{10}(\rho)$. (M-U) – Corresponding histology for the 3 seeding densities of SMC gels: 6 hr (M-O), 24 hr (P-R), and 5 d (S-U). Gels seeded with 3.8×10^5 cells/ml are shown in (M, P, S); 1×10^6 cell/ml gels are shown in (N, Q, T); and 2.1×10^6 cell/ml gels are shown in (O, R, U). The histology images show an increase in cell density took place for the 3 sets of gels over time. Bar = 100 μm.

A summary of the optical property results from multiple sets of collagen gels is detailed in Table 7.2. Table 7.2 lists the peak values and range (±1/e or ±0.37 of peak value) for each μ and ρ of the joint PDFs. These ranges provide an estimate of how μ and ρ values were distributed around the joint PDF peaks. In comparing multiple sets of gels, the optical properties follow a general trend of starting out at low reflectivity and low attenuation at times <24 hr, and gradually increasing reflectivity over 5 days, approximately 2-fold, while attenuation remained relatively constant. These observed (μ, ρ) pairs corresponded to μ_s values that varied greatly, from 7-93 cm^{-1}, while g values were consistently closely centered around 0.90 in the first 24 hr. At 5 d, μ_s values of SMC gels consistently decreased 30-50 %, while g decreased to approximately 0.75. Moreover, at 5 d there was also a consistent subpopulation of data with higher reflectivity values, which were approximately 10-fold the reflectivity observed in the first 24 hr. Thus, at 5 d the reflectivity of collagen gels followed a bimodal distribution as can be seen in the reported peak ranges in Table 7.2. Note that the peak ρ value is consistently closer to the lower boundary than the upper boundary, which suggests that although most of the data were centered around the peak, there was always a sizeable subpopulation with even higher ρ values. In contrast to the SMC gels, acellular gels from Set 4 and Set

6 had very minor shifts towards either higher or lower reflectivity, respectively. Nonetheless, despite a large variance in μ, the increase in ρ of collagen gels over time was both consistent and reproducible. Thus, while the spatial heterogeneity of collagen structures in the acellular gels remained constant over time, the subpopulation of higher ρ values across the various sets of 5 d SMC gels suggests that some spatial heterogeneity developed in the SMC gels over time.

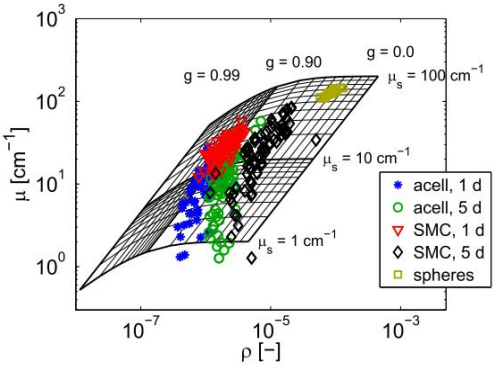

Fig. 7.3: Representative scatter plot showing the overall trends in (μ, ρ) data from both SMC and acellular gels at 1 and 5 days. Each point represents the fit results from an individual ROI. Note that at 1 d there was overlap between the SMC and acellular gel data, but at 5 d the (μ, ρ) data from SMC and acellular gels have drifted apart. The data displayed here corresponds to Sets 2 and 4 in Table 1, with an initial collagen density was 2.43 mg/ml and an initial cell density (passage 9) of 1×10^6 cell/ml.

7.4.C. Time dynamics of collagen gels

While Fig. 7.3 shows the overall shift in the local optical properties of the collagen gels, it is also worthwhile to visualize the time dynamics of the optical properties. However, since the shift in the (μ, ρ) data over time is slow, and many data points lie on top of one another, the actual 2D distribution of μ and ρ values is presented as the joint PDF. A representative set of the calculated joint PDFs at 6 hr, 24 hr, 3 d, and 5 d are plotted superimposed on a grid in Fig. 7.4A-D, showing the gradual increase in reflectivity over 5 days. Fig. 7.4A-B shows that there are not many changes in the optical properties over the first 24 hr. However, from 1 to 5 d (Fig. 7.4B-D) the center of the PDF shifted to the right towards higher reflectivity, without changing much in

attenuation. There was also a substantial subpopulation in the 5 d time point that had an even higher reflectivity (lower anisotropy), similar to the other data sets (Table 7.2).

Table 7.2: Summary of optical properties from multiple sets of collagen gels. Data reported from the earliest time point (6 hr in sets 1-3, 24 hr in sets 4-5) to the final time point (5 d for all sets). For both μ and ρ, we report both the peak of the joint PDF and the range over which the joint PDF > 1/e * maximum. [] denotes concentration. Collagen density units are mg/ml; cell density units are cells/ml; μ and μ_s units are cm^{-1}; ρ and g units are dimensionless. Pas. denotes cell passage number. * – Note that sets 5-6 were imaged with a different OCT system. # – Note 3 samples were imaged at 8 different time points. § – The initial collagen concentration in the gels imaged at 1d and 5 d were 2 mg/ml and 5 mg/ml, respectively.

Set	# gels	$[collagen]_{t=0}$	$[cell]_{t=0}$	Pas.	μ_{early}	μ_{final}	μ_{early} pk. range	μ_{final} pk. range
1	24	2.43	3.8×10^5	9	16.22	15.31	4.37-35.48	6.38-36.31
2	24	2.43	1×10^6	9	30.90	30.55	16.79-49.55	6.68-80.35
3	24	2.43	2.1×10^6	9	43.15	53.09	17.99-76.86	24.55-84.14
4	3#	2.43	0	NA	10.47	15.14	4.57-29.51	4.37-32.36
5*	6	2	1×10^6	5	59.57	48.98	14.62-117.49	17.99-108.39
6*	6	2 or 5§	0	NA	38.46	60.26	9.12-92.26	26.00-89.13

Table 7.2, continued:

Set	ρ_{early}	ρ_{final}	ρ_{early} pk. range	ρ_{final} pk. range	$\mu_{s\text{-}early}$	$\mu_{s\text{-}final}$	g_{early}	g_{final}
1	1.38×10^{-6}	2.95×10^{-6}	$5.19\text{-}29.2\times10^{-7}$	$2.16\text{-}3.94\times10^{-6}$	10.50	8.19	0.896	0.756
2	2.16×10^{-6}	5.37×10^{-6}	$1.01\text{-}3.51\times10^{-6}$	$2.60\text{-}21.1\times10^{-6}$	21.69	16.55	0.919	0.775
3	3.27×10^{-6}	4.79×10^{-6}	$7.16\text{-}73.3\times10^{-7}$	$2.40\text{-}29.5\times10^{-6}$	29.23	33.66	0.910	0.889
4	7.76×10^{-7}	1.80×10^{-6}	$4.37\text{-}11.78\times10^{-7}$	$1.11\text{-}3.09\times10^{-6}$	7.16	8.85	0.913	0.847
5*	1.15×10^{-6}	2.48×10^{-6}	$7.16\text{-}21.4\times10^{-7}$	$1.30\text{-}5.01\times10^{-6}$	37.30	25.75	0.878	0.690
6*	4.95×10^{-7}	3.05×10^{-7}	$1.93\text{-}12.6\times10^{-7}$	$1.35\text{-}5.62\times10^{-7}$	28.32	93.47	0.927	0.985

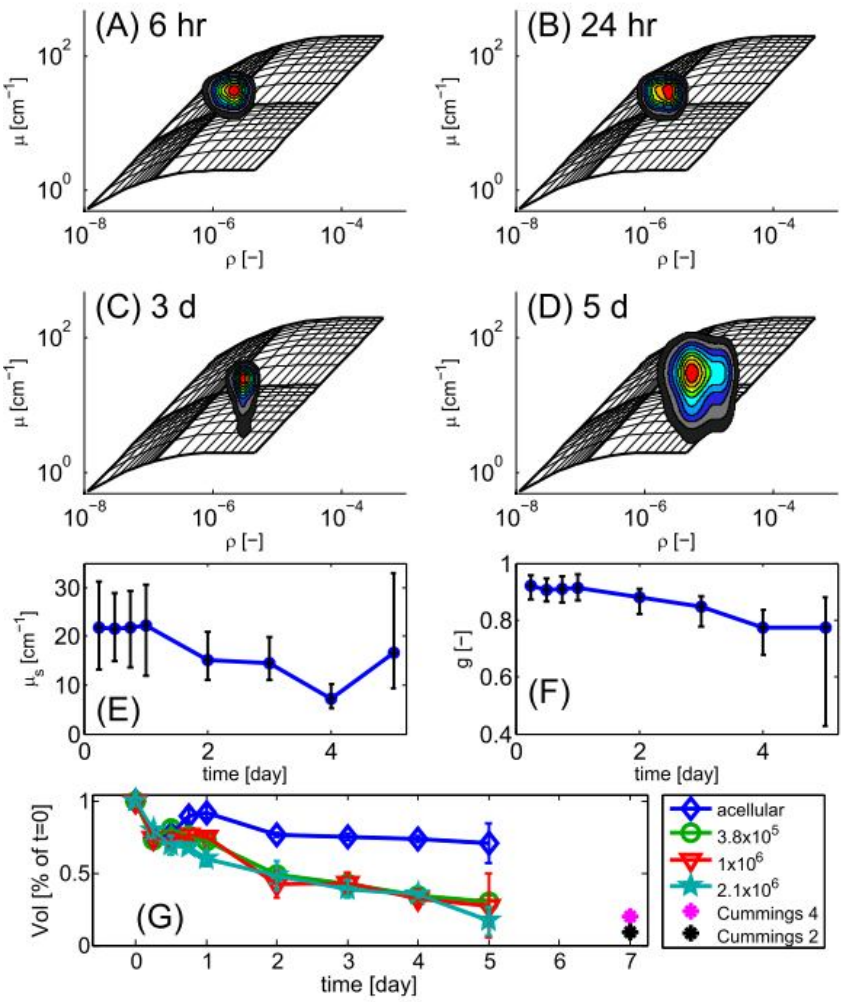

Fig. 7.4: Log-log plots showing 2D PDFs of collagen gels at 6 hr, 24 hr, 3 d, and 5 d (A-D). Also on each plot is a grid that shows how theoretical optical properties (μ_s, g) map to (μ, ρ) in our OCT system. Over time, the center of the PDF moves to the right, showing an increase in reflectivity. Moreover, the 5 d PDF also has a subpopulation at higher ρ values, indicating that a subpopulation of the ROIs had a higher reflectivity. (E-F) Plots of peaks in (μ, ρ) space that were mapped back to (μ_s, g), plotted versus time. The displayed data in (A-F) correspond to Set 2 in Table 1, in which the initial collagen density was 2.43 mg/ml, and the initial cell density (passage 9) was 1×10^6 cells/ml. (G) Gel compaction curve for the gels versus time. These data correspond to Sets 1-4 in Table 1; the first 4 legend entries represent initial cell concentrations in units of cells/ml. Cummings' gels had a 1×10^6 cell/ml seeding density, and an initial collagen density of either 4 or 2 mg/ml [37].

Additionally, the peaks of the joint PDFs shown in Fig. 7.4A-D were mapped from (μ, ρ) space back to (μ_s, g) space. Plots of μ_s and g versus time for 8 timepoints spanning 5 days are displayed in Fig. 7.4E-F. Error bars represent the 1/e width of the joint PDF at the iso-μ_s and iso-g lines of the PDF peak. The g versus time curve (Fig. 7.4F) shows that over 1-5 days, there was a moderate but steady decrease in anisotropy. A similar moderate but steady decrease is also seen in the μ_s versus time plot (Fig. 7.4E). Note the nonlinear mapping of (μ_s, g) to (μ, ρ) that occurs at g values >0.9, such that reflectivity can increase and attenuation can show no change while g and μ_s both decrease.

Macroscopically, the SMC collagen gels showed a moderate but consistent rate of gel compaction, i.e., the rate of decrease in collagen gel volume as the cells pull on the fibrils was steady (Fig. 7.4G). Gel compaction was assessed at the 8 imaging time points by quantifying the volume of media in the gel well just before imaging. The volume of gels from each of the 3 SMC groups shrunk to about 20-30% of their original volume. These data agreed with end point measurements by Cummings et al [37].

7.4.D. Cell density correlates with scattering coefficient of collagen gels

When analyzing the optical property results, the 6 hr data were closest to the 0 time point and thus had minimal change in both the cells and the collagen. In plotting the peaks of the joint PDFs on a grid (Fig. 7.5A), these (μ, ρ) pair were co-located on an iso-g line, and that their μ_s value increased with cell concentration. The corresponding μ_s and g values for the 4 points were backtracked, as in Fig. 7.4E-F, and plotted against the cell seeding density (Fig. 7.5B-C). Included in Fig. 7.5B-C are linear fits of both μ_s and g against cell seeding density. The fit results showed that μ_s was highly correlated with cell concentration (R^2=0.998) and increased linearly with cell density at a rate of 10.8 $cm^{-1}/(10^6$ cells/ml) plus a 7.0 cm^{-1} offset that represents scattering from collagen alone (Fig. 7.5B). Moreover, the 7.0 cm^{-1} measured from 2.43 mg/ml acellular collagen corresponds to a μ_s increase of 2.88 cm^{-1} per (mg/ml) of collagen density. A similarly high correlation

(R^2 = 0.985) between cell density and μ_s was obtained by correlating cell-like structures (i.e., "bright spots") counted manually in the 6 hr gel images (data not shown). In contrast to μ_s, g remained flat relative to the concentration (Fig. 7.5C) and was uncorrelated (R^2=0.035). Similar plots of μs and g versus cell density are shown in the appendix of this chapter (Section 7.7). Such an increase in μ_s without a change in g is expected for a static system with increasing scattering particle (i.e., cell) density. However, the imaged collagen gels are dynamic over 5 days, and no such clear cut correlations existed between either μ_s or g and cell concentration at any of the later timepoints. This suggests that over 5 d the contraction process involved a fundamental change in the overall collagen gel architecture.

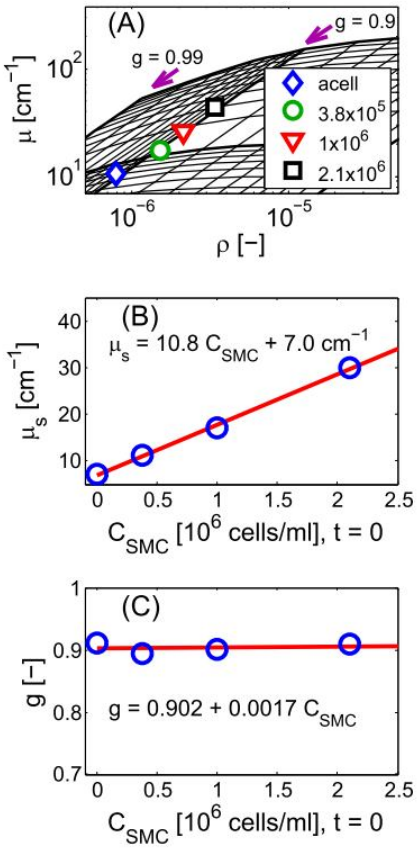

Fig. 7.5: (A) Peak of μ and ρ PDFs from 6 hr gels plotted on grid. Note how all the points line up on the same iso-g line, with increasing μ_s values. These data correspond to Sets 1-4 in Table 1; the units on the legend are cells/ml. Plots of (B) μ_s and (C) g data calculated from the (μ, ρ) PDFs for the 4 cell densities, along with corresponding linear fits. Note that μ_s increases linearly with cell density, while g does not change.

7.5. Discussion

In this paper, OCT was used to image developing collagen gels at different time points, and to measure the optical properties from the images by fitting the OCT signal to a theoretical model. The results showed that over time, there was a consistent 2-fold increase in reflectivity with little change in the attenuation in 4 separate sets of experiments with various cell seeding densities (Table 7.2, Figs. 7.3-4). Also, consistently present in each set of gels imaged at 5 d was a sizeable subpopulation of sites on the gel with a higher reflectivity, roughly 10-fold greater than the first 24 hr. These trends in attenuation μ and reflectivity ρ correspond to a decrease in anisotropy g and a moderate decrease in scattering coefficient μ_s, suggesting an overall decrease in the size of the scattering particles.

Several models have been proposed for measuring optical properties from OCT signals. The first model is the single scattering (SS) model, in which the signal is assumed to follow an exponential decay $R(z) \propto \exp(-2(\mu_s + \mu_a)z) \approx \exp(-2\mu_s z)$, since $\mu_s >> \mu_a$ for most tissues at NIR wavelengths. Despite similarities between the SS model and the μ-ρ model used here, our results illustrate several flaws in using the SS model for measuring optical properties. Firstly, the μ-ρ model fits two parameters that map back to two unknowns, μ_s and g, whereas the SS model only fits one parameter (μ_s). However, our results repeatedly showed that the shift with time in optical properties of the collagen gels was more clearly observed in g, not μ_s. Secondly, the main difference in the attenuation term of the two models is the factor a(g), which describes how scattered light can still reach the focus despite multiple scattering. It is a(g) that makes the mapping from μ_s to μ non-linear (and hence non-trivial) at high g values, to which the 6-24 hr collagen gel (μ, ρ) data mapped.

Most of the work on fitting optical properties from OCT imaging has focused on differentiating different types of atherosclerotic plaques [30, 79, 93]. Each of these

studies used a different theoretical model. Van der Meer et al [93] used the SS model and showed differences in μ_s between normal arteries and atherosclerotic plaques. Levitz et al [30] used the extended Huygens-Fresnel (EHF) model [9] and showed differences in anisotropy between normal arteries and atherosclerotic plaques. The EHF model has the added advantage of accounting for multiple scattering and defocusing, that is, it is capable of evaluating both μ_s and a measure of anisotropy similar to g without the need for the (time consuming) quasi-focus tracking scheme implemented in our study. However, the EHF model is highly non-linear and thus requires a computationally burdensome algorithm that does not always converge to a solution. Alternatively, there are other models that have been used to measure optical properties from highly-scattering samples. The model used by Xu et al [79] is very similar to the μ-ρ model used here, but with key differences. First, the a(g) is missing from this model, and second, ρ is represented as the backscattering coefficient μ_b, with no nonlinear mapping back to g.

Similar to our work, Xu et al [94] characterized cytochrome oxidase activity in astrocytes suspended in agarose gels by measuring changes in μ_a via the fitted attenuation, but using the SS model with its inherent limitations. Nonetheless, it is also worth noting that in their cell-agarose samples, a negligible amount of scattering and absorption from the agarose contributed to the signal, thus all the scattering and absorption measured could be attributed to the cells. Fig. 7.5 shows that cells are mild scatterers and that a very high density is needed to obtain a measureable change in attenuation. The attenuation values measured by Xu et al [94] required very high cell seeding densities ($\sim 10^7$-10^8 cells/ml), which is in general agreement with our results.

The experiments presented here highlight several advantages to measuring local optical properties of samples using OCT. The method is non-destructive, which makes continuous and time-lapse monitoring of the tissue gels feasible. Since this OCT method depends on endogenous contrast, no labels are needed, which has the added benefits of both preserving the sample unperturbed in its native environment and reducing the costs associated with fluorescent labels. Moreover, the visual information contained in the OCT images complements the quantitative optical property data. And although these

experiments were destructive in nature – samples were prepared, removed from the sterile incubator and imaged, and then fixed for histological analysis –one of OCT's primary advantages is that it is a fiber-based technology that can be sterilized and integrated into the incubator for continuous, time-lapse monitoring [86]. The adaptation of confocal mosaicing technology [95] to OCT will enable rapid surveying of large sample volumes. These features, if successfully implemented, could enable automated non-destructive evaluation of large volumes of engineered tissues.

In this study, samples were imaged, and images were further divided into volume regions of about $90\times10\times450$ μm (xyz), or 0.4 nanoliters. This resulted in a rather large number of ROIs with volumes on the nanoliter scale, which partly affected the analyses. Implicit in the definition of μ_s and g is the assumption of averaging over some volume. The nanoliter volumes assessed here approach the size limit over which these properties are defined, but nonetheless, it is still possible to define optical properties within these volumes. These small volumes, from which optical properties are measured, are a direct consequence of the spatial resolution and field of view of OCT images. Indeed, ROI volumes on the nanoliter scale have been used by others when measuring optical properties from OCT data [30, 79, 93, 94].

One consequence of these small sampling volumes is an increase in the variance of the optical properties, which may simply reflect the intrinsic heterogeneity of the samples on this size scale. The variance in optical properties of acellular gels was much larger than those in SMC gels (Figs. 7.3-4, Table 7.2), paradoxically suggesting that acellular gels were less homogeneous than SMC gels. However, this is not the complete picture. A careful examination of the acellular gels with the naked eye showed that some regions are cloudier than others, confirming millimeter scale heterogeneity seen in the OCT images and observed in the optical property data. Moreover, the histological sections (Fig. 7.2M-U) showed that within the field of view of an OCT or histology image, the cells were generally uniformly distributed. Noting that cells are mild scatterers but with a higher reflectivity than the background collagen, the scattering in the SMC gels from the "uniformly" distributed cells contrasted with the collagen background

and shifted the optical properties accordingly. However, in the acellular gels all the scattering was due to the slowly varying background, which explains the increased variance observed in the acellular gels. Indeed, perhaps the large spatial variability in collagen distribution may offer clues as to why some regions in tissue engineered implants are at increased risk of mechanical failure [44].

The optical properties at 5 d showed a consistent increase in ρ with little change in μ, which correspond to a decrease in anisotropy g with a modest decrease in μ_s. Such changes in optical properties suggest a decrease in the overall size of the scattering particles, not an increase in particle density, which would increase μ_s, and hence increase both μ and ρ. In attempting to identify which microstructural changes caused this shift in optical properties, we (initially) proposed 4 potential reasons: increased collagen density, increased cell density, SMC contraction (i.e., a change in cell morphology), and collagen remodeling. Further analyses of some of the data presented here rules out increases in collagen and cell density, and preliminary results (not shown) suggest that collagen remodeling is responsible for the changes in optical properties.

To test if increased collagen density – i.e., gel compaction – caused the 2-fold increase in reflectivity, the collagen density was plotted against both μ and ρ for the different collagen gel samples and the correlation coefficient was calculated. There was little to no correlation between collagen density and optical properties – for ρ versus collagen density, $R^2 < 0.2$; for μ versus collagen density: $R^2 < 0.06$ (data not shown). These poor correlations suggest that collagen density was not the primary cause of the measured shifts in optical properties. Furthermore, the changes in optical properties caused by changes in collagen density were very subtle ($\mu_s = 2.88\ cm^{-1}/(mg/ml)_{collagen}$), and are well below the 14 cm^{-1} algorithm resolution for μ_s at g = 0.9. Such an increase in μ_s with little change in g does not explain the shift in optical properties over time observed in our data, namely a decrease in g a modest decrease in μ_s. Also, data from Set 6 (Table 7.2), in which higher density (5 mg/ml) acellular gels were imaged at 5 d, suggests that gel compaction did not cause the change in optical properties, since the

characteristic increase in reflectivity (with no change in attenuation) that was consistently observed in the SMC gels was absent. Of note, we do not expect that extracellular matrix laid down by SMCs over the 5 day incubation period contributed significantly to the change in optical properties, since previous work has shown the matrix synthesized by SMCs embedded in both collagen and fibrin gels to make up <1 % of the total collagen content [38, 51].

Additionally, the correlation between the optical properties and cell density was checked. An increase in cell density may be caused either by cell proliferation and/or compounded by gel compaction. However, an alamar blue assay on 3 extra sets of gels did not show an increase in cell metabolism over 5 d, suggesting no proliferation took place (data not shown). The result is in agreement with previously published results [49]. Nonetheless, to confirm whether cell density correlates with optical properties, cells were manually counted in 15 histological H&E sections for each gel (3 analogous sites in 5 sections separated by 50 μm), which were normalized by the area of the collagen in that section. These cell density counts [cells/μm^2] were compared to both the μ and ρ values for that gel, and the correlation coefficient R^2 was calculated. The correlations between the cell density and both μ and ρ were rather weak. For μ versus cell density, $R^2 = 0.25$, while for ρ versus cell density $R^2 = 0.34$ (data not shown). These weak correlations, together with the 6 hr data showing how cell density correlates with μ_s but not g (Fig. 7.5) suggest that although an increase in cell density contributed partly to an increase in ρ, it was not the primary reason for the 2-fold increase in ρ shown in the data.

The data showed that over time, there was an overall decrease in anisotropy factor g of the collagen gels, as well as a moderate decrease in scattering coefficient μ_s. The decrease in μ_s seems a bit counterintuitive, since it is expected for there to be an overall increase in the density of scattering particles. However, treating the scattering particles in the gels as discretely sized microspheres, Mie theory provides some additional insight [11]. Mie theory states that the relationship between the particle size and scattering cross section is highly nonlinear. Thus, consider two scattering solutions, one made with small microspheres and the other with large microspheres, but where in both cases the spheres

occupy the same volume fraction. It is obvious that the small sphere solution will have a smaller g value than the large sphere solution. However, these two scattering media will also have different μ_s values, with the small sphere solution having a smaller μ_s than the large sphere solution. Thus, if the increase in the number of small scattering particles (as indicated by the higher reflectivity) was caused by a breakdown of larger particles, one would expect a moderate decrease in the μ_s along with a decrease in g. Such a scenario supports the hypothesis that remodeling of the collagen matrix into small fibril fragments caused the observed changes in optical properties.

7.6. Conclusion

In this study, OCT was used to image development in several sets of collagen gels with different cell seeding densities, as well as acellular gels, over a 5-day period. After the first 24 hr, changes in the collagen gels made structures (i.e., cells) impossible to resolve. To characterize the samples quantitatively, the optical properties of the gels were determined using an image processing algorithm that fit the OCT signal from a region of interest to a theoretical model. In doing so, the observed fit results (attenuation μ and reflectivity ρ), were mapped back to the optical properties, the scattering coefficient μ_s and the scattering anisotropy factor g. Within the first 24 hr, the optical properties of the SMC and acellular gels were similar (Figs. 7.3-4), suggesting that the optical properties were dominated by scattering from collagen fibrils. Over time, collagen gels with SMCs consistently exhibited a 2-fold increase in reflectivity, while acellular gels did not (Figs. 7.3-4, Table 7.2). The shift in optical properties towards higher reflectivity was gradual. A sizeable subpopulation of the SMC gels at 5 d had reflectivity values roughly 10-fold higher than those in the first 24 hr were consistently observed in 5 sets of gels. Such a shift corresponded to a decrease in g and an overall decrease in the size of the scattering particles. Additionally, at the earliest imaging time point (6 hr, Fig. 7.5), cell seeding density was strongly correlated to μ_s (R^2>0.99), but not to g (R^2=0.02). All in all, the data suggests that SMCs change the architecture of the collagen gel, and that OCT can visualize and quantify these changes.

7.7. Appendix: cell density versus optical properties

In addition to the data presented in the Fig. 7.5, the experiment determining the relationship between cell density and optical properties was repeated twice. The results, which were not published along with the rest of the chapter, are presented in this appendix.

7.7.A. Methods: Imaging and analysis

The general protocol used to prepare the collagen gels, image the collagen gels, and analyze the OCT data were very similar to those described in Sections 7.3.B-D, but with a few notable differences in gel preparation, imaging, and analysis. In terms of gel preparation, the two repetitions of the experiment each used SMCs isolated from different baboons. Moreover, in both cases, passage 5 cells (not passage 9) were used. In one repetition, the gels were cast in 12-well plates (as in Section 3.B) while in the other repetition the gels were cast in 24-well plates. Instead of imaging after 6 hr, the gels were imaged after 3 hr. Triplicate collagen gels were prepared for each cell density. Moreover, only one or two triplicates (3 or 6 gels) were imaged during each imaging session to minimize the time differences between gel preparation and imaging. In the experiment in which the gels were prepared in 12-well plates, 6 different cell concentrations were used: 0 (acellular), 5×10^5, 7.5×10^5, 1×10^6, 1.5×10^6, and 2.25×10^6. In the experiment in 24 well plates, 4 different cell concentrations were used: 0 (acellular), 7.5×10^5, 1.3×10^6, and 2.05×10^6 cells/ml.

In terms of OCT imaging and analysis, the OCT system used to image the gels was modified such that it had an additional lateral scan axis (y scanning), and a piezo-controlled objective lens mount to acquire quasi-focus-tracked data in an automated manner. During imaging, one 3D dataset spanning $350\times300\times1000$ μm (xyz) was acquired at 1 site per sample. After OCT imaging, the 3D data was subdivided into 10×10 ROIs, and the optical properties were evaluated from each ROI using the algorithm outline in Section 7.4, resulting in a single (μ, ρ) pair per ROI.

To analyze the data, all the (μ, ρ) data from a single cell density were grouped together, and a joint PDF was calculated for each group. The (μ, ρ) values that correspond to the peak of the 2D PDF were found, and these (μ, ρ) values of the peak were mapped back to (μ_s, g). Thus, each imaged group of collagen gels with a specified cell density resulted in a single (μ_s, g) pair. These μ_s and g data were used to determine the relationship between the optical properties and the cell seeding density.

7.7.B. Additional results: Cell density versus optical properties

The optical properties of the gels casted in 12-well plates, 24-well plates, as well as the gels from Fig. 7.5 are all plotted in Fig. 7.6 as a function of cell density. Plot of μ_s versus cell density data shown in Fig. 7.6A and g versus cell density data shown in Fig. 7.6B. In general, the results shown in Fig. 7.6 are similar to those in Fig. 7.5, although the data is a little noisier. For μ_s, the rate of change of 10.0 cm^{-1} per 1×10^6 cells/ml (Fig. 7.6A) is very similar to the 10.7 cm^{-1} per 1×10^6 cells/ml seen in Fig. 7.5B; however, the offset (15.1 versus 7 cm^{-1}) does differ a bit. However, this difference between the 2 measurements was within the resolution of the method, which for μ_s (at this g value) is 14 cm^{-1}. In terms of g (Fig. 7.6B), the results are again similar to those in Fig. 7.5C but there were a couple of outliers. These outliers were likely caused by a faulty calibration, where too a weak signal will artificially increase ρ, thereby decreasing g, without much effect in μs as was the case here. Excluding these 2 points (circled in black in Figs. 7.6A and B), the calculated regression coefficients had an offset of 0.900, with a slope of 0.0069 per 1×10^6 cells/ml, very similar to an offset and slope of 0.902 and 0.0017, respectively, that were measured in the gels from Fig. 7.5C. Statistically, the noise in the data was evident in that μ_s and cell density were correlated (R^2=0.65), but not highly correlated as earlier. On the other hand, g and cell density remained relatively uncorrelated (R^2= 0.32), but not totally uncorrelated as before.

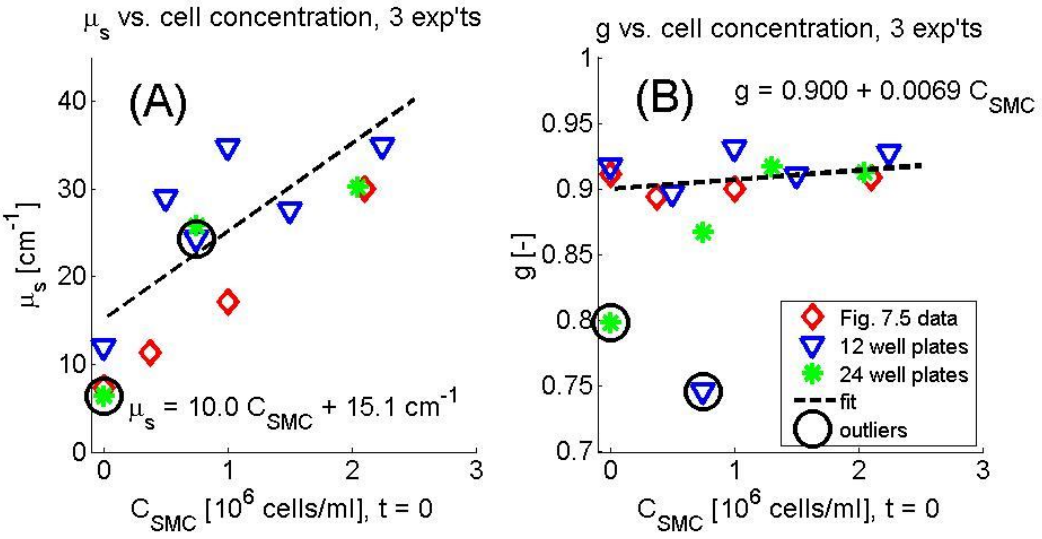

Fig. 7.6: Optical properties versus cell density for collagen gels from 3 set of experiments: the data in Fig. 7.5 and the extra sets in 12 and 24 well-plates. Linear regression coefficients are similar to those in Fig. 7.5B-C. Note there were 2 outliers in g (black circles) that were excluded from the regression calculation for both parameters.

Considering all the optical property data as a function of cell density shown in Fig. 7.6, we saw that μ_s increased with cell density while g remained unaffected. These results were observed consistently in 3 experiments, and suggest that as cell density increases, μ_s increases by approximately 10 cm^{-1} per 1×10^6 cells/ml cell density increase with an offset coming from collagen scattering of 15 cm^{-1}, while g remains unaffected by cell density at approximately 0.9.

Chapter 8: Non-destructive label-free monitoring of local smooth muscle cell remodeling of collagen gels using optical coherence tomography

This chapter was co-authored by: Monica T. Hinds, Ardalan Ardeshiri, Stephen R. Hanson, and Steven L. Jacques. A version of this chapter will soon be submitted to the journal Biomaterials.

8.1. Introduction

Cellular remodeling of the extracellular matrix (ECM) is a fundamental biological process that plays an important role in many physiological and pathological functions, including development [61], cell motility [62], aging [63], wound healing [64], atherosclerosis [65], tumorigenesis [66], fibrosis [67], as well as in many tissue engineering applications [68, 69, 96]. ECM remodeling involves assembling, degrading, and reorganizing ECM structures [70]. Critical to ECM remodeling is the activity of a family of enzymes called matrix metalloproteinases (MMPs), which degrade ECM structural proteins. MMP substrates include collagens, fibronectin, laminin, and proteoglycans [60]. Real-time information on ECM remodeling would improve understanding many of these physiological and pathological processes.

Currently, one common *in vitro* model of ECM remodeling is a 3D collagen I matrix populated by fibroblasts or smooth muscle cells (SMCs), in what is often referred to as a collagen gel [10]. Over time, these cells contract and remodel the collagen matrix, causing a decrease in the size of the gel in a process often referred to as either gel contraction or gel compaction [37]. MMP activity has been implicated as playing an important role in collagen gel remodeling [53, 54, 57].

Given the importance of ECM remodeling in many fields of biomedicine, there has been a search for methods that could monitor the process in real-time both quantitatively and non-destructively [22]. One promising technology that was recently proposed for imaging engineered tissues is optical coherence tomography (OCT) [7]. OCT, which measures coherent light backscattered from tissues, has several technological advantages for imaging collagen gels and other engineered tissues, including an axial resolution <10 μm and an ability to image tissues up to a 2 mm depth at video-rate imaging speeds [22]. Importantly, contrast in OCT images is based on endogenous refractive index mismatches between structures in the imaged sample, and thus no labels need to be added to the sample. OCT data also contain information of the scattering properties of structures within the imaged sample, and recently our group developed an algorithm that fits OCT signals to a theoretical model and evaluates the optical scattering properties of the imaged sample in local nanoliter volumes [8]. Measuring the optical properties from OCT images of collagen gels showed that over a 5 day period, the reflectivity more than doubled from its day 1 values, corresponding to a decrease in the scattering anisotropy [76]. We hypothesized that matrix remodeling, specifically MMP activity, was responsible for the reflectivity increase.

In this paper, OCT was used to show that collagen remodeling significantly contributes to the increase in reflectivity through a decrease in the scattering anisotropy. Specifically, SMC-populated collagen gels were treated with doxycycline (a non-specific MMP inhibitor), which impeded the decrease in scattering anisotropy over 5 days relative to the increase measured in untreated gels. Additionally, day 1 acellular collagen gels were treated with collagenase 2 (MMP-8) for 3 hours, which induced a partial decrease in

scattering anisotropy. We propose that the mechanism by which reflectivity is increased is that MMPs break down local collagen fibrils into small fragments, and these small fragments scatter light more isotropically, which increases the fraction of light backscattered towards the lens, thereby increasing the measured reflectivity.

8.2. Theory

The theory of light propagation in low-coherence imaging systems used in this paper was derived from the inverse Monte Carlo method [8]. For a homogeneous turbid medium characterized by scattering coefficient μ_s, anisotropy factor g, and absorption coefficient μ_a, the depth-dependent signal R(z) can be described as an exponential decay:

$$R(z) = \rho e^{(-\mu z)} \tag{8.1}$$

with reflectivity ρ and attenuation μ. Specifically,

$$\rho = \mu_s b(g) \Delta z \,, \tag{8.2}$$

and

$$\mu = 2G(\mu_s a(g) + \mu_a), \tag{8.3}$$

where Δz is the axial resolution and G is a geometry factor accounting for the extra pathlength caused by off-axis propagation, which can be approximated by $1/\cos(\sin^{-1}(\mathrm{NA}))$. The parameter b(g) represents the fraction of light backscattered at the focus towards the objective lens. As the scattering particles decrease in size, the scattering anisotropy of the sample decreases, which results in increases in b(g) and hence the reflectivity. The term a(g) describes the fraction of light scattered at such small polar angles that it cannot be distinguished from the unscattered light. For highly anisotropic scattering media, a(g) has the effect of reducing the measured attenuation in the OCT signal. Note this model requires calibrating the OCT signal (in arbitrary units) into dimensionless units of reflectivity ρ. Moreover, this model requires implementation of focus-tracking (or quasi-focus-tracking) conditions during OCT imaging.

8.3. Materials and Methods

8.3.A. Cell culture

All cell culture materials were purchased from GIBCO unless otherwise stated. Experiments involving cells used primary SMCs (passage 4-5) isolated from a single baboon carotid artery by enzymatic digestion [49]. SMCs were fed with SMC growth medium (SGM), consisting of minimal essential medium (MEM) supplemented with 10 % fetal bovine serum, 1 % L-glutamine, and 1 % penicillin-streptomycin.

8.3.B. Collagen gel preparation

Soluble calf skin collagen (MP Biomedicals, part # 150026) was dissolved in 0.02 N acetic acid at a concentration of 4 mg/ml. The collagen (1.625 ml, pH = 2.5) was mixed with 0.406 ml 5× MEM and 0.260 ml 0.2 M NaOH (Sigma), with additional 10 μl drops of NaOH solution added until the pH was neutral. Immediately thereafter, 1 ml SGM containing 3.25×10^6 SMCs was added to the collagen suspension, resulting in a Day 0 cell concentration of 1×10^6 cells/ml. The collagen suspension was aliquotted as three disc-shaped 1 ml samples in a 12 well plate (Corning) and thermally gelled for 1 hr at 37°; thereafter, 1 ml SGM was layered on top of each gel. After 24 hr, the gels were detached from the wells with a spatula and allowed to further compact. The gels were fed 1 ml SGM every 2 days. At each of the imaging times (days 1 and 5), 3 gels were removed from their wells, and imaged by OCT.

8.3.C. OCT imaging and image processing

The time-domain OCT setup used in this paper was previously described [92]. Briefly, a broadband light source operating at 1310 nm (B&W Tech) with a 100 nm bandwidth (full-width at half maximum) was coupled into a fiber-based Michelson interferometer. A rapid scanning optical delay line [81] varied the delay in the reference arm; a 10× microscope objective (Newport), mounted on a piezo-driven lens mount

(Piezosystems Jena), focused the light on the sample. The interference signal between the backreflected light from the sample and reference arms was measured using an InGaAs photodiode (New Focus). The OCT system was controlled through a data acquisition card (National Instruments) using software written in LabVIEW (National Instruments).

Datasets of 175×150×1024 pixels (xyz) representing 350×300×1000 μm were acquired from each collagen gel at a single site. For each collagen gel, image acquisition was performed 11 times at a single site, with the piezo-driven lens mount shifting the lens towards the gel by 40 μm in each successive dataset. Thus, in each of the eleven 3D datasets, a different depth range was in focus. The depth regions that were in focus from each of the (eleven) 3D datasets were stitched together to form one quasi-focus-tracked 3D dataset per sample. Acquisition of the 11 datasets took 50 minutes. During OCT imaging, the sample was mounted in a 35 mm Petri dish while immersed in PBS at room temperature to maintain hydration.

8.3.D. OCT image processing algorithm

A single, Matlab-based algorithm, organized in separate modular steps, was used to evaluate optical properties from all the data. Details of this algorithm were described previously [76]. Briefly, the regions in focus from each of the eleven 3D datasets were stitched together. Next, the pixels of the 3D image of the gel were adjusted axially along z to bring the gel surface to a constant z position, i.e., the gel was flattened. The 3D dataset was then subdivided into 10×10 regions of interest (ROIs) along x and y. Along z, the ROIs were truncated to cover depths spanning 150-400 μm. For each ROI, the signal was converted into reflectivity units by calibrating against the signal from a phantom with known optical properties. This calibration dataset (polystyrene microspheres suspended in an agarose gel) was imaged and processed before all other samples. The fitted reflectivity from each ROI in the calibration phantom was used to calibrate the signal from the corresponding (x, y) position in the imaged collagen gels, to account for differences in power delivered to the sample between the center of the

objective lens and the periphery that result from laterally scanning the beam. Finally, the natural log of the averaged calibrated depth-dependent signal $\left[\ln\left(\overline{R}_{ROI}(z)\right)\right]$ was fit to Eq. 8.1, yielding one (μ, ρ) pair for each ROI. In this OCT experiment, the algorithm overestimated both μ and ρ by 10-15%, and fits from individual ROIs had an intra-ROI coefficient of variation of <5 % for μ and 10 % for ρ [76].

8.3.E. MMP inhibition in SMC gels

To show that MMP activity was necessary for the observed changes in optical properties, SMC collagen gels were prepared according to the protocol in Section 8.3.B, with the addition of either 200 or 450 μM doxycycline [55]. Doxycycline is a tetracycline derivative that is also a non-specific MMP-inhibitor [73] shown to prevent remodeling of collagen gels populated with fibroblasts [74] as well as SMCs [55]. Macroscopic remodeling was monitored in these gels, with details provided in the data supplement. The gels were imaged by OCT at day 5 and their optical properties were quantified.

8.3.F. Collagenase treatment of acellular gels

To show MMPs alone were sufficient to change the optical properties of collagen gels, acellular collagen gels were prepared and treated with collagenase 2 (MMP-8), since MMP-8 has been previously shown to degrade collagen under cell-free conditions [97]. Specifically, after the gels were detached at 24 hr, the gels were washed 3 times in PBS and incubated with 0.5 ml MEM containing either 0.5 or 1 unit/ml collagenase 2 (Sigma) for 3 hr at 37°. Thereafter, collagenase activity was blocked with 1 ml SGM and the gels were imaged by OCT with their optical properties evaluated.

8.3.G. Confocal mosaic imaging and analysis

Confocal mosaicing [98] is a new imaging technique in which a number of adjacent *en face* confocal images are stitched together laterally, resulting in an image that

covers large areas (~cm^2) of tissue at sub-micron resolution. Recent work on confocal mosaics of excised tumors from Mohs surgery [95, 99] have shown that the reflectance and fluorescence confocal images from a tissue stained with a cellular dye represent the matrix and cells, respectively. Four groups of collagen gels (5 gels per group) were imaged by confocal mosaicing – day 1 gels, day 5 untreated (dox-) gels, 200 μM dox+ day 5 gels, and 450 μM dox+ day 5 gels. Immediately following OCT imaging, the imaged collagen gels were washed in PBS and stained with eosin for 30 sec. Reflectance and fluorescence confocal mosaics were acquired using a modified VivaScope (Lucid, Inc.) at an imaging depth of approximately 20 μm from the (bottom) gel surface. Both reflectance and fluorescence images were captured at 8-bit resolution under the same detector setting to enable direct comparisons between the different gels. Each *en face* confocal image (tile) in the mosaic was composed of 1000×1000 pixels, which represented 500×500 μm. The number of tiles in each mosaic was approximately 20×20 (1×1 cm), though the exact numbers were tailored to the match the size of the imaged collagen gel.

The mosaic images were analyzed both visually and quantitatively. Specifically, the regions in each mosaic that corresponded to the gel were delineated with the mouse, creating a binary mask of the gel within the image. Using this mask, the probability density functions (PDFs) of reflectance pixel intensities inside the gel were determined within the 256 discrete intensity values. These pixel intensity values from the confocal mosaics are in arbitrary reflectance units.

8.3.H. Data analysis and statistics

All the OCT collagen gel experiments presented in this paper were repeated 3 times, with 3 gel samples imaged each time, resulting in n=9 samples imaged in total from each collagen gel condition. The data from each imaged collagen gel resulted in ~40-50 ROIs that met the optical property fitting algorithm criteria. Each linear fit of ROI data resulted in a (μ, ρ) pair. The distribution of (μ, ρ) data were grouped either by sample or by gel type. For each of these distributions, the PDFs f(μ) and f(ρ) were also

computed by binning $\log_{10}(\mu)$ and $\log_{10}(\rho)$ values from an individual group into histograms made of Gaussian shaped kernels. Additionally, by treating attenuation μ and reflectivity ρ as statistically independent random variables, a joint PDF was computed by $f(\mu, \rho) = f(\mu)f(\rho)$. The (μ, ρ) values from the peak of the joint PDFs were used as the representative values of the group and mapped back to the corresponding (μ_s, g). When calculating statistics, the (μ_s, g) values corresponding to the peak of the PDF of each collagen gel were used. A one-way ANOVA was used to calculate statistical significance in multiple distribution comparisons, using a Boneferroni *post hoc* to determine P values. Additional statistics calculated using $\log_{10}(\rho)$ and $\log_{10}(\mu)$ are also reported for completeness.

8.4. Results

8.4.A. Remodeling increases reflectance intensity in en face confocal mosaics

Confocal mosaics that imaged ~1 cm^2 of collagen gel area at a ~20 μm depth were acquired to assess the spatial uniformity of the gels. The reflectance signal from each gel, representing the matrix, was false-colored in green, while the eosin fluorescence that represented the cytoplasm was false-colored in red. Fig. 8.1A-B shows a representative (*en face*) 0.6×0.6 cm confocal mosaic and a mosaic tile at higher magnification (500×500 μm) for the day 1 gels; Fig. 8.1C-D shows 0.6×0.6 cm mosaic and tile for the day 5 (dox-) gels. The tiles are highlighted in a dotted cyan line in the corresponding mosaic. Because the reflectance signal was so weak, the images displayed were digitally boosted by a factor of 3. Note that over a range of millimeters in x-y, the gels had an irregular surface with variations in z that measured >20 μm, which explains the patchy appearance of the mosaics in Figs. 8.1A, C.

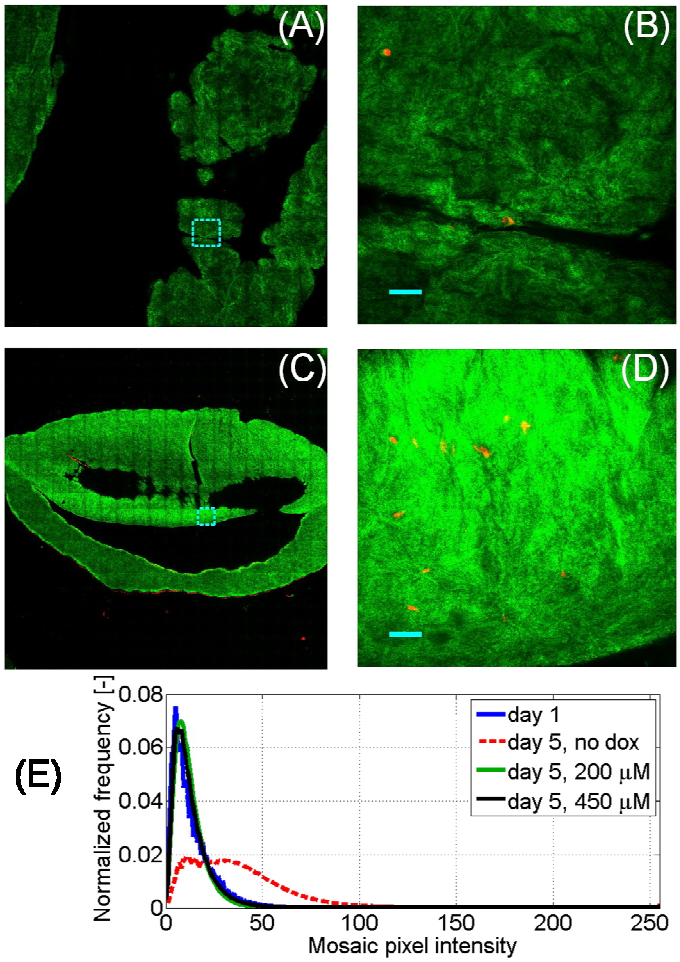

Fig. 8.1: Representative confocal mosaics of collagen gels, with the reflectance signal (green) representing collagen and eosin fluorescence signal (red) representing cell cytoplasm. (A, C) Representative 0.6 x 0.6 cm mosaics of day 1 and day 5 collagen-SMC gels, respectively, with representative 500 x 500 μm tiles shown at higher magnification in (B, D), respectively. Note that in (A-D) the reflectance signal was digitally boosted 3-fold. (E) Statistical distribution of pixel intensities of the collagen-SMC gels outlined in the reflectance mosaics that quantify the reflectance increase in the day 5, dox- gels. Tile shown in (B) and (D) represent 500 x 500 μm, are outlined in cyan in (A) and (C), respectively. (B, D): Bar = 50 μm.

In comparing the mosaics from the day 1 gels and the day 5 (dox-) gels, the overall reflectance of the day 1 gels (Fig. 8.1A-B) was very weak, while the reflectance from the day 5 gels was much stronger. To quantify these differences, the areas of each

mosaic that represented the gels were delineated, creating a binary mask that represented the gels. The pixel intensity distributions in the (raw) reflectance images were binned, and are plotted in Fig. 8.1E. It can be seen that most of the pixels from the day 1 gels were found between 0 and 30 a.u. on an 8-bit 0-255 scale, while most of the pixels in the day 5 gels were found between 0 and 80 a.u.

The differences between the day 1 and day 5 gels (Fig. 8.1), illustrate how collagen gel development and remodeling change the optical properties and thus increase the reflectance. But while the images in Fig. 8.1 were acquired at a single plane, the OCT data presented below were acquired over entire 3D volumes. The remainder of the paper shows a more detailed, depth-resolved, analysis of the reflectivity of collagen gels at a different wavelength (1310 versus 532 nm).

8.4.B. Collagen gels exhibit an increase in reflectivity over time

The optical properties of SMC and acellular collagen gels at day 1 and day 5 are plotted in Fig. 8.2A. The optical data is displayed in its entirety as a scatter plot on a grid of iso-μ_s and iso-g lines that represent theoretical values. Each datum point represents the (μ, ρ) values from the peak of the joint PDF of a single gel. As can be seen in Fig. 8.2A, the reflectivity of the day 5 SMC gels is roughly 10-fold that of the other 3 groups, with little change in attenuation. These changes correspond to a decrease in scattering anisotropy from 0.91 to 0.46 with little change in the scattering coefficient. Mapping the PDF peaks back to (μ_s, g) space and comparing the 4 gel groups statistically, there was a significant difference in both scattering anisotropy and reflectivity between the day 5 SMC gels and the 3 other gel conditions ($P<10^{-7}$). In contrast, both attenuation and scattering coefficient of the gel groups did not significantly differ. In addition, the joint PDFs of the 4 collagen gel groups in Fig. 8.2A are plotted on a grid in Fig. 8.2B, showing there was slightly more statistical variation in the acellular gels than in the SMC gels.

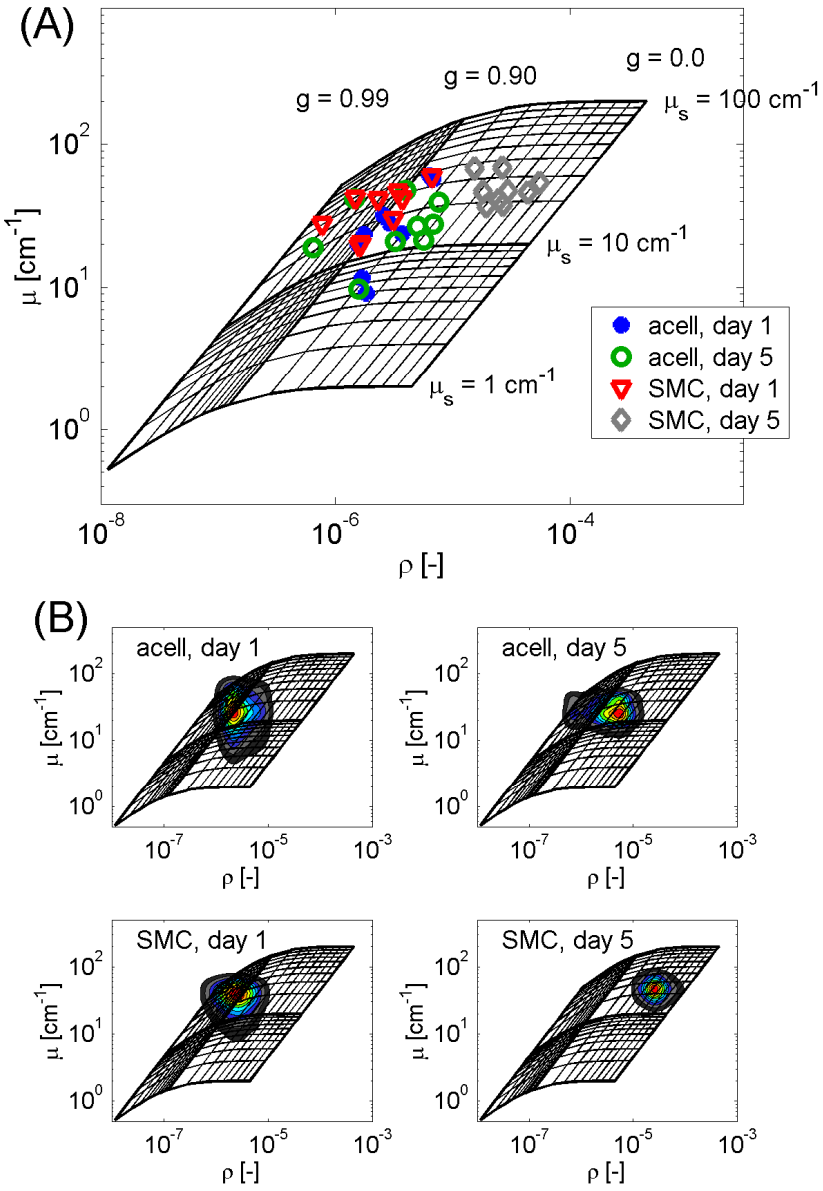

Fig. 8.2: Optical properties of acellular and collagen–SMC gels. (A) Scatter plot of the (μ, ρ) values from the peak of the joint PDF of each imaged sample, displayed on a log-log scale and superimposed on a grid that maps theoretical iso-μ_s and iso-g lines to the experimental conditions. (B) Joint probability density functions of the optical properties of the collagen-SMC gels and calibration spheres, displayed as a color map and superimposed on the grid.

8.4.C. Doxycycline mitigates increase in reflectivity in remodeling collagen gels

To assess the role MMPs play in the optical properties of collagen gels, SMC gels were treated with 2 different doses of the non-specific MMP inhibitor doxycycline and were imaged at 5 days by both confocal mosaics (n=5) and OCT (n=9), and the optical properties were quantified from the OCT data. A photo of the SMC gels treated with (dox+) and without (dox-) doxycycline is shown in Fig. 8.3A. It can be clearly seen that the dox- and dox+ gels look different. The 450 μM dox+ gels look flat with uniform thickness, have a large diameter, and appear more transparent, resembling unremodeled day 1 gels. However, the dox- gels are shaped as a bi-concave disc, with a smaller diameter relative to day 0, and a cloudier (i.e., more reflective) appearance. The 200 μM dox+ gels appear to be partially remodeled, in between the dox- and 450 μM dox+ gels. Macroscopic measurements of remodeling and confocal mosaic images from the dox+ gels are found in the data supplement.

Fig. 8.3B shows the reflectivity of day 5 dox+ and dox- gels. Since no significant differences in μ_s were observed between the various gel groups, only information on g is presented. For comparison, the g values from the day 1 gels are also plotted. The anisotropy of the dox- gels was in between the optical properties of the day 1 and day 5 dox- gels. At 5 days, the differences in the anisotropy between the dox- and dox+ were significant for both the 450 μM and 200 μM doses ($P<0.01$ and $P<0.05$, respectively). Similarly, the differences in $\log_{10}(\rho)$ between the day 5 dox- and 450 μM and 200 μM dox+ gels were $P<0.001$ and $P<0.01$, respectively.

8.4.D. Collagenase activity increases reflectivity of acellular gels

Finally, to show that MMP activity is sufficient to cause an increase in reflectivity, multiple acellular collagen gels were treated with MMP-8 for 3 hr, imaged by OCT, and had their optical properties evaluated. Macroscopically, no signs of remodeling were evident as the treated gel and untreated gels looked very similar. The mean anisotropies from the treated and untreated day 1 acellular gels are plotted in Fig.

8.4. These data show that in 3 hours, collagenase activity alone induced a significant decrease in the scattering anisotropy of acellular gels, with $P<10^{-5}$ between the untreated and either treated groups. The increase in reflectivity of the treated gels was significantly higher ($P<0.05$) than the untreated group.

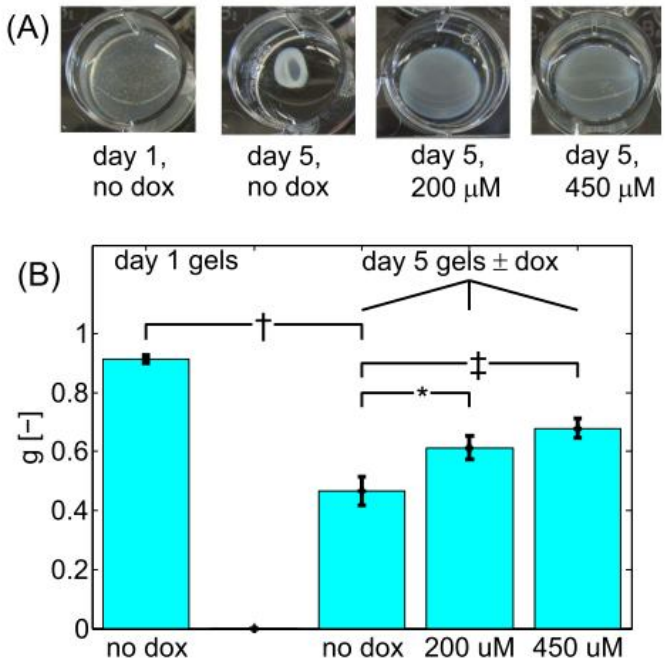

Fig. 8.3: Effect of doxycycline dosage on collagen-SMC gels. (A) Photos of collagen-SMC gels in 12-well plates with and without doxycycline treatment. (B) Scattering anisotropy of collagen gels. All P-values were calculated against the day 5 dox- gels. Error bars represent the standard error of the means. †: $P<10^{-8}$; *: $P<0.05$; ‡: $P<0.01$.

8.5. Discussion

In this paper, we showed that OCT is capable of measuring and quantifying changes in optical scattering properties caused by SMC remodeling of collagen fibrils. By measuring these optical properties from OCT data, we showed that from day 1 to day 5, there was a 10-fold increase in reflectivity ρ with no change in attenuation μ, which corresponds to a decrease in anisotropy g from 0.91 to 0.46, with little change to scattering coefficient μ_s (Fig. 8.2). Blocking MMP activity in the gels by treating them

with doxycycline for 5 days impeded collagen gel remodeling macroscopically (Fig. 8.3A, supplementary Fig. 8.1) and the corresponding decrease in scattering anisotropy (Fig. 8.3B). The effect that the presence (or absence) of MMPs had on collagen reflectance could be seen in the confocal mosaics (Fig. 8.1, supplementary Fig. 8.2), where the collagen matrix in the day 5 dox- gels had a much higher reflectance signal than the day 1 gels and both doses of the day 5 dox+ gels. Treating acellular collagen gels with MMP-8 for 3 hr managed to partially mimic the increase in reflectivity that occurs over 5 days (Fig. 8.4). Taken together, we believe the data presented here shows that (A) a relationship exists between MMP activity and the optical properties of collagen gels, and (B) that measuring optical properties from OCT data provides an indirect assessment of remodeling in local nanoliter volumes.

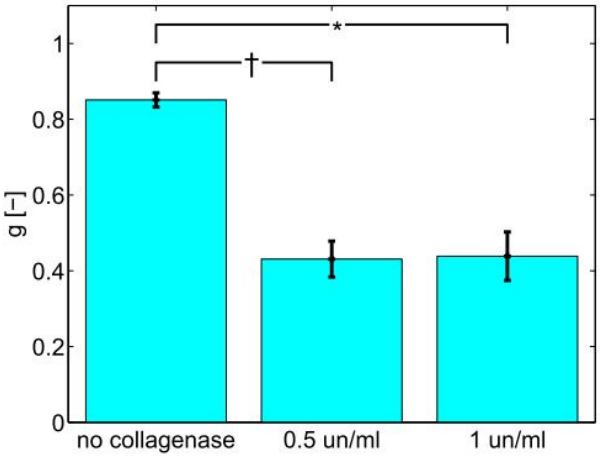

Fig. 8.4: Effect of treating day 1 acellular gels for 3 hr with collagenase 2 on the reflectivity measured from the OCT data. Error bars represent the standard error of the means. Both collagenase treated gels differed significantly from untreated gels ($P<10^{-5}$).

Using OCT to measure the optical properties is advantageous in terms of characterizing collagen gels, and more broadly engineered tissues, for multiple reasons. The optical scattering properties of a sample, particularly the scattering phase function $P(\theta)$ and scattering anisotropy g, are very sensitive to the molecular microstructure of the sample [11]. The decrease in scattering anisotropy between the day 1 and day 5 gels illustrates that the optical properties are sensitive to ECM degradation (among other

things). Moreover, measuring optical properties is non-destructive, allowing for repeated measurements on the same sites and on the same sample. This OCT technique is based on endogenous contrast between the collagen, the cells, and the surrounding medium, making it label-free, which reduces both the costs and complexity associated with adding exogenous fluorescent labels. As a fiber-based technology, OCT probes can be readily integrated into the incubator for continuous, time-lapse monitoring of construct uniformity. Finally, since the sample arm of the OCT system is essentially a confocal microscope, an OCT system can be designed to acquire mosaics of data (analogous to confocal mosaics in Fig. 8.1, supplementary Fig. 8.2), that cover centimeters of area and millimeters of depth, compared to the ~100 μm depth limit on confocal mosaic imaging. Such an instrument, that can continuously and non-destructively monitor milliliter volumes of a sample at micron resolution and detect changes in the ECM in nanoliter volumes without any exogenous labels, can prove to be a powerful tool for surveying the spatial uniformity of engineered tissues.

Recently, we demonstrated that over 5 days SMC remodeling of collagen gels decreased both anisotropy g and scattering coefficient μ_s, thereby causing the reflectivity to double and the attenuation to remain the same [76]. Moreover, the measured reflectivity statistically followed a bimodal distribution, with a sizeable subpopulation of data points with 10-fold reflectivity relative to that from the first 24 hr. Although the trends are similar, this earlier data contrasts with Fig. 8.2, where nearly all the day 5 reflectivity data was 10-fold higher than the day 1 reflectivity data. Subsequent experiments showed that this discrepancy was caused both by the cell source (i.e., from different baboons) and the serum lot. Moreover, the gel compaction time dynamics from the previous study also contrasted with those in the present study: Earlier, the gel volume reduced in incremental steps every day, while in this study most of the compaction happened between days 1 and 2.

In trying to dissect the optical property data and identify what caused these observed decreases in scattering anisotropy (increases in reflectivity), 4 possibilities were hypothesized: increased collagen density, increased cell density, SMC contraction, and

ECM remodeling. In the SMC gels, there was no correlation between anisotropy and either collagen density or cell density [76]. To assess whether SMC contraction, i.e., a change in cell morphology, caused the measured increase in reflectivity, collagen gels were prepared and seeded with endothelial cells (ECs) instead of SMCs. The ECs and SMCs were determined to have different morphologies in 3D collagen gels by F-actin staining (data not shown). At day 1, the EC gels and SMC gels differed in μ_s ($P<0.05$), but not in g ($P>0.05$) [100]. Since the primary changes in the remodeling of SMC gels were in g, the EC data suggests such changes were not caused by a change in cell shape, which further supports the hypothesis that ECM remodeling caused the changes in the optical properties of the collagen gels.

Mie theory [11], which calculates the angular distribution of light energy scattered off a sphere, can be used to interpret the optical properties of the collagen gels. Mie theory states that in general, as the sphere diameter increases, light is scattered more anisotropically, that is, mostly in the forward direction ($g \rightarrow 1$); conversely, as the sphere diameter decreases, light is scattered more isotropically, that is, relatively equally in all directions ($g \rightarrow 0$). The OCT signal depends on light backscattered from the sample, specifically, the fraction of light scattered back towards the lens relative to the total scattered energy. The fraction of light scattered in the backwards direction increases as the scattering anisotropy decreases, forming an inverse relationship between scattering anisotropy and reflectivity, as has been described in our theoretical model [8]. Applying these principles to collagen gels, scattering by the collagen fibril network is intrinsically very forward-directed, as shown by the high scattering anisotropy/low reflectivity measured from these samples (Figs. 8.2, 8.4). Proteolytic degradation of the collagen matrix by local MMP activity breaks down the fibrillar collagen network into small fibril fragments. These fibril fragments constitute a dense collection of local isotropic scatterers that would scatter more light back to the objective lens, thereby increasing the reflectivity.

In trying to understand SMC remodeling of collagen matrices, some insight can be obtained from cell biology studies on collagen gels seeded with fibroblasts, which

have been better documented in the literature [53, 54, 57, 58]. When seeded in a collagen gel, fibroblasts assume a differentiated myofibroblast phenotype, expressing both α-smooth muscle actin and smooth muscle heavy myosin chains [54, 101]. Moreover, these fibroblasts contract and pull on the collagen fibrils causing gel compaction, as well as express and activate MMPs, thereby resembling SMCs both structurally and functionally. Collagen gels seeded with fibroblasts prepared in our lab showed both similar macroscopic remodeling and a similar decrease in scattering anisotropy/ increase in reflectivity over 5 days (data not shown). Additionally, collagen gels seeded with ECs, a cell type that generates little secreted MMP activity in 3D collagen matrices [102], did not produce comparable remodeling at 5 days, neither macroscopically nor microscopically [100]. Considering the fibroblast gels as positive controls and the EC gels as negative controls further confirms our hypothesis that ECM remodeling is causing the measured changes in optical properties.

In general, there are 2 types of remodeling – mechanical remodeling, in which the collagen matrix is pressed down and fluid is expelled, and biochemical remodeling, which involves proteolytic enzymes such as MMPs breaking down collagen [53, 59]. Mechanical remodeling (i.e., gel compaction) can be seen even in the absence of cells, for example on the outside periphery of the gels, where the wall of the well exerts support that causes the outer periphery to be more opaque than the center. Biochemical remodeling, i.e., proteolytic MMP activity, is determined by local agonists like PDGF and TGF-β that are found in serum and whose function is to regulate such activity [58]. Moreover, biochemical remodeling can be further subdivided into global remodeling caused by collagenases and gelatinases that were secreted into the extracellular space, and local remodeling in the pericellular space by membrane-tethered MMPs (MT-MMPs) [71].

Several studies measuring MMP activity in SMC-gels using gelatin zymography showed that secreted MMPs, specifically MMP-2 (gelatinase A), play a critical role in matrix remodeling [50, 55]. However, both these studies (and ours) used serum-containing media, and serum contains proteins such as α_2-macroglobulin that are very

effective at blocking proteolytic activity [72]. Unlike the secreted MMPs, the key membrane-bound MMP, MT1-MMP (MMP-14) is activated by mechanisms that are independent of the activation cascade that regulates the secreted MMPs [71]. Thus, the microenvironment within the collagen gel in which MMPs are acting is complex, and further work is needed to identify the influence each of these MMPs has on the optical properties. One possible way to assess if the MMPs are acting globally or locally is to prepare collagen gels in which all the SMCs are plated on one side, which would concentrate the changes in scattering anisotropy to the SMC side of the gels. These experiments are currently ongoing in our lab.

It is worth noting that our primary objective in this paper was to determine what role MMPs play on optical scattering within collagen gels, and in some ways both the doxycycline and collagenase experiments were intended to serve as a proof-of-principle. Blocking MMP activity with doxycycline impeded the decrease in scattering anisotropy (Fig. 8.3B) and impeded gel compaction (supplementary Fig. 8.1, [55]), but did not eliminate it. Similarly, treating acellular gels with collagenase partially mimicked the increase in reflectivity, but did not reproduce it in full. In both the doxycycline and collagenase experiments, the dose response of anisotropy was nonlinear. Thus, it is likely that other mechanisms contribute to the measured changes in optical properties.

Within this context, it is important to distinguish between cell biology applications of collagen gels, in which the goal is to identify active compounds and elucidate cellular pathways that are involved with remodeling, and tissue-engineering applications, in which the goal is to replace or regenerate tissue. In cell-biology applications, the exact contents of the growth medium need to be controlled to avoid cross-talk with other agents and/or pathways, and thus serum, which introduces a great deal of variability into the growth medium, is often excluded. In tissue-engineering applications, where the focus is primarily on the overall cell density, localization, and functions, inclusion of serum in the growth medium is often required to achieve proper cell growth and function. Nonetheless, information on the collagen microstructure is important for both cell biology and tissue-engineering applications, and thus the

technique of measuring optical properties from OCT images is applicable to both. Moreover, adapting the experimental conditions for cell biology applications, i.e., elucidating the role of mechanical tension or agonists like PDGF and TGF-β on the collagen microstructure, would be trivial.

8.6. Conclusion

In this study, OCT was used to quantitatively monitor ECM remodeling in SMC-seeded collagen gels from day 1 to day 5 by measuring the optical properties from OCT data. Over 5 days, the reflectivity of the SMC gels decreased the scattering anisotropy from 0.9 to 0.45 while the scattering coefficient stayed the same, corresponding to a 10-fold increase in reflectivity with no change in attenuation (Fig. 8.2). To assess the role MMPs played in the change in optical properties, additional sets of SMC gels were prepared and treated with doxycycline, a non-specific MMP inhibitor, which impeded remodeling macroscopically over 5 days (Fig. 8.3A, supplementary Fig. 8.1). The optical properties of the day 5 dox+ gels did not show the decrease in anisotropy measured in the day 5 dox- gels, and the measured anisotropy values ranged between the day 1 and day 5 dox- gels (Fig. 8.3B). Confocal mosaicing visually confirmed the presence or absence of remodeling in the collagen gels, and the reflectance signal was substantially higher in the day 5 dox- gels than the unremodeled day 1 gels and dox+ gels (Fig. 8.1E). Finally, day 1 acellular gels were treated with MMP-8 (collagenase 2) for 3 hr, which resulted in a decrease in anisotropy that partially mimicked the decrease measured in SMC gels after 5 days of remodeling (Fig. 8.4). All in all, our data suggests that the activity of MMPs in SMC collagen gels degrades collagen fibrils into smaller fragments, and that OCT can visualize and quantify the entire process.

8.7. Data supplement

8.7.A. Methods: Gel compaction

Collagen gel remodeling was monitored macroscopically. Specifically, gel compaction was quantified over time, both in terms of volume and area reduction. Prior to OCT imaging, the volume of the gels was indirectly measured via the mass of the media in the well (1 ml SGM = 1 g ± 0.1%). The volume of a gel was then calculated by $V_{gel} = 2\ ml - V_{SGM}$, with the 2 ml coming from an initial gel volume of 1 ml gel that was fed with 1 ml SGM. Shortly after OCT imaging, digital photos of all the gels in the 12-well plates were taken, which allowed calculating the area reduction in each gel using software written in Matlab.

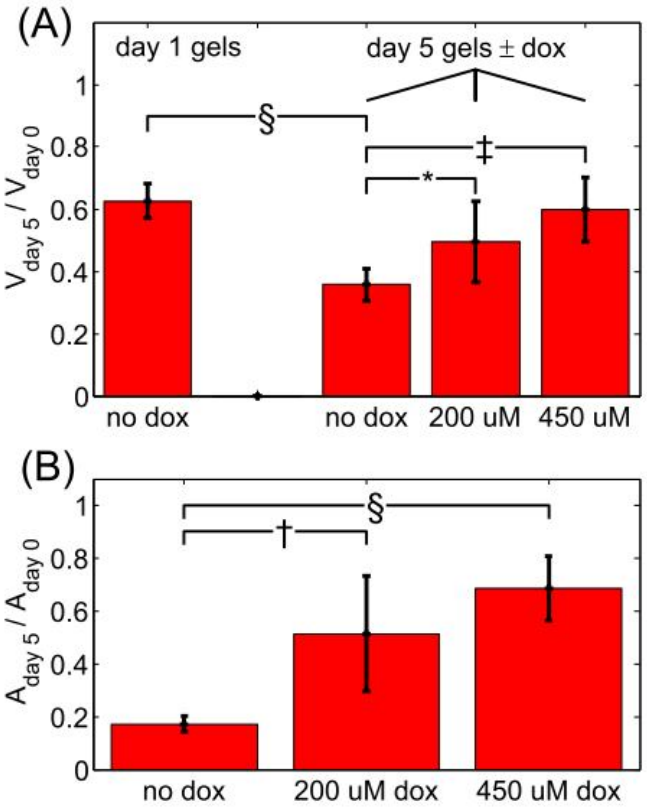

Fig. 8.S1: Macroscopic compaction in collagen gels calculated as a percent reduction in volume (A) and diameter (B). At day 0, the gel volume was 1 ml and the gel area was 4 cm^2. Error bars represent the standard deviation. *: $P<0.05$; †: $P<0.001$; ‡: $P<10^{-4}$, §: $P<10^{-5}$.

8.7.B. Results: Gel compaction

Supplementary Figs. 8.S1 A-B plot the reduction in gel volume and area for the SMC gels, respectively. Specifically, the day 1 SMC gels compacted to 63 % of their original volume, while the day 5 dox- gels compacted to 34 % ($P<10^{-5}$). Moreover, the area of the day 5 SMC gels reduced to 17 % of the original well area; note that the day 1 gels were attached until just before imaging and hence maintained their original area. Supplementary Fig. 8.S1 also shows that macroscopically, the 450 μM gels compacted to 68% of their original volume ($P<10^{-4}$ vs. dox- gels) and 76% of their original area ($P<10^{-5}$), while the 200 μM gels compacted to 55 % of the original volume ($P<0.05$ vs. dox- gels) and reduced to a 71% of the original area ($P<0.001$).

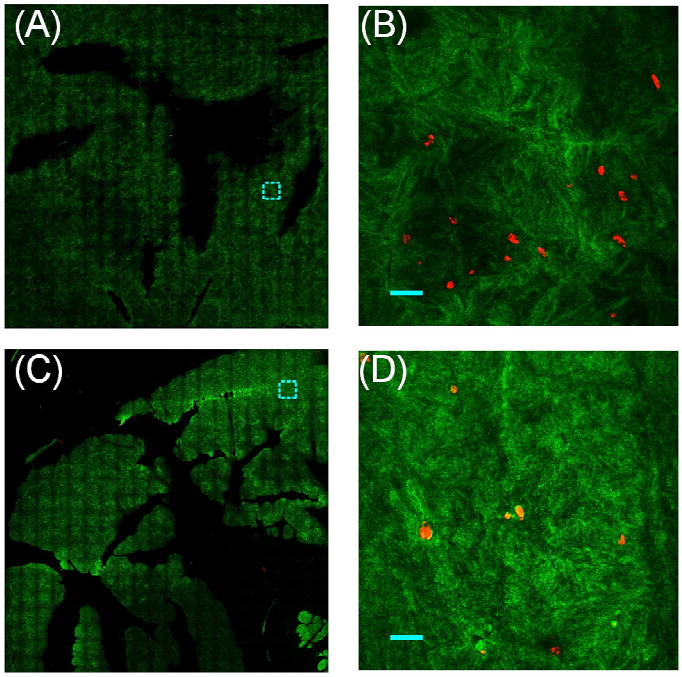

Fig. 8.S2: Confocal mosaics of day 5, dox+ gels, with the reflectance signal (matrix) false-colored green and the cells false-colored red. (A, C) Representative 1×1 cm mosaics of 200 μM and 450 μM dox+ gels, respectively, with representative 500×500 μm tiles shown at higher magnification in (B, D), respectively. Similar to Fig. 8.1, the reflectance signal was digitally boosted 3-fold. Note that for both doxycycline doses the reflectance signal from the matrix is weak, similar to day 1 gels (Fig. 8.1A and B).

8.7.C. Results: Confocal mosaics of dox+ collagen gels

Confocal mosaics of the dox+ gels are shown in supplementary Fig. 8.S2. Full mosaics that cover 1 x 1 cm of 200 and 450 μM dox+ gels are shown in supplementary Figs. 8.2A and C, respectively, with enlargements of the selected area that represent 500 x 500 μm in supplementary Figs. 8.S2B and D. Note that similar to Fig. 1A-D, the reflectance signal in supplementary Fig. 2 was digitally boosted by a factor of 3. The confocal mosaics showed that the reflectance intensity was much brighter in the day 5 dox- gels (Fig. 8.1C-D). Statistically, the distribution of pixel intensities in the day 5, dox+ gels was nearly identical to distribution from the day 1 gels (Fig. 8.1E).

Acknowledgements

The authors would like to thank Dan Gareau of the Department of Science and Engineering at OHSU for help aligning the VivaScope. Additionally, the authors would like to thank Fred Grinnell, Kate Phelps, and Miguel Miron of the Cell Biology Department at University of Texas-Southwestern Medical Center for helpful discussions on collagen gel remodeling. This study was funded in part by the National Institutes of Health grant R01-HL084013 (Jacques) and R01-HL095474 (Hanson).

Chapter 9: Depth-resolved analysis of how cell localization and remodeling affect the optical scattering properties of collagen gels

9.1. Introduction

Understanding the complex relationship between cell localization and extracellular matrix (ECM) remodeling is critical to successful tissue engineering [21]. Cell-matrix interactions regulate many cell functions [70] such as proliferation, contraction, and protein expression [61, 103]. Moreover, cell-matrix interactions affect, and are affected by, communication between cells in close proximity [70]. However, despite the critical role cell-matrix interactions play in many tissue engineering applications [21], the relationship between local cell density affects local cell-matrix interactions is poorly understood.

One of the most basic types of engineered tissues is the collagen gel [10], in which cells such as fibroblasts or smooth muscle cells (SMCs) are embedded inside a collagen I matrix. Collagen gels serve as a template for many types of engineered tissue, including vascular [104] and dermatological applications [105]. Over time, the cells remodel and contract the collagen matrix and thus collagen gels offer a simple model to study cell-matrix interactions.

One promising imaging modality for characterizing engineered tissues is optical coherence tomography (OCT) [7]. OCT uses low-coherence interferometry to achieve fine spatial resolution (~10 μm) with penetration depths up to 1 mm in turbid tissues [24]. As an optical technology, OCT is non-destructive, allowing for repeated measurements on the same site. Since the contrast mechanism in OCT is based on endogenous differences in refractive indices, no labels need to be added to the sample of interest.

Recently, our group developed a method for characterizing developing collagen gels by measuring their optical properties from OCT data [76]. Specifically, fitting the OCT signal to a theoretical model [8] provides an estimate of the attenuation μ and reflectivity ρ, which together can be mapped back to the optical scattering properties, namely, the scattering coefficient μ_s and anisotropy factor g. Using this technique, we recently showed a strong correlation between the scattering coefficient and cell density in unremodeled collagen gels [76], as well as a relationship between reflectivity and matrix remodeling, specifically matrix metalloproteinase (MMP) activity [106].

In this paper, we use this technique to assess the relationship between cell localization, matrix remodeling, and the optical properties. We compare the optical properties of acellular collagen gels to collagen gels with embedded SMCs and dual-sided collagen gels in which the SMCs were plated atop an acellular collagen gel and were thus only able to remodel one side of the gel. Our results showed that from day 1 to day 5, the embedded gels experienced a 10-fold increase in reflectivity with little change in attenuation, corresponding to a decrease in the scattering anisotropy. In the day 5 dual-sided gels, the optical properties of the SMC side showed a 5-fold increase in both attenuation and reflectivity. Analysis of the dual-sided gels at different depth ranges showed that optical properties varied with depth, with higher attenuation and reflectivity in the superficial regions than in the deeper regions; no such relationship was found to exist in the embedded gels. Our analysis showed that in the 300-400 μm depth range on the SMC-side, the optical properties were similar to those measured on the collagen side,

suggesting that most of the SMCs and MMP activity were localized above this depth. These observations were qualitatively confirmed by histology.

9.2. Theory

The theory of light propagation in low-coherence imaging systems used to process data has been described previously [8]. In a homogeneous turbid medium characterized by scattering coefficient μ_s, anisotropy factor g, absorption coefficient μ_a, refractive index n, the depth-dependent signal R(z) follows an exponential decay:

$$R(z) = \rho \exp(-\mu z) \tag{9.1}$$

with reflectivity ρ and attenuation μ. Moreover,

$$\rho = \mu_s b(g) \Delta z , \tag{9.2}$$

and

$$\mu = 2G(\mu_s a(g) + \mu_a), \tag{9.3}$$

where Δz is the axial resolution of the imaging system. G is a geometry factor that corrects for the extra pathlength that occurs with off-axis light propagation such that $G \approx 1/\cos(\sin^{-1}(NA))$, where NA is the numerical aperture of the imaging system. b(g) is a factor that represents the fraction of light backscattered towards the objective lens. As the scattering particles decrease in size, the scattering anisotropy of the sample decreases, which results in increases in b(g) and hence the reflectivity. a(g) describes the fraction of light scattered at such small polar angles that it cannot be distinguished from the unscattered light. In anisotropic media, a(g) has the effect of reducing the measured attenuation in the OCT signal.

This model requires that the OCT signal (measured in arbitrary units) be converted to dimensionless reflectivity units. This calibration, which can be done by comparing the fits from the sample to those from a phantom with known optical properties, is critical for the analyses described here. It is also worth noting that this theoretical model ignores defocusing effects and thus requires implementing focus-tracking (or quasi-focus-tracking) imaging conditions.

9.3. Materials and methods

9.3.A. Cell culture

All cell culture materials were purchased from GIBCO unless otherwise stated. Primary SMCs isolated from a single baboon carotid artery by enzymatic digestion [49] were used in all experiments involving cells presented in this paper. Collagen gels were prepared using passage 4-5 SMCs. SMCs were fed with SMC growth medium (SGM), consisting of minimal essential medium (MEM) supplemented with 10 % fetal bovine serum, 1 % L-glutamine, and 1 % penicillin-streptomycin.

9.3.B. Collagen gel preparation

The protocol used for collagen gel preparation has been previously described [106]. Briefly, soluble calf skin collagen (MP Biomedicals, part # 150026) was dissolved in 0.02 N acetic acid at a 4 mg/ml concentration. 1.625 ml collagen (pH = 2.5) was mixed with 0.406 ml 5× MEM and 0.260 ml 0.2 M NaOH (Sigma), titrating additional 10 μl drops of NaOH solution added until the pH was neutral. Immediately thereafter, 1 ml SGM was added to the collagen suspension. For gels with embedded SMCs, this 1 ml SGM contained SMCs at a concentration of 3.25×10^6 cells/ml, resulting in a Day 0 cell concentration of 1×10^6 cells/ml. The collagen suspension was aliquotted as three 1 ml samples in a 24 well plate (Corning) and thermally gelled for 1 hr at 37°. Thereafter, 1 ml SGM was added to each of the embedded gels.

To prepare acellular gels, the same exact protocol was used except the SGM added into the collagen-5× MEM-NaOH mixture contained no cells. To prepare dual-sided gels, acellular gels were prepared initially. At 1 hr, these 1 ml gels were fed with 1 ml SGM that contained 1×10^6 cells, matching the overall cell density in the embedded gels. The acellular gels filled the area of each well, and thus the cells were isolated at the top.

After 24 hr, the gels were detached from the wells with a spatula and allowed to further compact. Note that the SMC gels (embedded and dual-sided) were prepared in batches of 12, with 6 embedded gels and 6 dual-sided gels. During imaging on days 1 and 5, 3 gels from each type were removed from their wells, and imaged by OCT.

9.3.C. Gel contraction

When assessing gel contraction in the various collagen gel groups, both the reduction in gel area and volume were documented. The reduction in gel area was measured indirectly by weighing the media in each well, as previously described [106]. To assess the reduction in gel area, digital photographs of the gels were taken and analyzed. The outline of the gel was determined with a mouse, from which the corresponding area reduction was determined [106]. Both area and volume gel contraction measurements are expressed as a fraction of their initial (day 0) values.

9.3.D. OCT imaging and image processing

The OCT setup used in this paper was previously described [76]. Briefly, a broadband light source with a 1310 nm central wavelength and a 100 nm bandwidth (B&W Tech) was coupled into a fiber-based Michelson interferometer. A rapid scanning delay line [81] varied the optical delay in the reference arm; a 10× microscope objective (Newport), mounted on a piezo-driven lens mount (Piezosystems Jena), focused the light on the sample. The interference signal between the light backreflected from the sample and reference arms was measured using an InGaAs photodiode (New Focus). The OCT system was controlled through a data acquisition card (National Instruments) via software written in LabVIEW (National Instruments). The Hilbert transform, required to calculate the envelope of the interferometric OCT signal, was implemented in software post-acquisition using Matlab (Math Works).

Three-dimensional datasets of 175 × 150 × 1024 (xyz) pixels representing 350 × 300 × 1000 μm were acquired from each collagen gel. The embedded and acellular gels, presumed to be spatially uniform, were imaged at 1 site per gel, while the dual-sided gels were imaged at 1 site on the SMC side and 1 site on the collagen side. At each imaged site, image acquisition was repeated 11 times, with the piezo-driven lens mount shifting the lens towards the gel by 40 μm in each successive dataset. Thus, in each of the eleven 3D dataset, a different depth range was in focus, and data from these in-focus depth ranges were stitched together to form a single 3D dataset (per site) acquired at quasi-focus-tracking conditions. Acquisition of the 11 datasets took 50 minutes. During OCT imaging, the sample was mounted in a 35 mm Petri dish and covered with PBS to maintain hydration throughout imaging.

9.3.E. OCT image processing algorithm

A single, Matlab-based algorithm, organized in separate modular steps, was used to evaluate optical properties from all the data. More details on this algorithm were described by Levitz et al [76]. Briefly, the first step was stitching together the regions in focus from each of the eleven 3D datasets. Next, the data were aligned such that the superficial most pixel of the gel was found at the same z pixel across the entire 3D dataset. To do this, the user identified the superficial most pixel in each lateral position in 17 of the 150 acquired xz frames, which were then interpolated to cover the entire 3D range (along y). From these pixels, individual A-scans were shifted axially to align the image. The 3D dataset was then subdivided into 10×10 regions of interest (ROIs) along x and y. Along z, the ROIs were truncated to cover depths spanning 100-400 μm unless otherwise noted (in some analyses the optical properties from different depth ranges were compared). For each ROI, the signal was converted into reflectivity units by calibrating against fits from a phantom with known optical properties. Finally, the natural log of the averaged calibrated depth-dependent signal $\left[\ln\left(\bar{I}_{ROI}(z)\right)\right]$ was fit to Eq. 9.1, yielding one (μ, ρ) pair for each ROI.

To calibrate the OCT signal from the collagen gels, at each imaging session a light scattering phantom made of polystyrene spheres (0.6 μm) suspended in an agarose gel was also imaged. This calibration dataset was processed as described above except that it was processed before all the other samples from its imaging session. The reflectivity fitted at each ROI in the phantom was used to calibrate the signal from the corresponding (x, y) position in the imaged collagen gels. This accounted for differences in power delivered to the sample at different scan angles.

9.3.F. Histology

Following OCT imaging, collagen gels were fixed in 10% neutral buffered formalin (Richard Allan Scientific) overnight and then stored in 70% ethanol solution (Fisher Scientific) at 4° C. The samples were then passed for routine histological processing, in terms of paraffin-embedding, sectioning, and staining with hematoxylin and eosin (H&E). Ten 5 μm thick cross-sections of the collagen gel were cut parallel to the direction of OCT imaging, with 250 μm between successive sections. The H&E sections were imaged by phase-contrast microscopy (Nikkon) at 20×.

9.3.G. Data analysis and statistics

All collagen gel experiments presented here were repeated 3 times with 3 collagen gels per repetition, yielding a total of n=9 samples imaged from each collagen gel condition. The data from each imaged collagen gel resulted in ~70-80 ROIs that met the fitting algorithm's criteria. Each fit yielded a (μ, ρ) pair, and the data were grouped together either by sample or by gel condition. For each such distribution of (μ, ρ) values, the probability density functions (PDFs) $f(\mu)$ and $f(\rho)$ were calculated by binning individual $\log_{10}(\mu)$ and $\log_{10}(\rho)$ data into histograms made up of Gaussian-shaped kernels. Treating the variables μ and ρ as independent random variables, the joint PDF was determined by $f(\mu, \rho) = f(\mu)\, f(\rho)$.

The (μ, ρ) data was plotted as a scatter plot on a grid of iso-μ_s and iso-g contours that map experiment to theory. Given the large number of total data points, the (μ, ρ) values that correspond to the peaks from the joint PDFs from each individual sample were plotted for clarity, with the 2 sides of the dual-sided gels are plotted separately. Moreover, the (μ, ρ) values from the peak of the joint PDFs were used when mapping back to the corresponding (μ_s, g) values. To demonstrate the variance within the (μ, ρ) data, plots showing the joint PDF from a specific collagen gel group superimposed on a grid are also shown.

To statistically analyze our data, the (μ, ρ) values representing the peaks of the joint PDFs were used. A one-way ANOVA was used to calculate statistical significance in multiple distribution comparisons, using a Boneferroni *post hoc* to determine P values.

9.4. Results

9.4.A. Embedded and dual-sided collagen gels contract differently

Macroscopically, all gel types looked identical at day 1, since the gels were attached to the wells until being detached just prior to OCT imaging (Fig. 9.1A-B). After being detached, the embedded and dual-sided day 5 gels contracted differently, while the acellular day 5 gels did not contract at all. Specifically, the embedded gels contracted into a bi-concave disk shape. In the dual-sided gels, the area around the SMCs contracted on the SMC side but the collagen region beneath the SMCs did not contract, which caused the extra collagen on the side of the gel to fold over as a flap. Moreover, the concavity was localized to only one side, with the SMCs located in the central dip that was outlined by a ring of contracted collagen (Fig. 9.1B); the area inside this dip was imaged by OCT.

In addition to a different physical appearance on day 5 (Fig. 9.1B), gel contraction in the embedded and dual-sided gels was also assessed quantitatively via the reduction in gel area and volume. In measuring the area reduction in the gels (Fig. 9.1C), both the

area of the inner ring and outer flap were determined and compared to the area of the embedded gels. The inner ring, which represented the area of SMCs, contracted slightly more than the embedded gels, but there were no significant differences between these data. The outer flap, representing the collagen folding over, was significantly larger than the other 2 areas. In terms of volume, both embedded and dual-sided gels had similar volumes at day 1, presumably because both were still attached to their plastic wells. From day 1 to day 5, there was a significant reduction for both the embedded and dual-sided gels relative to their day 1 counterparts ($P<10^{-7}$). Additionally, the day 5 embedded gel contracted significantly more than the dual-sided gel, to 30% versus 50% of the original volume, respectively ($P<10^{-7}$).

9.4.B. SMCs can be visualized in OCT images of unremodeled collagen, but not in remodeled collagen

At day 1, the OCT images of the embedded gels showed a low signal background with bright spots that presumably represent cells or clusters of cells found uniformly spaced throughout the gels (Fig. 9.2A), while the acellular gels showed the low-signal, slowly varying background only (Fig. 9.2B). In contrast to the embedded and acellular gels, in the dual-sided day 1 gels, there was a thin high signal layer seen at the SMC side, while just beneath it the image resembled the acellular day 1 gels (Fig. 9.2C). Moreover, the collagen side of the dual-sided gels appeared identical to the acellular gels (Fig. 9.2D). From day 1 to day 5, both the embedded and dual-sided collagen underwent remodeling which changed their scattering properties (i.e., made them cloudier). In the OCT images, this translated to an increased signal/reflectivity in the embedded gels, which was absent from the acellular gels. In the dual sided gels, the collagen side remained unremodeled and had similar image features to day 1, as well as the acellular gels. The SMC-side of the dual-sided gels showed a signal-rich superficial region that strongly attenuated with depth. In both the day 5 embedded gels and the SMC side of the day 5 dual-sided gels, identifying structures such as cells unfeasible. Note that images of the outer flap of the dual-sided gels were of similar appearance and reflectivity to the collagen side of the dual sided gels (data not shown).

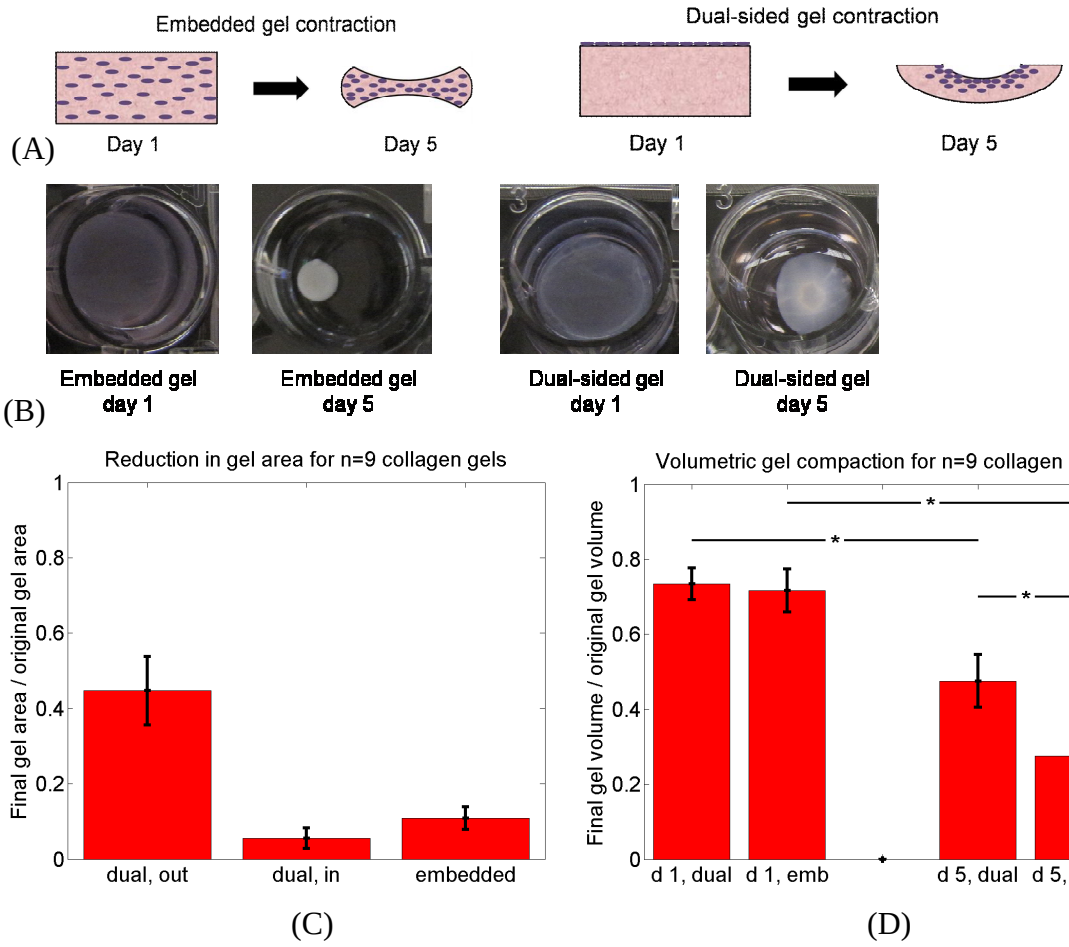

Fig. 9.1: Macroscopic characterization of collagen gels. (A) Schematic illustrating the contraction mechanism in the gels, that result in the embedded gel shaped like a bi-concave disk, while the concavity of the dual-sided gels was found only on the SMC side. (B) Photos of collagen gels in 24-well plates. Note the inner ring in the day 5 dual-sided gels inside of which the cells were found. (C-D) Quantitative macroscopic measurements of gel contraction, expressed as a reduction in gel area (C) and volume (D). (C) Reduction in area was calculated for the inner part of the dual-sided gel (which contained the SMCs), the outer part (which was acellular collagen folded over), and the embedded gel. The reduction in cellular area (the inner ring in the dual sided gel) did not differ significantly from the area of the embedded gel ($P>0.05$). (D) Reduction in volume between the dual-sided and acellular gel on days 1 and 5. Note that both the day 5 gels were significantly smaller from their day 1 analog. Moreover, the volume reduction embedded gel was significantly greater in the day 5 embedded gels in comparison to the day 5 dual-sided gels. *: $P<10^{-7}$.

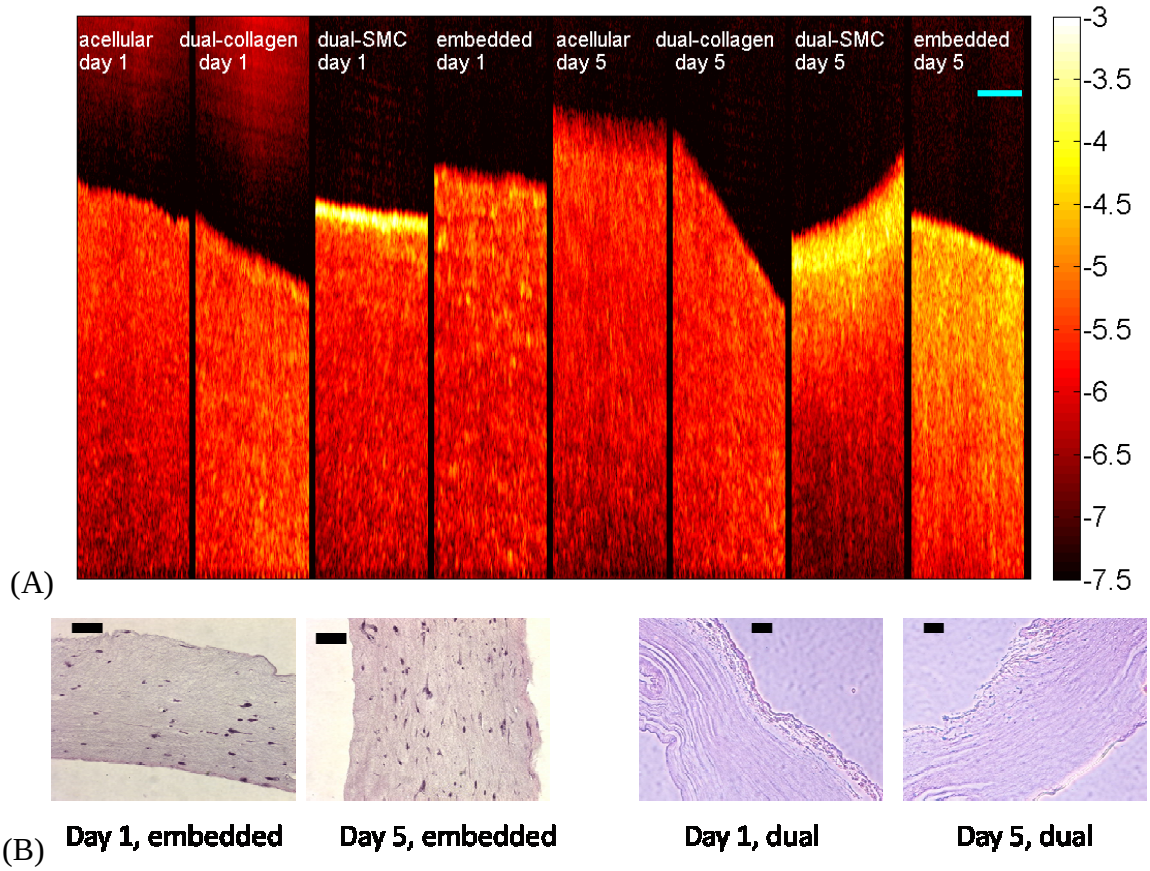

Fig. 9.2: (A) Selected OCT images of collagen gel cross-sections (xz), showing images of acellular, embedded, and both SMC and collagen sides of the dual-sided gels at days 1 and 5. Note that on both day 1 and day 5 the images of the collagen side of the dual-sided gels resemble the acellular gel images. A thin bright layer of cells is seen atop the collagen on the SMC-side of the gel on day 1 (bright line), in contrast to the bright spots distributed throughout the gel in the day 1 embedded gel image. By day 5, it is difficult to visualize structures in either the embedded gels or the SMC-side of the dual-sided gels. (B) Corresponding H&E images of dual and embedded gels. Note the cells are distributed uniformly throughout the embedded gels on both day 1 and day 5, while in the dual-sided gels the SMCs line the periphery on one side (day 1) and penetrate up to approximately 400 μm into the gel (day 5). The colorbar in (A) shows a calibrated reflectivity scale. Bar = 100 μm for all images.

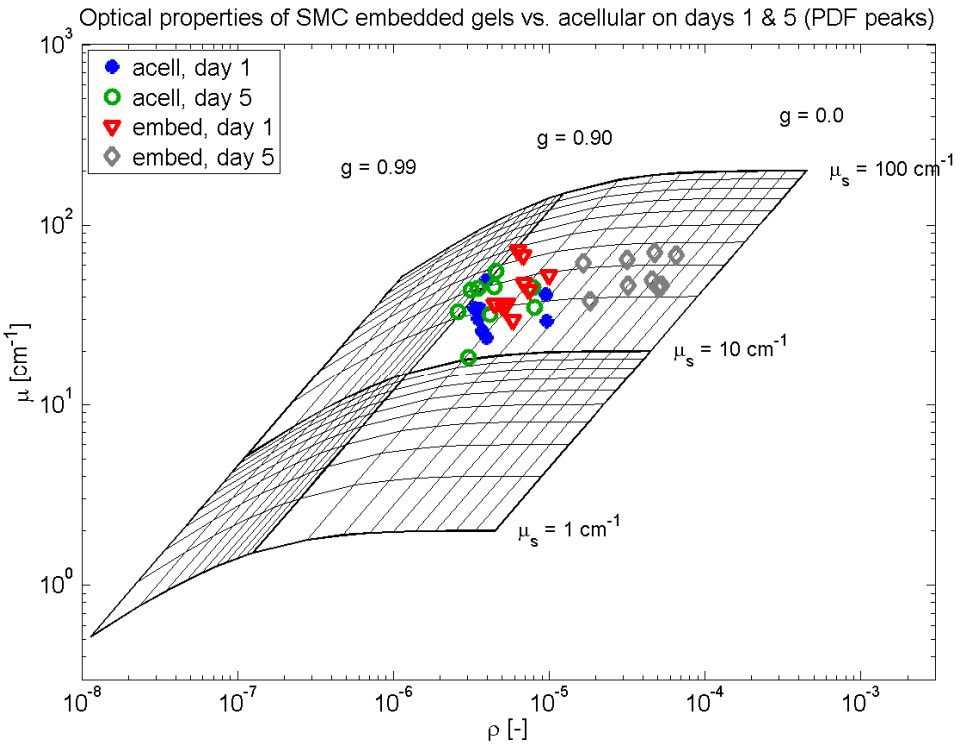
Optical properties of SMC embedded gels vs. acellular on days 1 & 5 (PDF peaks)
acell, day 1
acell, day 5
embed, day 1
embed, day 5
g = 0.99
g = 0.90
g = 0.0
μs = 100 cm-1
μs = 10 cm-1
μs = 1 cm-1
μ [cm-1]
ρ [-]

(A)

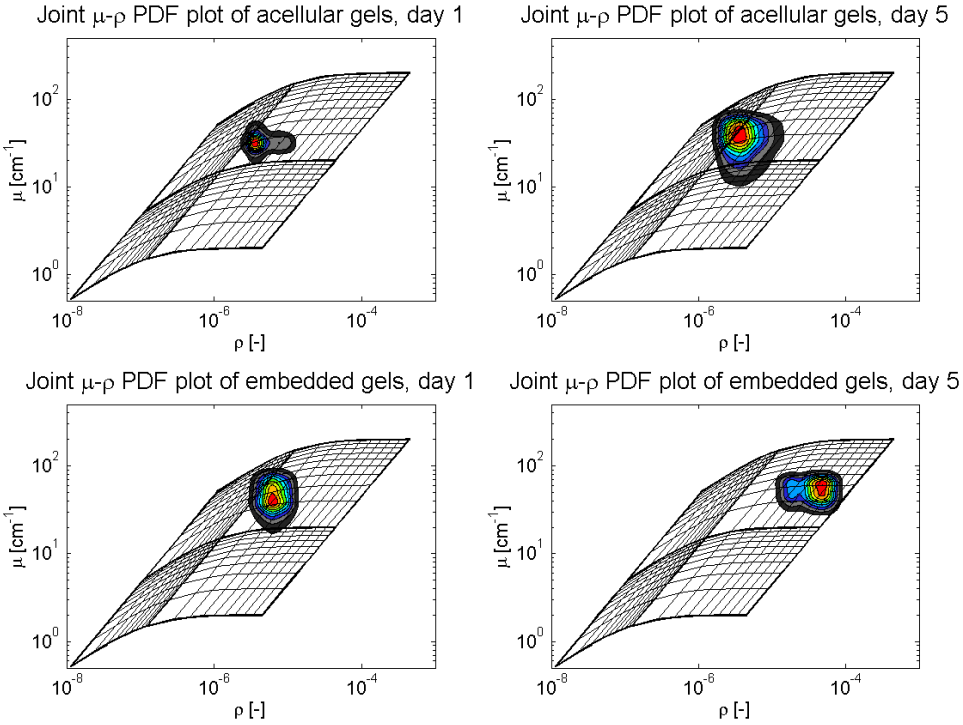
Joint μ-ρ PDF plot of acellular gels, day 1
Joint μ-ρ PDF plot of acellular gels, day 5
Joint μ-ρ PDF plot of embedded gels, day 1
Joint μ-ρ PDF plot of embedded gels, day 5
μ [cm-1]
ρ [-]

(B)

Fig. 9.3 *(on previous page)*: Optical properties of acellular and embedded collagen gels. (A) Peaks of joint PDFs plotted on a grid that maps theoretical (μ_s, g) values to (μ, ρ) space. Note how the 10-fold increase in the reflectivity of the day 5 embedded gels relative to the other gel groups ($P<10^{-9}$). (B) Joint PDFs plotted on grids for each of the 4 groups that illustrate the variance of the fitted results. Grid labels were omitted for clarity.

9.4.C. Embedded gels show 10-fold increase in reflectivity over 5 days

The optical properties from the acellular collagen gels and embedded collagen gels are plotted in Fig. 9.3A. The data are plotted on a grid that maps theoretical (μ_s, g) values into experimental (μ, ρ) space. Each datum point marker represents the (μ, ρ) value that corresponded to the peak of the joint PDF for a specified collagen gel. It can be seen that the day 5 embedded gels have reflectivity values that are roughly 10-fold higher than those of the other 3 groups, corresponding to a decrease in the scattering anisotropy from 0.8-0.9 range to the 0.2-0.5 range. Moreover, the shift in reflectivity was significant ($P<0.10^{-9}$) and consistent with previously reported results [76, 106]. However, no differences in attenuation between any of the 4 groups were observed ($P>0.05$).

An alternative way to analyze the data is to compare the joint PDFs from all 4 groups, which provides an assessment of the variance of the data. In calculating each collagen gel group's joint PDF, every fit (as opposed to every sample) was given equal weight. The joint (μ, ρ) PDFs for the day 1 and day 5 acellular and embedded gels is plotted in Fig. 9.3B. Here, the labels on the (μ_s, g) grid were omitted for clarity. It can be seen that the for the most part, the variance of the optical data in the various groups was moderate. However, side modes can be seen in the day 1 acellular and day 5 embedded data.

9.4.D. SMC side of dual-sided gel has a 5-fold increase in both attenuation and reflectivity

Figs. 9.1-2 showed that remodeling in the dual-sided gels caused them to appear differently than the embedded gels, with all the SMC-related effects concentrated on the SMC side of the gels. In addition to macroscopic physical differences, the optical properties of the dual-sided gels shifted in a different manner than those of the day 5 embedded gels. The optical properties of both the SMC and collagen sides of the dual-sided gels on days 1 and 5 are plotted in Fig. 9.4A. It can be seen that the (μ, ρ) data from both the SMC and collagen sides of the day 1 gels were generally located in the same region in (μ, ρ) space. Similarly, the collagen-side day 5 gels was co-located in the same region of (μ, ρ) space, however, there was one sample with a higher and another with a lower reflectivity, which averaged out without shifting the PDF peak in either direction. However, unlike the embedded day 5 gels which underwent a 10-fold increase in reflectivity with little change in attenuation, a 5-fold increase was observed both in the reflectivity and attenuation in the SMC-side of the day 5 dual-sided gels, corresponding to both a decrease in scattering anisotropy and an increase in the scattering coefficient. The increase in both attenuation and reflectivity of the SMC-side day 5 gels were significant ($P<0.0001$) relative to the other 3 collagen gel groups. No significant differences in either attenuation or reflectivity were found between the other gel groups.

Similarly to the optical data from the acellular and embedded gels, the joint (μ, ρ) PDFs from the dual-sided gels are plotted in Fig. 9.4B. The appearance from these distributions differs considerably from those seen in the acellular and embedded gels (Fig. 9.3B). Specifically, both sides of the day 5 dual-sided gels joint PDFs contain multiple modes. A careful examination of our data showed that these secondary modes corresponded to variations between different samples, as opposed to similar variations within each sample that are consistent across the multiple samples. For example, the secondary mode in the SMC-side day 5 gels (Fig. 9.4B) comes from the (μ, ρ) data from the 3 samples with lower attenuation (Fig. 9.4A). Collectively, these data suggest that the inter-sample variability is greater than the intra-sample variability.

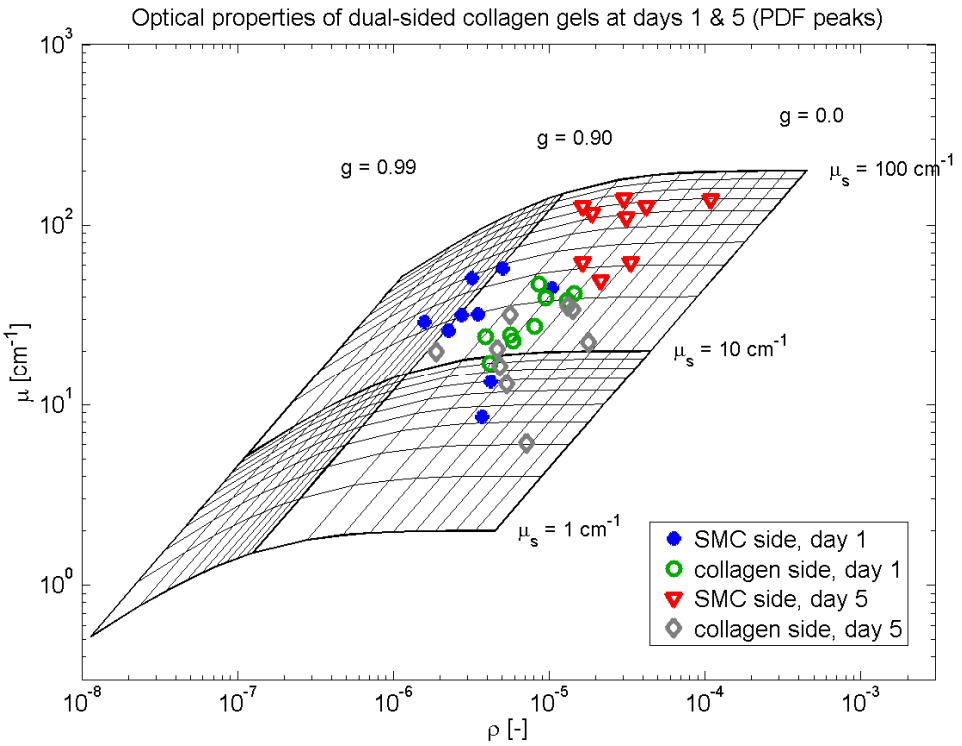
Optical properties of dual-sided collagen gels at days 1 & 5 (PDF peaks)
g = 0.0
g = 0.90
g = 0.99
μs = 100 cm-1
μs = 10 cm-1
μs = 1 cm-1
SMC side, day 1
collagen side, day 1
SMC side, day 5
collagen side, day 5
μ [cm-1]
ρ [-]

(A)

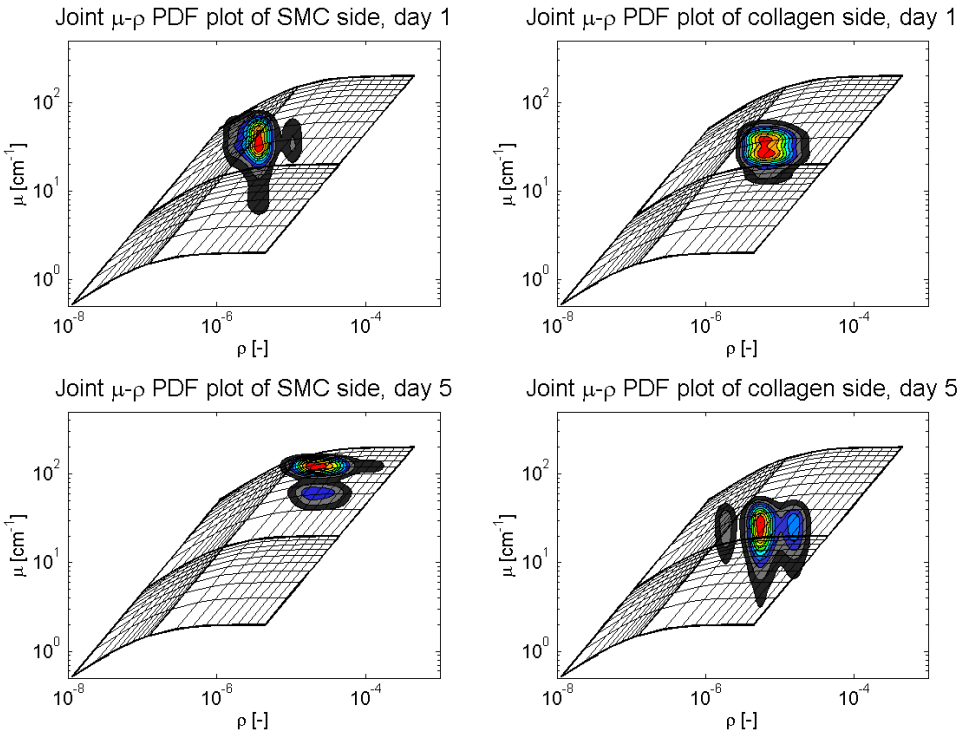
Joint μ-ρ PDF plot of SMC side, day 1
Joint μ-ρ PDF plot of collagen side, day 1
Joint μ-ρ PDF plot of SMC side, day 5
Joint μ-ρ PDF plot of collagen side, day 5
μ [cm-1]
ρ [-]

(B)

Fig. 9.4 *(on previous page)*: Optical properties of dual-sided collagen gels on days 1 and 5. (A) Scatter plots of (μ, ρ) values that corresponded to peak of joint PDFs plotted on a grid that shows how theory maps to experiment. The SMC-side day 5 gels differed significantly from the other 3 collagen gel groups in both attenuation and reflectivity ($P<0.0001$). (B) Plots of joint PDFs for collagen- and SMC-sides of the dual-sided gels on days 1 and 5. Note the multiple modes observed in the day 5 data come from inter-sample variability, not intra-sample variability.

9.4.E. Optical properties of the SMC side on the day 5 dual-sided gels have a depth dependence

When analyzing the fitting results, we noticed that in the SMC-side of the day 5, dual-sided gels, the signal did not follow a linear decay when plotted on a log scale. This feature was unique to the SMC-side day 5 data. To illustrate this concept, a representative averaged A-scan from a single ROI is plotted in black in Fig. 9.5A, with the fitting area (100-400 μm) highlighted in green X's. We then broke up the 100-400 μm depth range into 3 segments of 100 μm, and fitted them to the μ-ρ model (blue, red, and gray lines). It can be seen that as the fitting depth range increases, both the attenuation and reflectivity decrease. Extending this analysis to the entire sample (Fig. 9.5B) shows that indeed that fits from different depth-dependence are grouped separately in (μ, ρ) space, with some minor overlap. In this plot, each datum point represents a single fit. Only data from one sample is shown given the inter-sample variability in these gels (Fig. 9.4B).

To better understand this phenomenon, we analyzed our data more systematically. Specifically, we reprocessed all the dual-sided gel data, further segmenting the data along the depth direction into 3 regions: 100-200, 200-300, and 300-400 μm, similar to Fig. 9.5A-B. Because of the great inter-sample variability, we normalized the fitted attenuation and reflectivity values by the fit results from 100-400 μm depth range *on the collagen side of the same gel*, where depth-dependence to the decay was not observed. For simplicity, we call these ratios the normalized attenuation and reflectivity.

The normalized reflectivity and attenuation from both sides of the dual sided-gels are shown in Fig. 9.5C-D, respectively. Fig. 9.5C shows that there only the SMC side of the day 5 gels had a depth-dependence, which can be seen by the decrease in the normalized attenuation and reflectivity with increasing depth range; in the other 3 groups, the normalized reflectivity results were approximately 1. The same basic trend is observed for both normalized reflectivity and attenuation (Fig. 9.5C-D, respectively), though the normalized reflectivity decreases from 10 to 1, while the normalized attenuation decreases from 8 to 1. However, there were some differences between the 2 parameters statistically. The normalized reflectivity on the 100-200 μm depth range on the SMC side was significantly different ($P<0.05$) from all depth ranges on either side of the day 5 gels. Moreover, the P value between the normalized reflectivity on the 100-200 μm depth range on the SMC side and the 3 depth ranges on the collagen side, as well as the 300-400 μm depth range was even smaller ($P<10^{-5}$). In terms of normalized reflectivity, none of the other groups in the *post hoc* analysis were statistically different from any other. As for the normalized attenuation, the 100-200 μm depth range on the SMC side (day 5) was significantly different than the 300-400 μm depth range on the SMC side ($P<0.05$), and very significantly different than all 3 depth ranges on the collagen side ($P<0.0001$). However, the 100-200 μm depth range on the SMC side was not significantly different than the 200-300 μm on the SMC side. Moreover, the normalized attenuation from the 200-300 μm depth range on the SMC side was significantly different from all 3 depth ranges on the collagen side ($P<0.01$). For completeness, none of the depth ranges in either side of the day 1 gels were significantly different from one another, in terms of either normalized attenuation or normalized reflectivity.

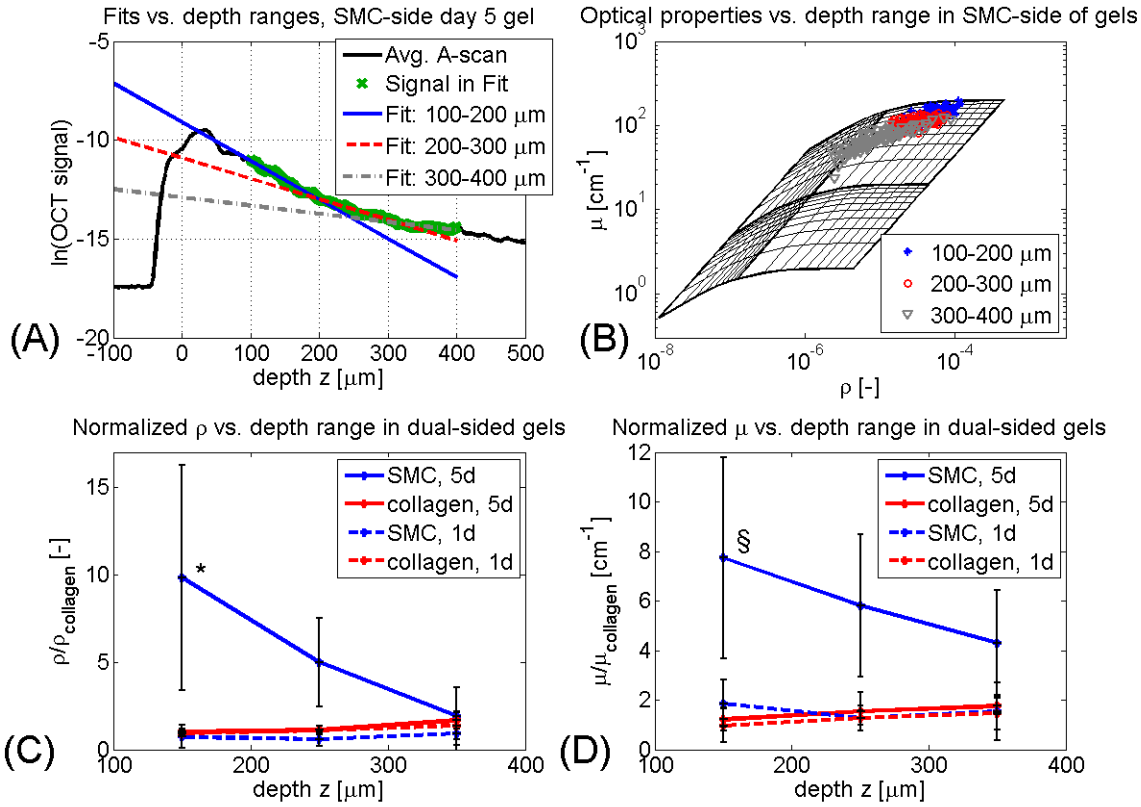

Fig. 9.5: Depth dependence of optical properties in SMC side of dual-sided gels. (A) Average A-scan from a representative ROI in the SMC-side of the dual-sided gels. Fits from 3 different depth regions result in 3 different (μ, ρ) pairs. (B) Comparison of fit results from a representative sample plotted on grid. Here, each datum point represents a single fit. It can be seen that as the fitting depth range increases, both the attenuation and reflectivity decrease. (C) Plots of mean reflectivity from different depth ranges in SMC- and collagen-sides of dual-sided gels (both days 1 and 5), normalized to the reflectivity fitted from 100-400 μm on the collagen side. It can be seen that only the day 5 SMC-side of the dual gels has depth-dependent optical properties. (D) Corresponding plot for attenuation, showing a similar behavior only in the day 5 SMC-side of the dual gels. Error bars represent standard deviation between various samples and resulted mainly from inter-sample variability. *: $P<0.05$ versus every other group, §: $P<0.05$ versus every group except 200-300 μm from SMC side, day 5.

In trying to make practical sense out of this analysis, recall that attenuation μ and reflectivity ρ contain information on the local composition of the gel. Specifically, we have shown earlier that the scattering coefficient μ_s (and similarly attenuation μ) strongly correlated with cell density, while reflectivity provides an indirect measure of the local MMP activity in the gel. Thus, the higher attenuation and reflectivity in the superficial regions of the SMC side of the gels suggests that there was a higher concentration of cells and MMP activity. Both of these results are expected given the initial localization of cells on one side of the gel. Moreover, the above analysis suggests that the 300-400 μm depth range is where both SMC concentration and MMP activity cannot be distinguished from the surrounding collagen matrix. This depth range is comparable with the histological sections, in which the cells penetrated approximately 400 μm into the collagen matrix.

9.5. Discussion

In this paper, we used OCT to image and quantitatively analyze multiple sets of collagen gels, including acellular gels, gels with embedded with SMCs, and gels with the SMCs plated on the top surface only. Our aim was to see if the optical properties can be used to assess the relationship between SMC localization and matrix remodeling. The gels were imaged at day 1 and day 5, before and after major matrix remodeling took place. Over 5 days, no significant changes in optical properties were measured in the acellular gels. The embedded gels showed a 10-fold increase in reflectivity with no change in attenuation that corresponded to a decrease in the scattering anisotropy with no change in the scattering coefficient. Attenuation and reflectivity data from the 2 sides of the dual sided gels showed no significant difference on day 1. However, on day 5 the optical properties on the SMC side had reflectivity and attenuation values that were 5-fold higher than their day 1 values, while the optical properties on the collagen side remained similar to their day 1 values. Moreover, the decay in the OCT signal on the SMC side of the dual-sided gels showed a depth dependence, such that the superficial (100-200 μm) regions had higher attenuation and reflectivity than deeper (300-400 μm) regions, which had similar optical properties to the collagen side of the gels. Given the

relationship that we established earlier between the optical properties and cell density and MMP activity, the data suggest that elevated cell densities and MMP activity are found up to 400 μm from the gel surface on the SMC side. These findings were qualitatively confirmed by histology.

Recently, we used the method of measuring optical properties from OCT image to characterize remodeling in embedded collagen gels. Our initial experiments showed that there is a consistent increase in reflectivity over 5 days [76, 106]. We identified matrix remodeling, specifically MMP activity, as having caused the measured reflectivity increase. When MMP activity was blocked by doxycycline, a non-specific MMP inhibitor, the increase in reflectivity was considerably reduced [106]. Moreover, treating day 1 acellular gels with collagenase 2 (MMP-8) for 3 hr caused a significant 3-fold increase in reflectivity [106], showing that MMPs alone can change the reflectivity of collagen gels.

The results presented in this paper confirmed our earlier results. Specifically, the 10-fold increase (Fig. 9.3) was very similar to results we reported earlier [106]. However, while the earlier collagen gels were grown in 12-well plates (diameter/height = 9), the gels here were grown in 24-well plates (diameter/height = 2.4). Note that we chose 24 well plates for this set of experiments for 2 reasons. First, the smaller area would increase the cell density (cell/cm^2) when plating SMCs on the collagen gel surface. Secondly, the larger gel height in the 24 well plates meant that cells and MMPs would have a longer distance to diffuse across in order to reach the other side, yielding a clearer separation in optical properties. The data in Fig. 9.3 suggest that the diameter/height ratio of the embedded collagen gel does not influence the optical properties.

The optical properties measured from the dual-sided gels proved a bit more complicated to analyze and interpret than those of embedded gels. The joint PDF of the day 5 dual-sided gels showed multiple modes on both the collagen and SMC sides. Moreover, the additional modes showed no consistent behavior. A careful assessment of every individual dual-sided gel's joint PDF relative to the joint PDF of the given collagen

gel group revealed that the increased variance was due to inter-sample variability, as we saw that the individual gels' PDFs (data not shown) only contained 1 mode.

From day 1 to day 5, the observed shifts in optical properties of the SMC side of the dial-sided gels were a 5-fold increase in both attenuation and reflectivity, meaning that the scattering coefficient increased and the scattering anisotropy decreased. In a previous paper, we showed that the cell density in collagen gels was highly correlated with the scattering coefficient [76]. However, these experiments were done with 6 hr gels, in which the collagen remodeling by the cells was minimal. On the SMC side of the day 5 dual-sided gels, the SMCs were co-located in the regions of the gel that were remodeled (at day 1, there were no cells in the fitting depth range, as none of the cells penetrated the matrix, Fig. 9.2A). However, the overall increase in attenuation observed on the SMC side (Fig. 9.4A), as well as the depth-dependent increase in attenuation at the superficial regions (Fig. 9.5D) in which the histology section showed most of the cells to be concentrated (Fig. 9.2B) suggests that the relationship between cell density and scattering coefficient might hold for remodeled matrices as well.

Another challenge we faced was the depth-dependence of the scattering properties (Fig. 9.5). The gels contained a gradient of cells and MMPs along the depth direction, and since both cell density and MMP activity influence optical properties, a gradient in optical properties was expected. From a biomedical optics perspective, a tissue with depth-dependent optical properties poses several challenges. One issue has to do with the fact that the μ-ρ model [8] used to analyze the data assumes that the imaged sample is a turbid medium with uniform optical properties, which is not the case here. Since the μ-ρ model is based on the inverse Monte Carlo method, one could adapt current Monte Carlo technique to address this problem. Other groups who have attempted to break the medium into layers and describe them analytically ended up with very complicated equations; however, given their complexity it would be difficult to use these equations for fitting and extracting meaningful information from data [31, 107]. Another optics-related issue is multiple small-angle scattering that contribute to the OCT signal at optical depths $\mu_s z > 1$. The result of multiple scattering is a gradual reduction of the attenuation (and

implicitly, the reflectivity) with depth [9]. Although the effects of multiple scattering are similar to the observed decay gradient, we do not suspect it heavily influenced our data. The maximum optical depth interrogated in these experiments was <2.5. Experiments in our lab using polystyrene sphere in agarose gels showed that our fit results were comparable with values predicted by theory for optical depths up to 3 (data not shown). Moreover, forward Monte Carlo simulations showed that multiple scattering does not have considerable effects until optical depths of 4-5.

Despite these caveats, our analysis that suggested that the SMCs and MMP activity were found up to 400 μm into the gels (both SMCs and a degraded matrix were qualitatively observed in the H&E sections), can be considered as a first approximation that addresses how to assess the localization of SMCs and MMP activity within a collagen gel. To our knowledge, we are the first to estimate the extent of SMC migration and MMP diffusion within collagen gels using non-destructive means. And while data presented here does not allow us to separate the optical scattering effects of the SMCs from the MMPs, improved modeling and analysis make the prospect of accomplishing such tasks feasible. Moreover, it is worth noting that while there has not been much information in the literature regarding the localization of MMPs in engineered tissues, histological analyses of MMP activity in real tissues shown that MMPs are active near the cells that secrete them [70]; however, this reported data was more qualitative than quantitative.

Both matrix remodeling and cellularity are important parameters to document when developing engineered tissues. Cell number and localization are important variables in the design of engineered tissues [108]. The ultimate success of engineered tissues is dependent on the characteristics of these microstructures [109]. Matrix remodeling, specifically MMP activity, plays important roles in physiology and pathology, as well as tissue engineering [61, 69, 50, 103]. Indeed, tissue engineering can be seen as a remodeling problem, with the course of remodeling being determined by the state of the matrix [21]. Thus, it is critical to understand remodeling in order to properly manipulate it for the desired tissue engineering application. We believe that measuring

the optical properties from OCT images of the engineered tissues, which was shown to be sensitive to both cell density and MMP activity, offers a promising route to advancing these objectives.

The present study highlights some of the advantages of measuring optical properties from OCT data. OCT already possesses many features of interest for tissue engineers, including a ~10 μm resolution and a penetration depth of up to 1 mm [24, 22]. OCT imaging is non-destructive and label-free, allowing for repeated measurements on the same imaging site. Moreover, current Fourier-domain OCT systems can image tissues faster than video rate [23]. As a fiber-based technology, OCT can also be coupled into incubators for continuous time-lapse non-destructive monitoring of engineered tissues. To this already well-developed repertoire, one can add the ability to measure optical properties from OCT data. Previous studies have shown that the technique is sensitive to both the cell density [76] and MMP activity [8]. Others have used the technique to characterize atherosclerotic plaques [30, 79, 110] as well as diagnose cervical cancer [31]. In the current study, the method of measuring optical properties was used to analyze the signal from different depth regions and showed, to a first approximation, the depth at which SMCs and MMPs can reach over 5 days was roughly 400 μm. And although the maximum depth range to which the method was applied was limited to 400 μm, a simple redesign of the system and improved theoretical modeling would enable quantifying optical properties for depth ranges up to 1 mm. The ability to quantitatively characterize collagen microstructure at different depths and make indirect assessments of cell density and MMP activity holds considerable promise in tissue engineering.

9.6. Conclusion

In this paper, the optical properties of different types of collagen gels that were measured from OCT data were compared at days 1 and 5. The results showed that in collagen gels with SMCs embedded into the matrix, there was a 10-fold increase in reflectivity with little change in attenuation, which was not observed in acellular gels

(Fig. 9.3). Imaging and analyzing collagen gels in which the SMCs were plated on top of the collagen matrix showed that the optical properties between the 2 sides differed on day 5 but not day 1 (Fig. 9.4). On day 5, the SMC-side showed a 5-fold increase in both attenuation and reflectivity. Further analysis of the OCT signal decay rate at different depth ranges showed that the regions with elevated reflectivity and attenuation were located in the superficial regions, and that optical properties of regions located 300-400 μm or deeper within the tissue (on the SMC side) were similar to those on the collagen side (Fig. 9.5). Based on earlier work which showed that the optical properties were affected by SMC density and MMP activity, we estimated that the cells did not penetrate deeper than 400 μm into the collagen matrix; this estimate was qualitatively confirmed by histology. These data suggest that the optical properties of collagen gels can be used to estimate cell localization and local matrix remodeling within collagen gels non-destructively.

Chapter 10: Concluding remarks

This thesis developed the methodology of measuring optical properties from optical coherence tomography (OCT) signals and applied it to characterizing matrix remodeling of collagen gels seeded with smooth muscle cells (SMCs). By fitting the depth-dependent signal to the μ-ρ model, it is possible to extract out the attenuation and reflectivity of the imaged sample. The attenuation and reflectivity map back to the optical properties of the imaged tissue, namely, the scattering coefficient μ_s and anisotropy factor g. By imaging multiple sites on multiple samples, it is possible to tabulate statistics on the local optical properties, which can be used to estimate the mean and variance of the optical properties within a group of samples.

The μ-ρ model used here has several features uniquely suited for measuring optical properties. The main expression is a simple exponential decay, meaning that it can be linearized and solved directly rather than iterating a solution. There are 2 output parameters – attenuation μ and reflectivity ρ – which map back to 2 properties, μ_s and g. Importantly, the confocal imaging geometry is one of the few imaging geometries in which it is possible to separately measure μ_s and g. The μ-ρ model also identified how anisotropy affects the single decay even in the single scattering regime, which, as discussed in Ch. 4, challenges the current paradigm of single-scattering theory.

Moreover, implementing the technique does not require a specialized sample arm setup or expensive hardware.

10.1. Significant findings

Throughout this thesis, there were several important findings. This section will provide a brief overview of the key results from the thesis and highlight the relevant figures.

The first key result (Fig. 10.1, originally in Ch. 6) is the plot that characterizes the accuracy of the algorithm, as well as the intra-ROI variability in sphere phantoms. These results demonstrate the accuracy and reproducibility of the method, and strengthen the validity of measurements presented throughout this thesis. In terms of accuracy, the (μ, ρ) results were mapped back to corresponding (μ_s, g) pair and compared to results evaluated from spectrally-resolved collimated transmission measurements. Here, the fitted μ_s values were overestimated by 22 %, while the fitted g was underestimated by 4 %. In terms of reproducibility, the intra-ROI variability, expressed as a coefficient of variation, was 5 % for μ and 10 % for ρ. Given that the optical property data measured by OCT is analyzed on a log scale, the systematic biases/errors in these measurements are for the most part negligible.

The second key result (Fig. 10.2), the most important result shown in this thesis, is the plot that shows the change in optical properties in SMC collagen gels from day 1 to day 5. Throughout this thesis, this experiment was repeated about 15 times over 3 years, varying several key parameters (4 different sources of SMCs, 3 OCT system designs, and 12-well versus 24-well-plate). Despite all these variations, the results were remarkably consistent, showing an increase in ρ from ~10^{-6} to ~10^{-5} with little change in ρ, corresponding to a decrease in g from 0.8-0.9 to 0.25-0.5. Some variation of this plot was shown in Ch. 7-9. The 10-fold increase in ρ from day 1 to day 5 illustrates the significant changes the gels underwent, and is suggestive of a fundamental change in the size and density of the scattering particles that took place.

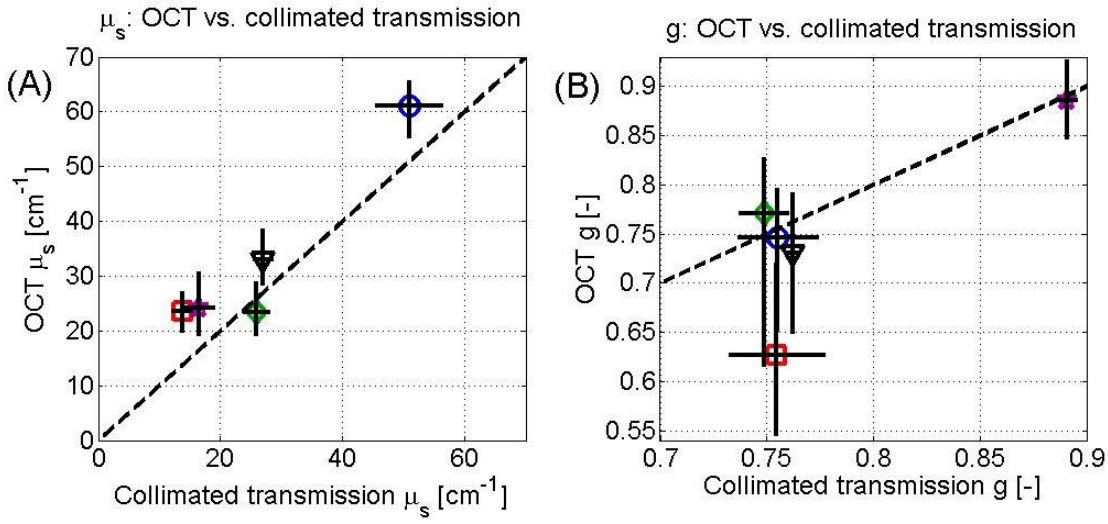

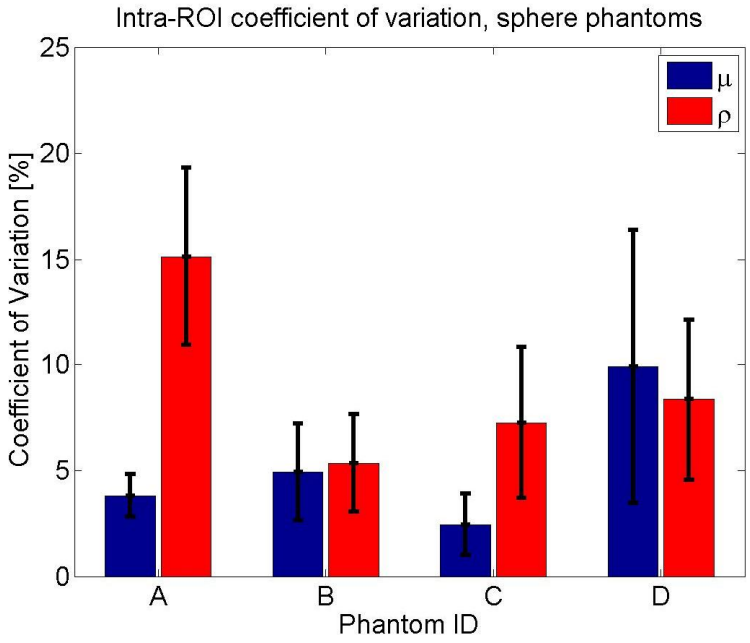

(C)

Fig. 10.1: Accuracy (A) and reproducibility (B) of the method of measuring optical properties from OCT data. (A) Comparison of μs and g evaluated by OCT (via μ and ρ) and from spectrally-resolved collimated transmission measurements. The dashed line represents the y = x line, with the collimated transmission measurements considered "truth". (B) Intra-ROI variability, expressed as a coefficient of variation, for 4 sphere phantoms. All data values are showed in percent as means ± standard deviations. Details of the phantoms are found in Table 6.1.

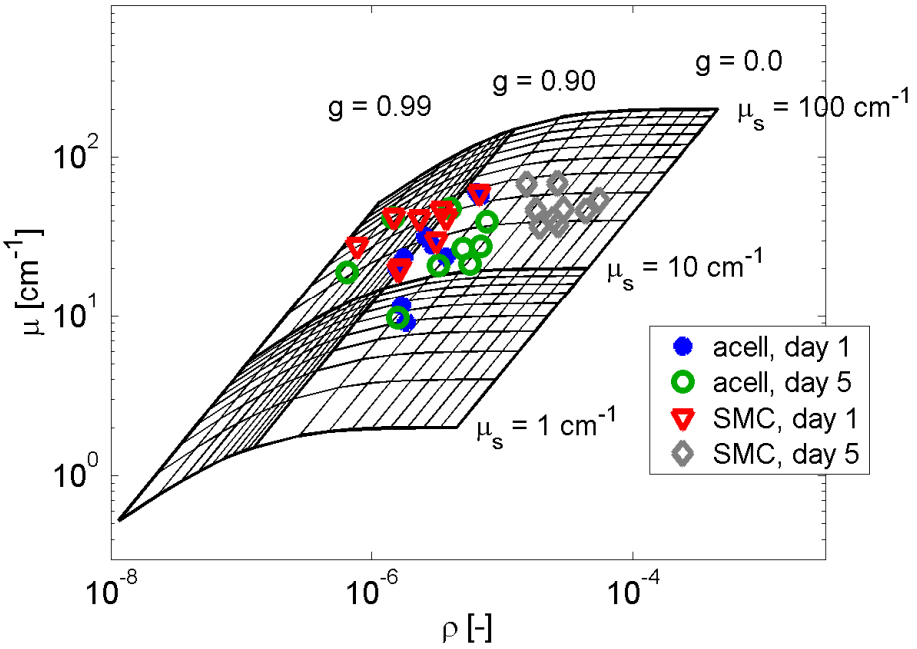

Fig. 10.2: μ-ρ plot of acellular and SMC gels on days 1 and 5. Note the reflectivity ρ of the day 5 SMC gels is 10-fold higher than the day 1 values, as well as those of acellular gels. This change corresponded to a decrease in anisotropy g, with little change in scattering coefficient μ_s.

Another important result (Fig. 10.3, from Ch. 8) is the relationship between anisotropy g and matrix remodeling, specifically, matrix metalloproteinase (MMP) activity. In trying to identify what caused the decrease in anisotropy in SMC collagen gels over 5 days (Fig. 10.2), another set of SMC collagen gels was prepared in which MMP activity was blocked using the non-specific MMP inhibitor doxycycline. The decrease in anisotropy was impeded in the doxycycline-treated (dox+) gels relative to the untreated (dox-) gels, as shown in Fig. 10.3A. The corollary to the doxycycline experiment was treating day 1 acellular gels with collagenase II (MMP-8) for only 3 hours. Fig. 10.3B shows that even in the absence of SMCs, the anisotropy of the gels decreased after treatment for 3 hr with collagenase relative to the untreated acellular gels. Thus, while the doxycycline experiment illustrated that MMP activity is necessary for the observed changes in optical properties, the collagenase experiment showed that MMP activity is sufficient to induce such changes. Given that remodeling and MMPs are

important concepts in many areas of (patho)physiology, the ability of OCT to assess MMP activity non-invasively could prove to have profound implications across many fields in biomedicine, including atherosclerosis, cancer research, wound healing, as well as tissue engineering.

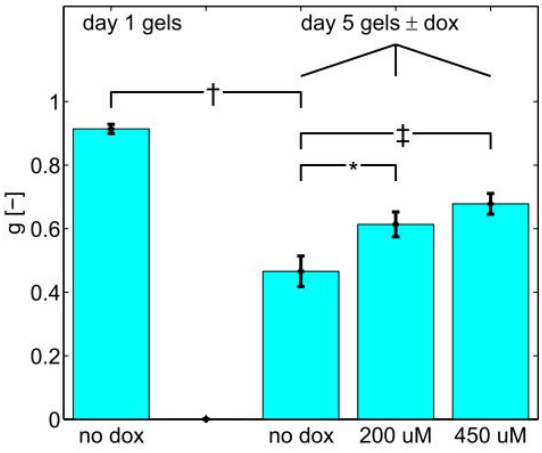

(A)

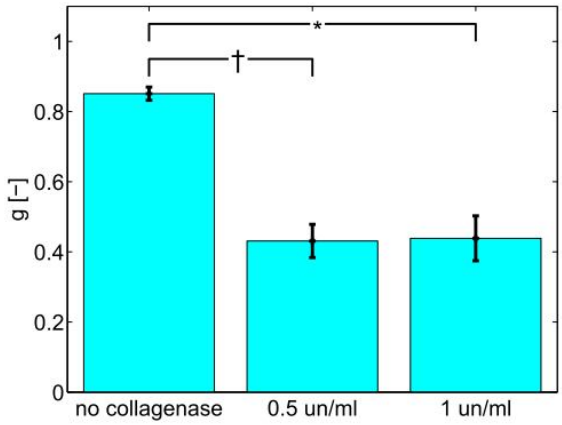

(B)

Fig. 10.3: Relationship between anisotropy g and MMP activity. (A) Comparison of anisotropy g of day 5 SMC gels treated with(out) doxycycline. Also plotted for reference is the anisotropy of day 1 gels. It can be seen that doxycycline impeded the decrease in g seen in the untreated gels. (B) Effect of collagenase 2 (MMP-8) on anisotropy of day 1 acellular gels, showing that with MMP treatment it is possible to reproduce structural changes in the collagen in 3 hr that are comparable to those produced by SMCs over a 5 day period.

Finally, a last key result (from Ch. 7) is the relationship between cell density and optical properties of (unremodeled) collagen gels, in which cell density was found to be highly correlated to μ_s, but uncorrelated to g. Fig. 10.4 plots both μ_s and g against cell density, showing a linear relationship between cell density and μ_s, with a rate increase of 10.7 cm^{-1} per 10^6 cell/ml of cell density (Fig. 10.4A). In contrast, g appeared to be unaffected by the increase in cell density (Fig. 10.4B). Subsequent experiments in the appendix of Ch. 7 have corroborated these results. These results are significant because they illustrate that cells act as isolated scattering particles, implying that it is possible to predict optical properties based on cell density, which could impact the use of optical technologies in tissue engineering and elsewhere in biomedicine.

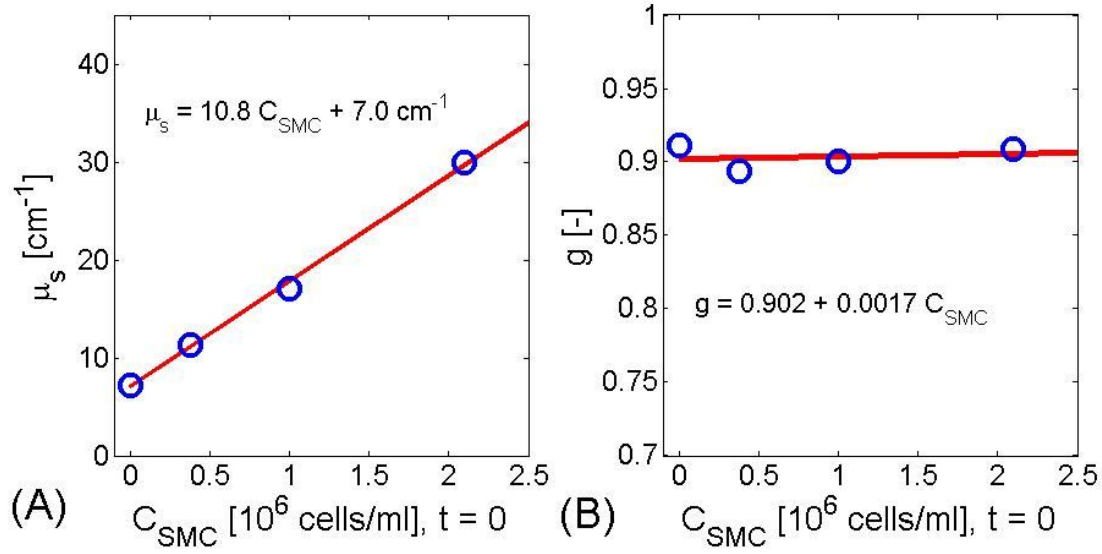

Fig. 10.4: Optical properties versus cell density in collagen gels at 6 hr, showing that μ_s and cell density in collagen gels are highly correlated, while g and cell density are uncorrelated.

10.2. Outlook

The results presented in this thesis have wide applicability in the field of tissue engineering and beyond. The doxycycline and collagenase experiments from Ch. 8 illustrate that measuring optical properties from OCT data can be used to assess the effects certain drugs have on local remodeling. The analyses of depth ranges in Ch. 9

showed that it is possible to detect changes in cell density and MMP activity as closely as 200 μm. The close proximity between the 2 depth ranges suggests that this technique can be used to make precise, localized measurements.

Additionally, the experiments presented in this thesis have implications for other applications within tissue engineering. For example, the degree of mineralization in engineered bone grafts is an important factor determining its mechanical properties. It has been shown that mineralized tissue has a high refractive index, meaning that the increase in mineral deposits in osteoblasts and osteocytes should have a strong scattering signature. Since mineralization is a slow process that takes weeks, one could easily conceive of experiments in which the optical properties of bone constructs are monitored over time and mineralization is indirectly assessed.

The technique of measuring optical properties from OCT and confocal signals does have its limitations. The μ-ρ model used here does not properly account for defocusing effects. However, in many OCT systems, a low numerical aperture (NA) objective lens with the focus fixed near the tissue boundary is used in many Fourier domain setups in order to speed up image acquisition. Thus, the optimal system design for rapid image acquisition is not optimal for measuring optical properties (which works better at higher NA values), and there is a tradeoff between these 2 applications. Another limitation is hardware-related. One of the key pieces of hardware is the piezo-driven lens mount, which shifts the objective lens towards/away from the sample and implicitly determines the maximum fitting depth. To our knowledge, there are not many commercially available piezo-driven lens mounts that can travel more than 400 μm. However, beyond this depth multiple scattering becomes an important factor, and the μ-ρ model is limited in its ability to handle multiple scattering effects.

Despite these basic limitations, this thesis illustrated how to turn a simple imaging system into a highly specialized analytical tool. The technique developed here can be easily implemented on any confocal microscopes that are found in many tissue engineering labs. This OCT method is both non-destructive and label free, meaning it is

possible to make repeated measurements without destroying the sample. It is also inexpensive and does not require much specialized hardware. And perhaps most importantly, the optical properties of collagen gels are sensitive to 2 parameters that are critical to tissue engineers – cell number and MMP activity. Collectively, these features hold considerable promise for use in tissue engineering.

References

1. Eds. AJ Welch and MJC van Gemert, *Optical-thermal response of laser-irradiated tissue*. (Plenum, New York, 1995).
2. DJ Williams and IM Sebastine, "Tissue engineering and regenerative medicine: manufacturing challenges", *IEE Proc. Nanobiotechnol* **152**, 207-210 (2005).
3. T Guda, M Appleford, S Oh, and JL Ong, "A cellular perspective to bioceramic scaffolds for bone tissue engineering: The state of the art", *Curr Top Med Chem* **8**, 290-299 (2008).
4. ST Ho and DW Hutmacher, "A comparison of micro CT with other techniques used in the characterization of scaffolds", *Biomaterials* **27**, 1362-1376 (2005).
5. CW Jones, D Smolinski, A Keogh, TB Kirk, and MH Zheng, "Confocal laser scanning microscopy in orthopaedic research", *Prog Histochem Cytochem* **40**, 1-71 (2005)
6. DB Smith, MS Sacks, PM Pattany, and R Schroeder, "High-resolution magnetic resonance imaging to characterize the geometry of fatigued porcine bioprosthetic heart valves", *J Heart Valve Dis* **6**, 424-432, (1997).
7. D Huang, EA Swanson, CP Lin, JS Schuman, WG Stinson, W Chang, MR Hee, T Flotte, K Gregory, CA Puliafito, and JG Fujimoto, "Optical coherence tomography", *Science* **254**, 1178-1181 (1991).
8. SL Jacques, D Levitz, R Samatham, DS Gareau, N Choudhury, F Truffer, Light scattering in confocal reflectance microscopy. In "Biomedical Applications of Light Scattering," eds. A. Wax, V. Backman. (McGraw Hill, 2010).

9. L Thrane, HT Yura, and PE Andersen, “Analysis of optical coherence tomography systems based on the extended Huygens-Fresnel principle”, *J Opt Soc Am A* **17**, 484-90 (2000).
10. E Bell, B Ivarsson, and C Merrill, Production of a tissue-like structure by contraction of collagen lattices by human fibroblasts of different proliferative potential in vitro. *Proc. Nat. Acad. Sci. USA.* **76**, 1274-78, 1979.
11. CF Bohren and DR Huffman, *Absorption and scattering of light by small particles* (John Wiley & Sons, Inc., New York, NY 1983).
12. J Swartling, *Biomedical and atmospheric applications of optical spectroscopy in scattering media*. PhD Thesis, Lund Institute of Technology (2002).
13. LG Henyey and JL Greenstein, “Diffuse radiation in the galaxy”, *Astrophysical J.* **93**, 70-83 (1941).
14. JW Pickering, SA Prahl, N van Wieringen, JF Beek, HJCM Sterenborg, and MJC van Gemert, “Double-integrating-sphere system for measuring the optical properties of tissue”, *Appl Opt*, **32**, 399-410 (1993).
15. SA Prahl, Inverse Adding-Doubling Software. 1999. http://omlc.ogi.edu/software/iad/index.html.
16. J Swartling, JS Dam, and S Andersson-Engels, "Comparison of spatially and temporally resolved diffuse-reflectance measurement systems for determination of biomedical optical properties," *Appl Opt* **42**, 4612-4620 (2003).
17. TJ Farrell, MS Patterson, and B Wilson, “A diffusion theory model of spatially resolved, steady-state diffuse reflectance for the noninvasive determination of tissue optical properties *in vivo*”, *Med Phys* **19**, 879-888, (1992).
18. SL Jacques and BW Pogue, “Tutorial on diffuse light transport”, *J Biomed Opt* **13**, 041302 (2008).
19. JR Mourant, TM Johnson, S Carpenter, A Guerra, T Aida, and JP Freyer, “Polarized angular dependent spectroscopy of epithelial cells and epithelial cell nuclei to determine the size scale of scattering structures”, *J. Biomed. Opt.* **7**, 378-387 (2002).
20. LR Jones and SL Jacques, “Comparing 2-D screen projections to 1-D goniometric measurements in scattering studies of surface roughness”, in Spectroscopy,

Optics, and Scattering III, SL Jacques and WP Roach, eds, *Proc SPIE* **7175**, 71750E (2009).

21. RM Nerem, "Tissue Engineering: The Hope, the Hype, and the Future". *Tissue Eng* **12**, 1143-1150, 2006.
22. C Mason, JF Markusen, MA Town, P Dunnill, and RK Wang. The potential of optical coherence tomography in the engineering of living tissue. *Phys Med Biol* **49**, 1097-1115, 2004.
23. R Huber, M Wojtkowski, K Taira, JG Fujimoto, and K Hsu. Amplified, frequency swept laser for frequency domain reflectometry and OCT imaging: design and scaling principles. *Opt Expr* **13**, 3513-3528, 2005.
24. JM Schmitt, "Optical Coherence Tomography (OCT): A Review", *IEEE J Sel Top Quant Elec* **5**, 1205-1215, 1999.
25. T Collier, M Follen, A Malpica, and R Richards-Kortum, "Sources of scattering in cervical tissue: determination of the scattering coefficient by confocal microscopy", *Appl. Opt.* **44**, 2072-2081 (2005).
26. JM Schmitt, A Knüttel, and RF Bonner, "Measurement of optical properties of biological tissue by low coherence reflectometry", *Appl opt* **32**, 6032-42 (1993)
27. JM Schmitt, A Knüttel, M Yadlowsky, and EA Eckhaus, "Optical-coherence tomography of a dense tissue: statistics of attenuation and backscattering", *Phys Med Biol* **39**, 1705-1720 (1994)
28. TG van Leeuwen, DJ Faber, MC Aalders, "Measurement of the axial point spread function in scattering media using single-mode fiber-based optical coherence tomography", *IEEE J. Sel. Top. Quantum Electron.* **9**, 227-233 (2003).
29. LS Dolin, "A theory of optical coherence tomography", *Radiophys. Quantum Electron.* **41**, 850-873, (1998).
30. D Levitz, L Thrane, MH Frosz, PE Andersen, CB Andersen, J Valanciunaite, J Swartling, S Andersson-Engels, PR Hansen "Determination of optical scattering properties of highly-scattering media in optical coherence tomography images", *Opt. Expr.* **12**(2), 249-259 (2004).
31. IV Turchin, EA Sergeeva, LS Dolin, VA Kamensky, NM Shakhova, and R Richards-Kortum, "Novel algorithm of processing optical coherence tomography

images for differentiation of biological tissue pathologies". *J. Biomed. Opt.* **10**, 064024 (2005).

32. http://www.bme.ogi.edu/biomedicaloptics/BME606/classnotes/mcsub/index.html
33. LV Wang, SL Jacques, LQ Zheng, "MCML - Monte Carlo modeling of photon transport in multi-layered tissues". *Comp. Meth. Prog. Biomed.* **47**, 131-146 (1995).
34. F Truffer, *Determining optical properties with confocal microscopy in reflection and transmission mode*, Master's thesis, Hochschule Ravensburg-Weingarten (2008).
35. World Health Organization – World health report (2008), available at: http://www.who.int/whr/2008/en/index.html
36. Eds. A Atala and RP Lanza. *Methods of Tissue Engineering*. Academic Press: 2002.
37. CL Cummings, D Gawlitta, RM Nerem, and JP Stegemann, "Properties of engineered vascular constructs made from collagen, fibrin, and collagen-fibrin mixtures". *Biomaterials* **25**, 3699-3706 (2004).
38. BC Isenberg, C Williams, and RT Tranquillo, "Small-Diameter Artificial Arteries Engineered In Vitro". *Circ Res* **98**, 25-35 (2006).
39. JP Stegemann, H Hong, and RM Nerem, "Mechanical, biochemical, and extracellular matrix effects on vascular smooth muscle cell phenotype". *J Appl Physiol* **98**, 2321-2327 (2005).
40. S Ravi, Z Qu, EL Chaikof, "Polymer Materials for Tissue Engineering of Arterial Substitutes" *Vascular* **17** (supp 1), S45-S54 (2009).
41. D Lloyd-Jones, R Adams, M Carnethon, G DeSimone, TB Ferguson, K Flegal, E Ford, K Furie, A Go, K Greenlund, N Haase, S Hailpern, M Ho, V Howard, B Kissela, S Kittner, D Lackland, L Lisabeth, A Marelli, M McDermott, J Meigs, D Mozaffarian, G Nichol, C O'Donnell, V Roger, W Rosamond, R Sacco, P Sorlie, R Stafford, J Steinberger, T Thom, S Wasserthiel-Smoller, N Wong, J Wylie-Rosett, Y Hong, "Heart Disease and Stroke Statistics—2009 Update: A Report From the American Heart Association Statistics Committee and Stroke Statistics Subcommittee". *Circulation* **119**, e21-e181 (2009).

42. LE Niklason, J Gao, WM Abbott, KK Hirschi, S Houser, R Marini, and R Langer. "Functional arteries grown in vitro". *Science* **284**, 489-493 (1999).
43. MS Conte, "The ideal small artery substitute: a search for the Holy Grail?" *FASEB J* **12**: 43-45 (1998).
44. SL Mitchell and LE Niklason, "Requirements for growing tissue-engineered vascular grafts". *Cardiovasc Pathol* **12**, 59–64 (2003).
45. RT Tranquillo, "The tissue-engineered small-diameter artery". *Ann NY Acad Sci* **961**, 251–254 (2002).
46. CB Weinberg and E Bell, "A blood vessel model constructed form collagen and cultured vascular cells". *Science* **231**, 397–400 (1986).
47. GK Owens, "Regulation of differentiation of vascular smooth muscle". *Physiol Rev* **75**, 487–517 (1995).
48. N L'Heureux, JC Stoclet, FA Auger, GJ Lagaud, L Germain, and R. Andriantsitohaina. "A human tissue-engineered vascular media: a new model for pharmacological studies of contractile responses". *FASEB J* **15**, 515-524 (2001).
49. JP Stegemann and RM Nerem, "Phenotype modulation in Vascular Tissue Engineering Using Biochemical and Mechanical Stimulation". *Ann Biomed Eng* **31**, 391-402 (2003).
50. D Seliktar, RM Nerem, and ZS Galis, "Mechanical Strain-Stimulated Remodeling of Tissue Engineered Blood Vessel Constructs". *Tissue Eng* 9, 657-666 (2003).
51. JJ Ross and RT Tranquillo, "ECM gene expression correlates with *in vitro* tissue growth and development in fibrin gel remodeled by neonatal smooth muscle cells". *Matrix Biol* **22**, 477–490 (2003).
52. A Patel, B Fine, M Sandig, and K Mequanint, "Elastin biosynthesis: The missing link in tissue engineered blood vessels". *Cardiovasc Res* **71**, 40-49 (2006).
53. F Grinnell, "Fibroblast biology in three-dimensional collagen matrices". *Trends Cell Biol* **13**, 264-269 (2003).
54. JJ Tomasek, G Gabbiani, B Hinz, C Chaponnier, and RA Brown. Myofibroblasts and mechanoregulation of connective tissue remodeling. *Nature Rev Mol Cell Biol* **3**, 349-363 (2002).

55. CD Franco, B Ho, D Mulholland, G Hou, KL Donaldson, MP Bendeck, "Doxycycline alters vascular smooth muscle cell adhesion, migration and reorganization of fibrillar collagen matrices". *Am J Pathol* **168**, 1697-1709 (2006).
56. J Qi, L Chi, J Faber, B Koller, AJ Banes. ATP reduces gel compaction in osteolast-populated collagen gels. *J Appl Physiol* **102**, 1152-1160 (2007).
57. F Sabeh, XY Li, TL Saunders, RG Rowe, and SJ Weiss. "Secreted versus Membrane-anchored Collagenases. Relative Roles in Fibroblast-Dependent Collagenolysis and Invasion". *J Biol Chem* **284**, 23001-23011 (2009).
58. S Rhee and F Grinnell, "Fibroblast mechanics in 3D collagen matrices". *Adv Drug Del Rev* **59**, 1299-1305 (2007).
59. RA Brown, M Wiseman, CB Chuo, U Cheema, and SN Nazhat, "Ultrarapid engineering of biomimetic materials and tissues: fabrication of nano- and microstructures by plastic compression". *Adv Func Mater* **15**, 1762-1770 (2005).
60. M Sternlicht and Z Werb, "Matrix Metalloproteinases (MMPs)". In *Guidebook to the Extracellular Matrix and Adhesion Proteins*, 2nd Ed., T. Kreis and R. Vale, eds. 519-523 (1999).
61. V Lemaître and J D'Armineto, "Matrix metalloproteinases in development and disease". *Birth Defects Res C Embryo Today* **78**, 1-10 (2006).
62. K Hotary, E Allen, A Punturieri, I Yana, and SJ Weiss. "Regulation of Cell Invasion and Morphogenesis in a Three-Dimensional Type I Collagen Matrix by Membrane-Type Matrix Metalloproteinases 1, 2, and 3". *J Cell Biol* **149**, 1309-1323 (2000).
63. GJ Fisher, J Varani, and JJ Voorhees, "Looking older: fibroblast collapse and therapeutic implications". *Arch Dermatol* **144**, 666-72 (2008).
64. A Desmoulière, C Chaponnier, and G Gabbiani. "Tissue repair, contraction, and the myofibroblast". *Wound Rep Reg* **13**, 7-12 (2005).
65. ZS Galis, GK Sukhova, MW Lark, and P Libby. "Increased expression of matrix metalloproteinases and matrix degrading activity in vulnerable regions of human atherosclerotic plaques". *J Clin Invest* **94**, 2493-2503 (1994).

66. R Roy, J Yang, and MA Moses. "Matrix Metalloproteinases As Novel Biomarkers and Potential Therapeutic Targets in Human Cancer". *J Clin Oncol* **27**, 5287-97 (2009).
67. A Pardo and M Selman, "Matrix Metalloproteases in Aberrant Fibrotic Tissue Remodeling". *Proc Am Thorac Soc* **3**, 383-388 (2006).
68. D Seliktar, RM Nerem, and ZS Galis, "The Role of Matrix Metalloproteinase-2 in the Remodeling of Cell-Seeded Vascular Constructs Subjected to Cyclic Strain". *Ann Biomed Eng* **29**, 923-934 (2001).
69. MP Lutolf and JA Hubbell, "Synthetic biomaterials as instructive extracellular microenvironments for morphogenesis in tissue engineering". *Nat Biotechnol* **23**, 47-55 (2005).
70. Z Werb, "ECM and Cell Surface Proteolysis: Regulating Cellular Ecology". *Cell* **91**, 439-442 (1997).
71. A Page-McCaw, AJ Ewald, Z Werb, "Matrix metalloproteinases and the regulation of tissue remodeling". *Nat Rev Mol Cell Biol* **8**, 221-233 (2007).
72. W Borth, "α2-Macroglobulin, a multifunction binding protein with targeting characteristics". *FASEB J* **6**, 3345-3353 (1992).
73. LM Golub, HM Lee, G Lehrer, A Nemiroff, TF McNamara, R Kaplan, and NS Ramamurthy, "Minocycline reduces gingival collagenolytic activity during diabetes: Preliminary observations and a proposed new mechanism of action". *J Periodont Res* **18**, 516-26 (1983).
74. SA Myers, and RG Wolowacz, "Tetracycline-based MMP inhibitors can prevent fibroblast-mediated collagen gel contraction *in vitro*". *Adv Dent Res* **12**, 86-93 (1998).
75. L Thrane and TM Jørgensen, private communication (2004).
76. D Levitz, MT Hinds, N Choudhury, NT Tran, SR Hanson, and SL Jacques, "Quantitative characterization of developing collagen gels using optical coherence tomography", *J. Biomed. Opt.* in-press (2010).
77. A Tycho, TM Jørgensen, HT Yura, and PE Andersen, "Derivation of a Monte Carlo Method for Modeling Heterodyne Detection in Optical Coherence Tomography Systems", *Appl. Opt.* **41**, 6676-6691 (2002).

78. D Faber, F van der Meer, M Aalders, and TG van Leeuwen. “Quantitative measurements of attenuation coefficients of weakly scattering media using optical coherence tomography”, *Opt. Expr.* **12**, 4353-4365 (2004).
79. C Xu, JM Schmitt, SG Carlier, R Virmani, “Characterization of atherosclerosis plaques by measuring both backscattering and attenuation coefficients in optical coherence tomography”, *J. Biomed. Opt.* **13**(3), 034004 (2008).
80. RO Esenaliev, KV Larin, IV Larina, M Motamedi, “Noninvasive monitoring of glucose concentration with optical coherence tomography”, *Opt Lett* **26**, 992-994 (2001).
81. A Rollins, S Yazdanfar, M Mulkarni, R Ung-Arunyawee, J Izatt, ”*In vivo* rate optical coherence tomography”, *Opt. Expr.* **3**, 219-29 (1998).
82. RA Horn and CR Johnson, *Topics in matrix analysis,* Cambridge University Press (1991).
83. GH Golub, CF van Loan, *Matrix Computations*, 3rd ed., Johns Hopkins University Press (1996).
84. C Mätzler, “Matlab Functions for Mie Scattering and Absorption”, Research Report 2002-08, Insitut für Angewandte Physik, (2002).
85. BW Pogue and MS Patterson, “Review of tissue simulating phantoms for optical spectroscopy, imaging and dosimetry”, *J Biomed Opt* **11**, 041102 (2006).
86. W Tan, A Sendemir-Urkmez, LJ Fahrner, R Jamison, D Leckband, SA Boppart, “Structural and Functional Optical Imaging of Three-Dimensional Engineered Tissue Development”, *Tissue Eng* **10**, 1747-57 (2004).
87. W Tan, AL Oldenburg, JJ Norman, TA Desai, SA Boppart, “Optical coherence tomography of cell dynamics in three-dimensional tissue models”, *Opt Expr* **14**, 7159–7171 (2006).
88. SM Rey, B Povazay, B Hofer, A Unterhuber, B Hermann, A Harwood, W Drexler, “Three- and four-dimensional visualization of cell migration using optical coherence tomography” *J Biophotonics* **2**, 370-379 (2009).
89. Y Yang, A Dubois, X Qin, J Li, A El Haj, RK Wang, “Investigation of optical coherence tomography as an imaging modality in tissue engineering”, *Phys Med Biol* **51**, 1649–1659 (2006).

90. PO Bagnaninchi, Y Yang, N Zghoul, N Maffulli, RK Wang, AJ El Haj, "Chitosan Microchannel Scaffolds for Tendon Tissue Engineering characterized by optical coherence tomography", *Tissue Eng* **13**, 323-331 (2007).
91. WD McMillan, BK Patterson, RR Keen, WH Pearce, "*In situ* localization and quantification of seventy-two – kilodalton type IV collagenase in aneurismal, occlusive, and normal aorta", *J Vasc Surg* **22**, 295-305 (1995).
92. N Choudhury, G Song, F Chen, S Matthews, T Tschinkel, J Zhen, SL Jacques, AL Nuttall, "Low coherence interferometry of the cochlear partition", *Hear Res* **220**, 1–9 (2006).
93. FJ van der Meer, DJ Faber, DMB Sassoon, MC Aalders, G Pasterkamp, TG van Leeuwen, "Localized Measurement of Optical Attenuation Coefficients of Atherosclerotic Plaque Constituents by Quantitative Optical Coherence Tomography", *IEEE Trans. Med. Imaging* **24**, 1369-76 (2005).
94. X Xu, RK Wang, A El Haj, "Investigation of changes in optical attenuation of bone and neuronal cells in organ culture or 3 dimensional constructs *in vitro* with optical coherence tomography: relevance to cytochrome-oxidase monitoring" *Eur Biophys J* **32**, 355-362 (2003).
95. DS Gareau, Y Li, B Huang, Z Eastman, KS Nehal, M Rajadhyaksha, "Confocal mosaicing microscopy in Mohs skin excisions: feasibility of rapid surgical pathology", *J Biomed Opt* **13**, 054001 (2008).
96. LC Abraham, E Zuena, B Perez-Ramirez, DL Kaplan, "Guide to collagen characterization for biomaterial studies", *J Biomed Mater Res B* **87**, 264-85 (2008).
97. M Gioia, S Monaco, GF Fasciglione, A Coletti, A Modesti, S Marini, M Coletta, "Characterization of the Mechanisms by which Gelatinase A, Neutrophil Collagenase, and Membrane-Type Metalloproteinase MMP-14 Recognize Collagen I and Enzymatically Process the Two α–chains", *J Mol Biol* **368**, 1101-1113 (2007).
98. YG Patel, KS Nehal, I Aranda, Y Li, AC Halpern, M Rajadhyaksha, "Confocal reflectance mosaicing of basal cell carcinomas in Mohs surgical skin excisions", *J Biomed Opt* **12**, 034027 (2007).

99. DS Gareau, “Feasibility of digitally stained multimodal confocal mosaic to simulate tissue histopathology”, *J Biomed Opt* **14**, 034050 (2009).

100. D Levitz, N Choudhury, K Vartanian, MT Hinds, SR Hanson, SL Jacques. “Optically characterizing collagen gels made with different cell types” in Optics in Tissue Engineering and Regenerative Medicine III. Eds. Kirkpatrick SJ, Wang RK. *Proc SPIE* 2009; **7179**: 717905.

101. G Serini and G Gabbiani, “Mechanisms of Myofibroblast Activity and Phenotypic Modulation”, *Exp Cell Res* **250**, 273-283 (1999).

102. GE Davis and DR Senger, “Endothelial extracellular matrix: biosynthesis, remodeling, and functions during vascular morphogenesis and neovessel stabilization”, *Circ Res* **97**, 1093-1107 (2005).

103. LM Coussens and Z Werb, “Matrix metalloproteinases and the development of cancer”, *Chem Biol* **3**, 895-904 (1996).

104. D Seliktar, RA Black, RP Vito, RM Nerem, “Dynamic Mechanical Conditioning of Collagen-Gel Blood Vessel Constructs Induces Remodeling *in Vitro*” *Ann Biomed Eng* **28**, 351-362 (2000).

105. C Egles, Y Shamis, JR Mauney, V Volloch, DL Kaplan, JA Garlick, “Denatured collagen modulates the phenotype of normal and wounded human skin equivalents”, *J Invest Dermatol* **128**, 1830-37 (2008).

106. D Levitz, MT Hinds, A Ardeshiri, SR Hanson, SL Jacques “Non-destructive label-free monitoring of local smooth muscle cell remodeling of collagen gels using optical coherence tomography” To be submitted to Biomaterials (2010).

107. L Thrane, MH Frosz, TM Jørgensen, A Tycho, HT Yura, PE Andersen, “Extraction of optical scattering parameters and attenuation compensation in optical coherence tomography images of multilayered tissue structures”, *Opt Lett* **29**, 1641-1643 (2004).

108. S Gerontas, SS Farid, M Hoare, “Windows of Operation for Bioreactor Design for the Controlled Formation of Tissue-Engineered Arteries”, *Biotechnol Prog* **25**, 842-853 (2009).

109. MS Sacks, FJ Schoen, JE Mayer Jr., “Bioengineering Challenges for Heart Valve Tissue Engineering”, *Ann Rev Biomed Eng* **11**, 289-313 (2009).

110. FJ van der Meer, DJ Faber, I Cilesiz, MJ van Gemert, TG van Leeuwen, “Temperature-dependent optical properties of individual vascular wall components measured by optical coherence tomography”, *J Biomed Opt* **11**, 041120 (2006).

Biographical sketch

David Levitz obtained his BS degree from the Biomedical Engineering Department at the University of Rochester in 2002 and his MS degree from the Department of Physics in Lund University, Sweden in 2004. He joined the Biomedical Engineering Department at Oregon Health and Science University later in 2004, and worked with Prof. Steven L. Jacques imaging matrix remodeling in collagen gels.